

The VLA-Cosmos 3 GHz Large Project

Tisanić, Krešimir

Doctoral thesis / Disertacija

2020

Degree Grantor / Ustanova koja je dodijelila akademski / stručni stupanj: **University of Zagreb, Faculty of Science / Sveučilište u Zagrebu, Prirodoslovno-matematički fakultet**

Permanent link / Trajna poveznica: <https://um.nsk.hr/um:nbn:hr:217:625398>

Rights / Prava: [In copyright](#) / [Zaštićeno autorskim pravom.](#)

Download date / Datum preuzimanja: **2024-04-27**



Repository / Repozitorij:

[Repository of the Faculty of Science - University of Zagreb](#)





University of Zagreb
Faculty of Science
Department of Physics

Krešimir Tisanić

**The VLA-COSMOS 3 GHz Large Project:
Spectral energy distributions in the
radio band**

DOCTORAL THESIS

Zagreb, 2020



University of Zagreb
Faculty of Science
Department of Physics

Krešimir Tisanić

**The VLA-COSMOS 3 GHz Large Project:
Spectral energy distributions in the
radio band**

DOCTORAL THESIS

Supervisor:
prof. dr. sc. Vernesa Smolčić

Zagreb, 2020



Sveučilište u Zagrebu
Prirodoslovno-matematički fakultet
Fizički odsjek

Krešimir Tisanić

**VLA-COSMOS veliki projekt na 3 GHz:
Spektralne energetske distribucije u
radio području**

DOKTORSKI RAD

Mentor:
prof. dr. sc. Vernesa Smolčić

Zagreb, 2020

Supervisor information

This thesis was made under the supervision of prof. dr. sc. Vernesa Smolčić, as a part of the PHD program at the Department of Physics, Faculty of Science, University of Zagreb.

Vernesa Smolčić's main area of research is observational astrophysics. She attained her Masters degree in physics from the Department of Physics, Faculty of Science, University of Zagreb (Zagreb, Croatia) in 2004, and a doctoral degree from the Ruperto-Carola University (Heidelberg, Germany) in 2007. After obtaining her doctoral degree, she held two postdoctoral positions. She was a CARMA Postdoctoral Scholar at the California Institute of Technology (2008-2010), and the ESO ALMA COFUND Fellow at the Argelander Institute for Astronomy, Bonn (2010-2013).

She became an assistant professor at the Department of Physics, Faculty of Science, University of Zagreb in 2010, and was promoted to an associate professor in 2015. She co-authored 136 refereed publications in Current Content journals, with more than 15000 citations and a H-index of 49.

She was the leader of the project *Constraining Stellar Mass and Supermassive Black Hole Growth through Cosmic Times: Paving the way for the next generation sky surveys* (project ID: 337595), which was funded by the European Research Council (ERC) Starting Grant.

Acknowledgements

I would like to thank my supervisor, Vernesa Smočić, for guidance during the course of my PHD.

I would also like thank the members of the VLA-COSMOS team and co-authors Gianni Zamorani, Jacinta Delhaize, Mladen Novak, Ivan Delvecchio, Lana Ceraj, Eva Schinnerer, Huib Intema, Marco Bondi, and Eleni Vardoulaki for providing helpful comments and suggestions when publishing papers.

My gratitude goes to Marko, my mum, dad, and grandma. Thank your for being beside me.

Abstract

A galaxy's spectral energy distribution (SED) enables the estimation of different galactic properties. In contrast to the better-understood, but harder to interpret, infrared SED, the radio spectrum below 30 GHz offers a dust-unbiased way of constraining properties of galaxies.

We have constructed the average radio spectral energy distribution for 1.4 GHz-selected samples of highly star-forming galaxies ($\text{SFR} > 100 \text{ M}_{\odot}/\text{yr}$, HSFGs), and a sample of sources exhibiting a 3σ excess of radio luminosity from that expected from star formation (RxAGN) in the COSMOS field. To achieve a broad rest-frame frequency range, we combined previously published VLA observations at 1.4 GHz and 3 GHz with unpublished GMRT observations at 325 MHz and 610 MHz by employing survival analysis to account for non-detections in the GMRT maps caused by their higher RMS values.

For HSFGs, by fitting a broken power-law to the SED, we find the spectral index to change from $\alpha_1 = 0.42 \pm 0.06$ below 4.3 GHz to $\alpha_2 = 0.94 \pm 0.06$ above 4.3 GHz. Our results are in line with previous low-redshift studies of star-forming galaxies with an $\text{SFR} > 10 \text{ M}_{\odot}/\text{yr}$ that show that their SED differs from the one found in normal star-forming galaxies by having a steeper spectral index around 10 GHz, which could imply a smaller thermal fraction than in normal star-forming galaxies. For RxAGN, we find that a single power-law model fits best with a spectral index of 0.64 ± 0.07 . However, such a model does not capture all the features of the RxAGN radio SED which can be better described by a broken power-law with a spectral index of 0.28 ± 0.03 , below 4 GHz, and 1.16 ± 0.04 , above 4 GHz.

We have established the different SED shapes for highly star-forming galaxies and RxAGN at radio frequencies around 1-10 GHz in the COSMOS field. Further work needs to be done to assess the possible differences in SEDs above 10 GHz, which would give better estimates of the free-free contribution in star-formation processes at high redshift, providing a major step forward in understanding the average radio SEDs affecting the prevalence of different galaxy populations in samples detected in present and future deep radio surveys.

Keywords: galaxies, galaxy evolution, radio emission, spectral energy distribution, star formation, active galactic nuclei, COSMOS field, Very Large Array

Prošireni sažetak

Svojstva galaksija mogu se odrediti koristeći njihove spektralne energetske distribucije (SED). Za razliku od bolje istraženih SED-ova u infracrvenom području, radio spektar na frekvencijama manjim od 30 GHz je lakši za interpretirati jer nije pod utjecajem prašine te stoga pruža nepristran način određivanja svojstava galaksija.

Konstruirali smo prosječne spektralne energetske distribucije za uzorke galaksija selektirane po opažanjima na 1.4 GHz dvaju populacija galaksija. Uzorak galaksija koje intenzivno stvaraju zvijezde (skraćeno HSFG), izabran je prema kriteriju brzine stvaranja zvijezda $\text{SFR} > 100 \text{ M}_\odot/\text{yr}$, dok je uzorak aktivnih galaktičkih jezgri sa suviškom radio zračenja (Rx-AGN) identificiran 3σ suviškom radio luminoziteta u odnosu na očekivani radio luminozitet s obzirom na procese povezane sa stvaranjem zvijezda. Kako bismo postigli širok raspon frekvencija u sustavu mirovanja izvora spojili smo već prethodno objavljena opažanja VLA interferometrom na 1.4 GHz i 3 GHz s prethodno neobjavljenim GMRT opažanjima na 325 MHz i 610 MHz. VLA opažanja imaju veću dubinu, mjerenu srednjim kvadratnim odstupanjem radio mapa, od GMRT opažanja. Taj nesrazmjer smo razriješili koristeći analizu preživljavanja.

Za HSFG galaksije, koristeći prilagodbu slomljenog zakona potencije na radio SED, pronalazimo da im se spektralni indeks mijenja od $\alpha_1 = 0.42 \pm 0.06$, ispod 4.3 GHz, do $\alpha_2 = 0.94 \pm 0.06$, iznad 4.3 GHz. Ovi rezultati se slažu s prethodnim studijama $\text{SFR} > 10 \text{ M}_\odot/\text{yr}$ galaksija izvedenima pri malom crvenom pomaku. Te studije ukazivale su da HSFG galaksije pokazuju strmije spektre (veći spektralni indeks) oko 10 GHz u odnosu na normalne galaksije u kojima se stvaraju zvijezde, što upućuje na manji doprinos termalnog zračenja. Za RxAGN uzorak pronalazimo kako uzorak možemo opisati običnim zakonom potencije sa spektralnim indeksom od 0.64 ± 0.07 , no također smo uvidjeli kako tim jednostavnim modelom ne možemo obuhvatiti sve karakteristike RxAGN spektra. Ponovno koristeći slomljeni zakon potencije, dobivamo spektralni indeks od 0.28 ± 0.03 ispod 4 GHz te spektralni indeks od 1.16 ± 0.04 iznad 4 GHz.

Ukratko, odredili smo oblik spektralnih energetske distribucije dvaju uzoraka galaksija (HSFG i RxAGN) u rasponu od 1 GHz do 10 GHz u COSMOS predjelu neba. Potrebna su daljnja istraživanja kako bi se odredile razlike u obliku SED-a iznad 10 GHz u svrhu dobivanja bolje ocjene doprinosa zakročnog zračenja pri procesu stvaranja zvijezda u galaksijama

na velikom crvenom pomaku te kako bi se bolje razumjeli odnosi između različitih populacija galaksija u uzorcima u sadašnjim i budućim pregledima neba.

Ključne riječi: galaksije, evolucija galaksija, radio zračenje, spektralna energetska distribucija, stvaranje zvijezda, aktivna galaktička jezgra, COSMOS polje, Very Large Array

Uvod

Evolucija svemira je jedno od najvećih područja istraživanja u modernoj astrofizici. U današnje vrijeme takva istraživanja iziskuju poznavanje našeg bliskog dijela svemira koje koristimo za dobivanje spoznaja o daljem dijelu svemira.

Kozmologija

Prva teorijska razmatranja o obliku svemira započeta su početkom 20. stoljeća na temelju opće teorije relativnosti ([de Sitter 1916](#); [Einstein 1919](#); [Friedman 1922](#)), a prva opažачka informacija o evoluciji svemira je spoznaja da galaksije koje su dalje od nas imaju i veće radijalne brzine. Ova poveznica postala je poznata kao Hubbleov zakon ([Hubble 1929](#)), a konstanta proporcionalnosti prozvana je Hubbleovom konstantom (sadašnje vrijednosti oznake H_0).

[Penzias & Wilson \(1965\)](#) otkrili su suvišak zračenja na temperaturi od 3.5 ± 1.0 K koje je bilo začuđujuće izotropno, nepolarizirano i neovisno o godišnjim dobima. Ovo kozmičko mikrovalno pozadinsko zračenje (CMB) je ujedno najsavršenije izmjereno zračenje crnog tijela ([Fixsen et al. 1996](#); [Fixsen 2009](#)).

Galaksije

Iako ne postoji formalna definicija galaksije, [Forbes & Kroupa \(2011\)](#) predložili su definiciju galaksije kao gravitacijski vezanog sustava koji sadrži zvijezde uz uvjet relaksacijskog vremena većeg od H_0^{-1} i polumjera većeg od 100 pc. Nekoliko galaksija, poput Andromedine galaksije i našeg Mliječnog puta mogu se opaziti i golim okom te su poznate odavno, iako su prvotno bile smatrane maglicama (kao u Messierovom i NGC katalogu, [Messier 1781](#); [Dreyer 1888](#)). [Hubble \(1925\)](#) je utvrdio kako su ‘spiralne maglice’ zapravo izvangalaktički objekti.

Pronađeno je da se galaksije tipično nalaze na ‘glavnom nizu’ u ravnini zvjezdane mase i brzine stvaranja zvijezda (Noeske et al. 2007; Elbaz et al. 2007, 2011). One mogu proći kroz fazu praskovitog stvaranja zvijezda (engl. *starburst phase*), što može biti posljedica sudara galaksija (Sanders & Mirabel 1996). Lilly et al. (2013) su razvili jednostavan model u kojemu tipična galaksija polazi iz glavnog niza povećavajući svoju masu pobirući hladan plin iz svoje okoline. Kako se približava kritičnoj masi, dotok svježeg plina je zaustavljen te se zaustavlja stvaranje zvijezda, što je dosad još slabo shvaćen proces (Heckman & Best 2014).

Aktivne galaktičke jezgre

Prisutstvo aktivne galaktičke jezgre (AGN) je nužno za objašnjavanje svojstava galaksija (Heckman & Best 2014). Već dugo (Kormendy & Richstone 1995) postoje naznake da su u središtu AGN-ova zapravo supermasivne crne rupe (SMBH), no prva izravna potvrda dolazi iz opažanja sjene supermasivne crne rupe u središtu divovske eliptične galaksije M87 (Akiyama et al. 2019).

Postoji dihotomija fizičkih procesa prilikom akrecije mase na SMBH unutar AGN-ova. U radijativnom modu, SMBH okružuje geometrijski tanak ali optički debeo akrecijski disk (Shakura & Sunyaev 1973), dok u mlaznom modu umjesto njega postoji geometrijski debeo akrecijski tok dominiran advekcijom u kojemu se većina energije prenosi entropijom umjesto da je odnešena zračenjem (Narayan & Yi 1994). Izvori koji imaju karakteristike ova dva moda su također prozvani radijativno efikasni i neefikasni AGN-ovi.

U radio području spektra, AGN-ovi emitiraju netermalno sinkrotronsko zračenje te se mogu klasificirati na temelju toga dolazi li većina radio zračenja iz predjela bliskom centralnom izvoru (FR I) ili iz režnjeva (FR II, Fanaroff 1974).

Postoji iznenađujuće podudaranje između evolucije brzine stvaranja zvijezda (Madau et al. 1996) i akrecije materije na SMBH (Shankar et al. 2009) tijekom povijesti svemira. Mogući razlog jest prisutnost centralnog praska stvaranja zvijezda blizu središta AGN-a (Boyle & Terlevich 1998; Silverman et al. 2008). Dva su moguća načina na koji središnji SMBH može utjecati na proces stvaranja zvijezda u galaksiji. U kvazarskom modu povratne sprege (Kauffmann & Haehnelt 2000), rezervoar hladnog plina je izbačen dalje od AGN galaksije pomoću zračenja i mlazova, dok u radio modu povratne sprege mlazovi injektiraju kinetičku energiju u svoju

okolinu, zagrijevaju plin i prašinu te time zaustavljaju stvaranje zvijezda (Croton et al. 2006, 2016).

Spektri galaksija u radio području

Radio SED izvora u rasponu od 1 – 10 GHz je često pojednostavljen u oblik zakona potencije, opisan spektralnim indeksom od $\alpha = 0.7$ (koristeći konvenciju $S \sim \nu^{-\alpha}$, Condon 1992). Očekivani glavni doprinos koji daje ovakav oblik spektra je sinkrotronsko zračenje koje dolazi ili od ostataka supernovi, koji su povezani s procesima stvaranja zvijezda, ili od aktivnosti AGN-a. Preciznija opažanja pokazala su da postoje devijacije od ovog jednostavnog modela u formi drugačije vrijednosti spektralnog indeksa ili pak kompleksnijeg oblika spektra (vidi npr. Kukula et al. 1998; Kimball & Ivezić 2008; Clemens et al. 2008; Leroy et al. 2011; Calistro Rivera et al. 2017; Galvin et al. 2018; Tisanić et al. 2019).

Tipični oblik SED-a normalne galaksije u kojoj se stvaraju zvijezde ($SFR < 10 M_{\odot}/\text{yr}$) je opisiv kao zakon potencije spektralnog indeksa od ~ 0.8 te kao dodatne termalne komponente udjela 8 – 10% koja dolazi od zakočnog zračenja (Klein et al. 1988; Condon & Yin 1990). Kod objekata koji imaju puno veću brzinu stvaranja zvijezda, pronađeno je puno manje emisije zakočnog zračenja te smanjivanje spektralnog indeksa zakona potencije na frekvencijama oko 1 GHz.

Kvazari pokazuju spektre koji mogu biti ili strmi (spektralnog indeksa većeg od 0.5) ili ravni (<0.5) (Kukula et al. 1998). U uzorcima snažih radio izvora ($\sim 1 \text{ Jy}$), uz izvore ravnog spektra postoji i značajni udio (40 – 50%) izvora strmog spektra te izvora koji imaju vrh u emisiji ili čak invertirani spektar (Kapahi 1981; Peacock & Wall 1982; De Zotti et al. 2010). Emisija koja dolazi iz radio režnjeva je često strmog spektra, dok je ravniji spektar posljedica emisije kompaktnijih izvora usljed sinkrotronske samoapsorpcije (Kimball & Ivezić 2008).

Mnoge studije pokazale su da postoji poveznica između infracrvenih i radio luminoziteta (van der Kruit 1971; Helou et al. 1985; Condon 1992). Ova korelacija, prozvana infracrveno-radio korelacija i definirana parametrom q , je okosnica ideje korištenja radio luminoziteta kao pokazatelja stvaranja zvijezda jer spaja radio luminozitet s bolje shvaćenim infracrvenim luminozitetom, koji je povezan sa brzinom stvaranja zvijezda (Kennicutt 1998b).

U jednostavnom modelu (Voelk 1989), q vrijednost je konstanta za različite vrijednosti jačine galaktičkog magnetskog polja u kojemu elektroni gube energiju sinkrotronski i inverzno komptonski. Na velikim crvenim pomacima, analitički modeli (Murphy 2009), predviđaju da q vrijednost raste s crvenim pomakom zbog utjecaja pozadinskih CMB fotona, no nedavne studije temeljene na analizi preživljavanja pronalaze obrnut trend (Ivison et al. 2010; Magnelli et al. 2015; Delhaize et al. 2017; Calistro Rivera et al. 2017).

VLA-COSMOS projekt

COSMOS je pankromatski pregled neba veličine 2 kvadratna stupnja u zviježđu sekstant. Ovaj pregled neba je, među ostalim, dizajniran za proučavanje stvaranja galaksija, jata galaksija i tamne materije, te proučavanje evolucije svojstava galaksija u širokom rasponu crvenog pomaka $z \in \langle 0.5, 6 \rangle$ (Scoville et al. 2007). U radio području, postoje VLA opažanja cijelog COSMOS polja (Schinnerer et al. 2007, 2010; Smolčić et al. 2014, 2017b; Tisanić et al. 2019) u rasponu od 1 – 3 GHz (Schinnerer et al. 2007, 2010; Smolčić et al. 2017b) te ispod 1 GHz koristeći GMRT (Tisanić et al. 2019).

Konstrukcija GMRT kataloga

GMRT opažanja COSMOS polja provedena su koristeći 30 antena razmaka do 25 km te su reducirana koristeći SPAM proceduru opisanu u Intema et al. (2017).

Opažanja na 325 MHz izvedena su u jednom smjeru (engl. *pointing*) opažanja u sklopu projekta 07SCB01 (PI: S. Croft) u alociranom vremenu od 45 h podijeljenom u 4 opažanja. Konačno producirana mapa ima rezoluciju od $10.8 \times 9.5 \text{ arcsec}^2$ i medijalni srednji kvadratni šum od $97 \mu\text{Jy}/\text{beam}$.

Opažanja na 610 MHz izvedena su u 19 smjerova u sklopu projekta 11HRK01 (PI: H. R. Klöckner). Svi smjerovi su u konačnici pretvoreni u mape na rezoluciji od $5.6 \times 3.9 \text{ arcsec}^2$, primijenjena je korekcija primarne zrake te su svi smjerovi složeni u mozaik prateći proceduru iz Smolčić et al. (2018). Mozaik ima medijalni srednji kvadratni šum od $39 \mu\text{Jy}/\text{beam}$.

Radio izvori su detektirani unutar mapa koristeći BLOBCAT (Hales et al. 2012) kod koristeći prag od 5σ , gdje je σ određen koristeći RMS mapu produciranu programom AIPS. Konačne

kataloge suzili smo na COSMOS polje. Pronalazimo 633 komponenti izvora u 325 MHz mapi i 999 komponenti izvora u 610 MHz mapi. Nakon uzimanja u obzir multikomponentnih izvora i miješanja izvora, konačan broj izvora je 633 unutar COSMOS polja za 325 MHz mapu, odnosno 986 za 610 MHz mapu. Primijenjena je korekcija na razmazivanje širine frekvencijskog pojasa (engl. *bandwidth smearing correction*). Sveukupno pronalazimo 177 (196) razlučenih izvora u 325 MHz (610 MHz) mapi.

Pogreške gustoća toka pojedinih izvora u 610 MHz katalogu uvećali smo za 20% prije publiciranja zbog netrivialnog deficita toka zračenja u odnosu na očekivanja temeljena na VLA opažanjima.

Konstrukcija srednjeg SED-a

Kako bismo konstruirali tipični SED uzorka galaksija u COSMOS polju, normalizirali smo spektar individualnih galaksija na njihovim pripadnim frekvencijama u sustavu mirovanja koristeći dostupne GMRT i VLA mape. Budući da crveni pomaci objekata u našim uzorcima variraju od 0.3 do 4, dobivamo dobro definiran SED u rasponu frekvencija u sustavu mirovanja od ~ 0.5 GHz do ~ 15 GHz.

Budući da imamo vrlo mali broj detekcija u mapama na 325 i 610 MHz, normalizirali smo gustoće tokova na svim frekvencijama koristeći linearnu prilagodbu na spektre dobivene samo iz 1.4 i 3 GHz frekvencija. Za izvore koji nisu detektirani na 325 i 610 MHz, procjenjujemo gustoću toka kao peterostruku vrijednost lokalnog srednjeg kvadratnog šuma unutar odgovarajuće GMRT mape te time dobivamo samo procjene gustoće toka - gornje limite.

Sveukupno područje frekvencija u sustavu mirovanja dijelimo na 20 dijelova u kojima zasebno proračunavamo srednji normalizirani logaritam gustoće toka, koristeći analizu preživljavanja ako u određenom predjelu spektra postoje gornji limiti. Analiza preživljavanja temeljena je na prilagodbi funkcije preživljavanja dobivene Kaplan-Meier metodom pomoću Weibullove distribucije, čije je statističke momente jednostavno procijeniti. Korištene su Monte Carlo simulacije kako bismo potvrdili koliko je ova metoda precizna prilikom određivanja parametara spektralnih energetske distribucija.

Srednji radio SED HSFG uzorka

Izabrali smo uzorak HSFG galaksija baziran na 1.4 GHz opažanjima uz uvjet $\text{SFR} > 100 \text{ M}_\odot/\text{yr}$ u COSMOS polju. Ovom skupu podataka pridružili smo 3 GHz podatke te puno pliće GMRT podatke. U uzorku nalazimo 306 galaksija, od kojih je 9% (29) detektirano na 325 MHz i 17% (52) na 610 MHz.

Na ovaj uzorak primjenjujemo metodu iz prethodnog poglavlja i koristimo prilagodbe na slomljeni zakon potencije. Pronalazimo da se spektralni indeks mijenja od $\alpha_1 = 0.53 \pm 0.04$ ispod 4.3 GHz do $\alpha_2 = 0.94 \pm 0.06$ iznad 4.3 GHz. Koristeći simulacije, pronalazimo da je korigirani spektralni indeks $\alpha_1^{\text{corr}} = 0.42 \pm 0.06$. Naši rezultati su u skladu s prethodnim opažanja galaksija s $\text{SFR} > 10 \text{ M}_\odot/\text{yr}$ na niskim crvenim pomacima koja pronalaze da je SED ove populacije drukčiji od onog očekivanog od normalne populacije galaksija u kojima se stvaraju zvijezde jer je strmiji oko 10 GHz, što može implicirati manji termalni omjer.

Također smo konstruirali infracrvenu-radio korelaciju koristeći naš dobiveni model slomljenog zakona potencije za galaksije s $\text{SFR} > 10 \text{ M}_\odot/\text{yr}$ te SED baziran na strmom ne-termalnom sinkrotronskom spektru i 10% termalnom omjeru na 1.4 GHz (Tabatabaei et al. 2017) za galaksije s $\text{SFR} < 10 \text{ M}_\odot/\text{yr}$. Pronalazimo da oblik radio spektra nije vjerojatan uzrok opadanja infracrveno-radio korelacije sa crvenim pomakom.

Srednji radio SED RxAGN uzorka

Odredili smo srednji radio SED koristeći AGN uzorak u COSMOS polju na temelju dostupnih VLA i GMRT opažanja. Odabrali smo uzorak AGN izvora temeljen na izvorima koji imaju 3σ suvišak 1.4 GHz radio luminoziteta naspram onoga očekivanog od procesa stvaranja zvijezda unutar galaksije domaćina AGN-a. Naš RxAGN uzorak je relativno kompletan (75%) u crvenom pomaku do $z \sim 4$ te u radio luminozitetu od 10^{24} W/Hz do 10^{26} W/Hz .

Pronalazimo da naš SED možemo opisati spektralnim indeksom od 0.64 ± 0.07 , no da bolji opis daje model slomljenog zakona potencije sa spektralnim indeksom od $\alpha_1 = 0.28 \pm 0.03$ ispod 4 GHz i spektralnim indeksom od $\alpha_2 = 1.16 \pm 0.04$ iznad 4 GHz.

Ovisnost infracrveno-radio korelacije o crvenom pomaku

Konstruirali smo jednostavan model za analitičko određivanje infracrveno-radio korelacije koristeći funkcije luminoziteta. Povezujemo infracrvene funkcije luminoziteta zajedno sa radio funkcijama luminoziteta za populaciju galaksija u kojima se stvaraju zvijezde koristeći Gaussovu kopulu, izabranu tako da možemo reproducirati lokalnu q vrijednost od 2.34 te njezinu disperziju (0.33).

Ovako konstruiranu zajedničku funkciju luminoziteta smo iskoristili kako bismo odredili q vrijednosti na većim crvenim pomacima. Koristeći granice infracrvenih i radio opažanja, propagiranih u sustav mirovanja te implementiranih analizom preživljavanja, pronalazimo kako se q vrijednosti počinju smanjivati iznad $z \sim 1$, što nije slučaj ako ne primijenimo granice opažanja. U našem modelu, ova razlika je nastala zbog toga što analiza preživljavanja nije uspjela dobro reproducirati q vrijednosti ispod $q < 2$, što je utjecalo na dobivene srednje q vrijednosti.

Potrebni su dodatni koraci kako bi se model testirao koristeći različite podatke na širokom rasponu crvenih pomaka kako bi se mogao usporediti s opažanjima na velikim crvenim pomacima koja također pokazuju padajući $q - z$ trend.

Glossary

Λ CDM Λ cold dark matter model. 3

AGN active galactic nucleus. 8–12, 19, 21, 75–77, 79, 97, 109, 110

ANOVA Analysis of variance. 92, 94, 95, 98

BPL broken power-law. xxii–xxiv, xxvi, 81, 84, 85, 88, 90–97

CDM cold dark matter model. 6

CMB Cosmic microwave background radiation. xv, 2, 4

COBE Cosmic Background Explorer satellite. 2

COSMOS Cosmological Evolution Survey. 21, 77–79, 97, 109

COSMOS2015 COSMOS2015 ([Laigle et al. 2016](#)). 78

CR Cosmic ray. 13, 14, 18

FIM Fisher information metric. xxiii, 83, 87

FLRW Friedmann-Lemaitre-Robertson-Walker metric. 2

GMRT Giant Meterwave Radio Telescope. 23, 77, 79, 97

HLAGN moderate-to-high radiative luminosity AGN. 79

i-band i-band ([Capak et al. 2007](#)). 78

IMF initial mass function. 6

IRAC IRAC ([Sanders et al. 2007](#)). 78

LOFAR The Low-Frequency Array. 19, 75, 76

MBAM Manifold Boundary approximation method. xxiii, 82, 83, 85, 86

MCMC Markov Chain Monte Carlo. 81, 82

MLAGN low-to-moderate radiative luminosity AGN. 79

MWACS The Murchison Widefield Array Commissioning Survey. 75

PL power-law. xxii, xxiii, xxvi, 84, 85, 88, 90–96

RMS root-mean-square. 77, 80

RT Razin-Tsytovič effect. 15

RxAGN radio-excess active galactic nuclei. xxii–xxiv, xxvi, 78–80, 84–95, 97, 98, 109, 110

RxHLAGN moderate-to-high luminosity RxAGN. xxvi, 79, 80, 90–96

RxQMLAGN low-to-moderate luminosity quiescent RxAGN. xxvi, 79, 80, 90–96

RxSMLAGN low-to-moderate luminosity star-forming RxAGN. xxvi, 79, 80, 90–95

SA synchrotron aging. 81, 85, 98, 110

SED spectral energy distribution. xxii–xxiv, 12, 18, 19, 22, 23, 75–77, 79–82, 84–90, 95–98, 109, 110

SFR star formation rate. 6

SKA Square Kilometer Array. 75

SMBH supermassive black hole. 8, 9, 11

SSA synchrotron self-absorption. 81, 85, 88, 96–98, 110

VLA Karl G. Jansky Very Large Array. 21, 77, 88, 97

VLA1.4JP VLA-COSMOS 1.4 GHz Joint Project. 77

VLA3LP VLA-COSMOS 3 GHz Large Project. xxii, 77, 79, 80

WMAP Wilkinson Microwave Anisotropy Probe. 3

List of Figures

1.1	The Cosmic microwave background (CMB) radiation temperature map adapted from Aghanim et al. (2019)	4
1.2	Comparison of the best-fit star-formation history (thick solid curve) with the massive black hole accretion history from X-ray [red curve Shankar et al. (2009)]. The shading indicates the $\pm 1\sigma$ uncertainty range on the total bolometric luminosity density. The comoving rates of black hole accretion have been scaled up by a factor of 3,300 to facilitate visual comparison to the star-formation history. Figure adapted from Madau & Dickinson (2014)	8
1.3	The categorization of the local AGN population. The blue text describes typical properties of each AGN class. Figure adapted from Heckman & Best (2014)	9
1.4	Model radio–FIR spectrum for a galaxy. Figure adapted from Murphy (2009)	12
1.5	Visualization of the covering area of the COSMOS field, adapted from www.spacetelescope.org/images/heic0701f . Credit: NASA, ESA and Z. Levay (STScI).	20
2.1	The left panel shows the visibility function for the entire 325 MHz map (blue line) and the 2 deg^2 COSMOS field (orange line). The median RMS within the COSMOS field is denoted by the black dashed line. The positions of sources detected using blobcat in the 325 MHz map are shown in the left panel. The blue rectangle denotes the 2 deg^2 COSMOS field, while the dashed circle shows the pointing half-power radius.	25

- 2.2 The left panel shows the visibility function for the entire 610 MHz map (blue line) and the 2 deg^2 COSMOS field (orange line). The median RMS within the COSMOS field is denoted by the black dashed line. The right panel shows the positions of sources detected using blobcat in the 610 MHz mosaic. The blue rectangle shows the COSMOS field. Black dashed lines show the areas covered by individual pointings, while the red dashed lines show pointings that were excluded from the analysis. 25
- 2.3 The panels show the beam major and minor axes and the beam position angle for the GMRT 610 MHz pointings. The 1σ intervals for the respective beam parameters are shown as colored regions, with dashed lines showing their medians. 27
- 2.4 The left panel shows the peak-over-total flux ratio, S_P/S_T , as a function of the distance to the pointing center (d) for the 325 MHz map. Red dots show the medians of S_P/S_T for different d bins, with 1σ percentiles as error bars. The fitted [Bridle & Schwab \(1999\)](#) is shown by a blue line. The orange points show the skewness for different d bins, while the orange dashed line shows the overall skewness in this dataset. The right panel shows the total-over-peak flux ratio, S_T/S_P , as a function of the signal-to-noise ratio (S/N) for the 325 MHz map. The red line shows the fit we used to discern resolved sources. Sources above the red envelope were considered resolved. 28
- 2.5 The left panel shows the peak-over-total flux ratio, S_P/S_T , as a function of the S/N for the 610 MHz map with sources extracted using blobcat. Red dots show the medians of S_P/S_T for different S/N bins, with 1σ percentiles as error bars. The red dashed line shows the median S_P/S_T of all the data points, while the orange dashed lines shows the overall skewness in this dataset. The right panel shows the total-over-peak flux ratio, S_T/S_P , as a function of the S/N for the 610 MHz map after bandwidth smearing correction. The red line shows the fit used to discern resolved sources. 29

2.6	The panel shows the ratio of total fluxes detected in the 325 MHz map and in the Smolčić et al. (2014) map. The mean and the 1σ interval of the ratio are shown as vertical orange lines.	30
2.7	The panels show the astrometric offsets of the 325 MHz pointing positions to the 3 GHz catalog. The left panel shows the two-dimensional distribution of offsets. Dashed blue lines indicate the median offset in right ascension and declination, while the blue shaded region shows the 1, 2, and 3σ covariance ellipses. The middle and right panels show their respective right ascension and declination offset histograms with fitted Gaussians.	33
2.8	The panels show the astrometric offsets of the 610 MHz mosaic positions to the 3 GHz catalog. The left panel shows two-dimensional distribution of offsets. Dashed blue lines indicate the median offset in right ascension and declination, and the blue shaded region shows the 1, 2, and 3σ covariance ellipses. The middle and right panels show their respective right ascension and declination offset histograms with fitted Gaussians.	33
2.9	Ratio of expected flux at 610 MHz computed by assuming the spectral index between 325 MHz and 1.4 GHz, and the flux from the 610 MHz catalog. Bottom row shows the offset computed using the flux estimate based on the spectral index between 325 MHz and 3 GHz and red points show multicomponent sources. . .	35
2.10	Positional offsets in the GMRT 610 MHz map. Top panel shows the flux offset as a function the number of pointings that overlap at the position of a source. Bottom left panel shows how the offset depends on right ascension and declination, while the bottom right panel shows the variations in the local RMS values within the GMRT 610 MHz mosaic.	36

2.11	Euclidean normalized source counts for the GMRT 610 MHz catalog (solid black line), VLA-COSMOS 3 GHz source counts (Smolčić et al. 2017b), scaled using an 0.7 spectral index, XXL 610 MHz source counts (labeled as XXL-out and shown with a solid red line Smolčić et al. 2018). Garn et al. (2008) source counts are shown in pink, Ibar et al. (2008) source counts in brown, and Whittam et al. (2017) source counts in purple. The lower section of the plot shows source count ratios, limited to the flux density range from 10 mJy to 100 mJy.	39
2.12	Upper panels show the mean (left) and median (right) spectral indices $\alpha(610, 3000)$, estimated using survival analysis (red points) for various 3 GHz flux density bins. These spectral indices were fitted with a constant (solid horizontal line) and a linear model (dashed line). In the lower panels, the Euclidean normalized source counts for the GMRT 610 MHz catalog resulting from the constant spectral index model (left panel) and a linear spectral index model (right panel) are shown. Source count ratios are shown in the lower parts of the panels, with their estimated 16-84 percentile interval shown as shaded regions.	40
3.1	Flowchart of the radio SED fitting procedure described in Sect. 3.1. The input values are source fluxes, S , and rest-frame frequencies, ν . The log fluxes are then binned in log-rest-frame frequency bins. If there are no upper limits in a certain bin, the mean and standard deviation are calculated immediately, and if that is not the case, the log fluxes are converted into a right-censored dataset, and the Kaplan-Meier estimate is calculated. This estimate is then fit to a Weibull distribution, yielding the analytically determined means and standard deviations. The resulting different bins are then treated as data points with errors in both axes and are fit by a particular model by employing the orthogonal distance regression (ODR) method.	42

- 3.2 Results of simulations produced by varying the mean value of the input spectral index α_1 (labeled as α_1^{in}). The figure shows the interdependence of the following properties: the input spectral index α_1^{in} , the derived spectral index α_1^{out} , and the percentage of upper limits below 1 GHz. The left panel shows the dependence of the input spectral index, α_1^{in} , on α_1^{out} ; the middle panel shows the dependence of the $\alpha_1^{in}/\alpha_1^{out}$ ratio on the output spectral index, α_1^{out} ; and the right panel shows the dependence of the percentage of upper limits below 1 GHz on α_1^{in} . The solid lines show the means derived for different bins in the x-axes of their respective plot, while the colored intervals show the 1σ interval for the same bins. The red point shows the values of spectral index α_1 before and after correction, and the percentage of upper limits below 1 GHz, as presented in Sect. 4.3. The dashed lines are the equality lines. 45
- 4.1 Star formation rate vs. redshift for the “clean star-forming galaxy sample” (CSFG, black points), as defined by [Smolčić et al. \(2017a\)](#), and described in Sect. 4.1. Orange points indicate a subset of the CSFG sample that was detected at both 1.4 GHz and 3 GHz. Red points indicate the HSFG sample used here, i.e., the subset of the CSFG sample with an additional cut of the infrared-derived SFR, $SFR > 100 M_\odot/\text{yr}$. Histograms show the redshift and SFR distributions with the different subsamples colored as in the main figure. For greater clarity, the HSFG sample is marked by filled histograms, and its limits in the main figure are denoted by dotted red lines. 49
- 4.2 Number of detections in GMRT catalogs of sources in the HSFG samples. The gray area represents the sources that are not detected in the GMRT maps, while blue and orange areas represent sources detected at 325 MHz and 610 MHz, respectively. 51

-
- 4.3 Broken power-law parameter estimation based on the MCMC algorithm used in deriving the break frequency. The red lines and ellipses show the results of the corresponding ODR fit, while the black contours show the 1, 2, and 3σ contours of the MCMC samples. The left panel shows the four-parameter fit with the break frequency treated as a free parameter, while the right panel shows the three-parameter broken power-law fit derived by fixing the break frequency to the best-fit value of ν_b in the left panel. 54
- 4.4 Average SED of the star-forming galaxy sample. Gray data points show individual detections, yellow arrows show upper limits, green circles show means in bins with no upper limits, and magenta circles show mean values derived using survival analysis. The red shaded interval shows the broken power-law fit with its 1σ error confidence interval. The errors derived using survival analysis are the standard deviations of the Weibull distribution that was fit on the Kaplan-Meier survival function. 55
- 4.5 Mean properties of various rest-frame frequency bins in the HSFG radio SED. Shown are the mean redshift (left panel) and $\log SFR$ values (right panel) for each bin. Colored circles show the means of detections, while down-pointing arrows show the mean values for non-detections in each redshift bin. The dashed line shows the best-fitting broken power-law SED. 57
- 4.6 Average radio SED of HSFGs for the models from Sect. 4.4.1 plotted as in Fig. 4.4. The red solid lines and shaded intervals represent the best-fitting parameters of Table 4.1 and confidence intervals, respectively. 60
- 4.7 Left panel: Comparison of the average SED data (magenta points) and our broken power-law fit (magenta lines) with different literature SEDs ([Clemens et al. 2008](#); [Leroy et al. 2011](#)) for ULIRGs. For comparison, we show the [Condon \(1992\)](#) model for a normal SFG. Right panel: Comparison of the different goodness-of-fit tests for different models. We show the log-likelihood test and the Akaike and Bayesian information criteria. We give the average of these three criteria for reference. 61

- 4.8 Infrared-radio correlation, q_{TIR} , as a function of redshift for galaxies in the [Delhaize et al. \(2017\)](#) joint radio and infrared sample. We used the broken power-law SED from this paper for star-forming galaxies with an $SFR > 10 M_{\odot}/\text{yr}$ and the following SED shapes for $SFR < 10 M_{\odot}/\text{yr}$ ([Tabatabaei et al. 2017](#)): 1) a simple power-law SED with a spectral index of 0.79 (black line, K-correction 1) or a nonthermal spectral index of 0.97, and a 10% thermal fraction at 1 GHz (green line, K-correction 2). We show the [Delhaize et al. \(2017\)](#) relation for reference (magenta line). 65
- 4.9 Left panel: Distribution of sources in the $SFR - z$ plane, analogous to Fig. (4.1). Cyan points and magenta crosses indicate the distributions of disk- and spheroid-dominated subsamples of star-forming galaxies, as defined in [Molnár et al. \(2018\)](#). The 3σ contours of the CSFG sample are shown as black lines, and the orange rectangle marks the edges of the chosen nearly complete disk- and spheroid-dominated samples. The right panel shows their respective SEDs. 67
- 4.10 Left panel: Luminosity at a rest-frame frequency of 1.4 GHz for different redshifts computed using the fiducial value of $1 \mu\text{Jy}$ for (observer frame) 3 GHz flux densities, while the right panel shows the correction of 1.4 GHz radio luminosity, $C_{L_{1.4\text{GHz}}}$ computed using the spectral index of $\alpha = 0.7$ as reference. Solid lines are corrections based on either a broken power-law (red line), derived in Sect. 4.3 for our HSFG sample, and an SED (black line) of normal star-forming galaxies based on a 0.97 nonthermal spectral index and a 10% thermal fraction ([Tabatabaei et al. 2017](#)). The green line shows the SED of NSFGs based on a simple power law ($\alpha = 0.79$ [Tabatabaei et al. 2017](#)). 70

- 4.11 Average correction of $L_{1.4\text{ GHz}}$ for galaxies detected in the radio from the [Delhaize et al. \(2017\)](#) sample. The dashed black line connects corrections in different redshift bins derived by using our broken power-law SED for galaxies with an $\text{SFR} > 10 M_{\odot}/\text{yr}$, and an SED based on a 0.97 nonthermal spectral index and a 10% thermal fraction ([Tabatabaei et al. 2017](#)) for NSFGs ($\text{SFR} < 10 M_{\odot}/\text{yr}$). The dashed green line similarly connects points based on the broken power-law for an $\text{SFR} > 10 M_{\odot}/\text{yr}$ and a simple power-law SED for NSFGs ($\alpha = 0.79$ [Tabatabaei et al. 2017](#)). 73
- 5.1 Radio luminosity $L_{1.4}$ and redshift for RxAGN (black points). Red points correspond to the selected redshift and radio luminosity sample of RxAGN used in this work and are contained within $\log L_{1.4} \in [24, 26]$ and $z \in [0, 4]$. The histograms show the distribution of radio luminosity and redshift for all RxAGN and the RxAGN sample used in this work with black and red bars, respectively. 78
- 5.2 Mean completeness correction for the sample of RxAGN as a function of redshift. The mean completeness (solid line), with its corresponding standard deviation (shaded interval), were estimated for different redshift bins using the 3 GHz flux densities and interpolated completeness corrections for the VLA-COSMOS 3 GHz Large Project catalog (table 2 in [Smolčić et al. 2017b](#)) 80
- 5.3 The radio SED of RxAGN as normalized log-flux vs. rest-frame frequency for $z \in [0, 4]$ and $\log L_{1.4} \in [24, 26]$. A single power-law (left panel) and a broken power-law (right panel) models of the radio spectral energy distribution (SED) are shown as red lines with red confidence intervals. Detections are shown as grey points, upper limits as yellow arrows, bins without upper limits as green points and bins with upper limits as magenta points. The derived power-law spectral index is 0.64 ± 0.07 , while the broken power-law parameters are $\alpha_1 = 0.28 \pm 0.03$, $\alpha_2 = 1.16 \pm 0.04$ and $\nu_b = (4.1 \pm 0.2) \text{ GHz}$ 84

5.4	SED of the RxAGN sample with the model from Eq. 5.3 fitted. Upper panel shows the resulting model before applying the Manifold Boundary approximation method (MBAM) method, while the lower panel shows the best-fitting model after reducing the number of parameters with the MBAM method.	86
5.5	Behavior of logarithmic derivative of parameters along the geodesic curve (left panel) and the components of the FIM eigenvector corresponding to the smallest eigenvalue at the beginning (end) of the geodesic curve are shown in the middle (right) panel the model from Eq. 5.3.	87
5.6	Spectral indices derived for subsets of the RxAGN sample divided by redshift, z , and radio luminosity, $\log L_{1.4\text{GHz}}$, described in Sect. 5.4.2. The color-scale in the left panel shows the spectral index of the PL model, while the color-scales in the middle and right panels show the spectral indices α_1 and α_2 of the broken power-law model. Bins are outlined by black dashed lines.	88
5.7	SEDs derived for subsets of the RxAGN sample divided by redshift, z , and radio luminosity, $\log L_{1.4\text{GHz}}$. Shown is the best-fitting power-law model for each bin.	89
5.8	Dependence of the broken power-law spectral indices below and above a break frequency of 4 GHz (α_1 and α_2 , respectively) on the source size, $\log D$, for the subsets of the radio-excess active galactic nuclei (RxAGN) dataset for different values of $\log D$, with corresponding errors in spectral indices. The error bars for $\log D$ show the standard deviations of $\log D$ within each bin. The numbers indicate the bin number in table 5.2.	90
5.9	Correlation matrix for properties of subsets of the RxAGN sample. Colors indicate positive or negative Pearson correlation coefficient, written on the plot for each parameter pair with its corresponding p-value in parentheses. The considered variables in the correlation matrix are the 1.4 GHz radio luminosity, $\log L_{1.4}$, power-law spectral index α , broken power-law spectral indices α_1 and α_2 , and source size, $\log D$	91

5.10	Distribution of the broken power-law spectral indices for the subsets of the RxAGN sample. Black crosses are spectral indices derived for individual bins, listed in Tab. 5.2. Blue intervals denote α_1 while orange intervals denote α_2	92
5.11	SED of a sample of flat-spectrum sources, produced by selecting all sources having sizes less than 1 kpc. Red line shows the broken power-law model.	97
6.1	Schematic representation of infrared (I) and radio (R) log-luminosity parameter space (left panel) and its mapping to the $q - R$ space (right panel). Green region denotes detections, while blue and orange regions denote regions with non-detections.	100
6.2	The q - z trend determined using luminosity functions and survival analysis to account for non-detections in radio and infrared for different values of q_{min} (blue, orange and green lines). Colored intervals correspond to the 16th and 84th percentile of the q - z trend when derived from MCMC samples of parameters. The solid black line corresponds to the values without screening, while the dashed black line is the Delhaize et al. (2017) $q - z$ trend.	103
6.3	The limits of infrared (I_m) and radio (R_m) luminosity functions and the correlation coefficient, ρ , determined using MCMC.	104
6.4	The q probability distribution computed with (red line) and without screening (solid black line). Blue and orange lines correspond to upper and lower limits, respectively.	105
6.5	The q - z trend determined using luminosity functions and survival analysis, determined by fitting a Gaussian to the probability distribution, to account for non-detections in radio and infrared for different values of q_{min} (blue, orange and green lines). Colored intervals correspond to the 16th and 84th percentile of the q - z trend when derived from MCMC samples of parameters. The solid black line corresponds to the values without screening, while the dashed black line is the Delhaize et al. (2017) $q - z$ trend.	106

List of Tables

2.1	Summary of data reduction results of the GMRT maps. Columns b_{maj} [arcsec], b_{min} [arcsec], and BPA [°] show the beam major and minor axes and the beam position angle, respectively. Column <i>Sources</i> shows the number of sources that are detected toward the COSMOS field, column <i>Resolved</i> shows the number of resolved sources, column <i>FDR</i> shows the false-detection rate, column <i>Cross-matched</i> shows the number of sources that are present in the respective GMRT catalog and in the VLA 3 GHz catalog, and column <i>HSFG Sample</i> shows the number of sources in the subset of the GMRT catalog that is present in the highly star-forming galaxy sample described in Sect. 4.1. Percentages in the table are derived relative to the column <i>Sources</i>	26
4.1	Rankings of different fitted models with their parameters. For simplicity, we show models without their normalization parameter and indicate the additional contribution of free-free emission with a thermal fraction at 1GHz by ‘FFE’. We show the rankings based on the Akaike and Bayesian information criteria and the log-likelihood test ($\ln L$).	59

4.2	Average corrections of luminosity at 1.4 GHz needed if the K-correction was performed by assuming a power-law SED with a spectral index of 0.7. The corrections were derived for the average luminosity at 1.4 GHz, as described in Sect. 4.5, and are based on the assumption that galaxies with an $\text{SFR} > 10 \text{ M}_{\odot}/\text{yr}$ follow the broken power-law (BPL) SED and that galaxies with an $\text{SFR} < 10 \text{ M}_{\odot}/\text{yr}$ follow the SED based on Eq. (4.2), with the nonthermal spectral index and thermal fraction taken from Tabatabaei et al. (2017) . The percentage $p_{<10}$ is the percentage of 3 GHz flux that is due to galaxies with an $\text{SFR} < 10 \text{ M}_{\odot}/\text{yr}$. Columns of $p_{<10} = 0\%$ and $p_{<10} = 100\%$ are also exact corrections for single objects derived by assuming the BPL or the Tabatabaei et al. (2017) SEDs, respectively. The values in parentheses are correction $C_{L_{1.4\text{GHz}}}$ expressed in dex.	72
5.1	Summary of ANOVA results for the power-law and broken power-law spectral indices for RxAGN subsamples. For each model the significance of dependence of the spectral index on each of the listed parameters is determined from the p-value and the F-statistic. The considered parameters are: Type- if the sources in the bins were moderate-to-high luminosity RxAGN (RxHLAGN), low-to-moderate luminosity star-forming RxAGN (RxSMLAGN) or low-to-moderate luminosity quiescent RxAGN (RxQMLAGN), z - redshift, and $\log D$ - source size.	93
5.2	Parameters of the power-law and broken power-law models, and source size, $\log D$, derived for subsets of the RxAGN sample divided by redshift, z , and radio luminosity, $\log L_{1.4\text{GHz}}$, described by the mean and standard deviation of redshifts and radio luminosity for each bin. The sample is further split into RxHLAGN, RxQMLAGN, and RxSMLAGN. The numbers 1-6 in parentheses indicate bin labels in Fig. 5.8.	94

Contents

1	Introduction	1
1.1	Cosmology	1
1.2	Galaxies	3
1.2.1	Classification and origin	4
1.2.2	Star formation	6
1.2.3	Active Galactic Nuclei	8
1.2.4	AGN-host galaxy co-evolution	11
1.3	Radio spectra	12
1.3.1	Radio SED of SFGs	16
1.3.2	Radio SED of AGN	18
1.3.3	Radio as a star formation tracer	19
1.4	The VLA-COSMOS project	21
1.5	PHD thesis outline	21
2	Data	23
2.1	Available VLA data	23
2.2	Construction of GMRT catalogs	24
2.2.1	Observations and imaging	24
2.2.2	Source extraction	27
2.2.3	Bandwidth smearing	29
2.2.4	Resolved and unresolved sources	30
2.2.5	Multicomponent sources and deblending	31

2.2.6	False-detection rate	34
2.2.7	Astrometry	34
2.2.8	Final catalogs	34
2.3	Source counts and flux errors of the GMRT catalogs	35
3	Construction and models of the average radio SED	41
3.1	Construction of the average radio SED	41
3.2	SED fitting	44
3.3	Method verification through simulations	45
4	Average radio SED of highly star-forming galaxies	47
4.1	Sample	50
4.2	Methods	52
4.3	Results	55
4.4	Discussion	57
4.4.1	Shape of the radio SED	57
4.4.2	Infrared-radio correlation	64
4.5	K-correction considerations	68
4.5.1	Broken power-law	69
4.5.2	K-corrections and thermal fraction	70
4.5.3	Average K-corrections	71
4.6	Chapter summary	74
5	Average radio SED of active galactic nuclei	75
5.1	Sample	77
5.1.1	The 1.4 GHz selected sample	77
5.2	Methods	80
5.2.1	Construction of average radio SEDs	80
5.2.2	Description of synchrotron spectrum	81
5.2.3	Manifold Boundary Approximation Method	82
5.3	Results	84

5.4	Discussion	85
5.4.1	Possible cause of the SED shape	85
5.4.2	SED shape dependence on various observables	90
5.4.3	Flat spectrum sources	96
5.5	Chapter summary	97
6	Redshift dependence of the infrared-radio correlation	99
6.1	Methods	100
6.2	Results	103
6.3	Discussion	106
6.4	Summary	107
7	Summary and outlook	109

Chapter 1

Introduction

Ever since the realization that our Universe is expanding, the evolution of our universe has been one of the largest topics of interest in modern astrophysics. Contemporary research into this topic requires both the detailed knowledge of the nearby universe - used for understanding more distant objects - and acquiring ever deeper observations of the distant, high-redshift, universe. Even though the farthest observable in the universe is the Cosmic Microwave background radiation, current studies of the universe are limited to objects closer than the distance corresponding to the epoch of reionization. A panchromatic view of the sky, from X-ray to radio bands, has been proven paramount for understanding the evolution of galaxies and cosmic structures up to the epoch of reionization. The results described in this thesis are a step forward in understanding high-redshift populations of galaxies that will be observed with the next generation of telescopes.

1.1 Cosmology

Theoretical considerations about the shape of the universe started at the beginning of the 20th century by considering implications of the general theory of relativity. The [de Sitter \(1916\)](#) paper discussed the curvature of a sphere-shaped universe, while [Einstein \(1919\)](#) discussed the idea of a universe in which the matter density determines the time-independent curvature of the spherically symmetric universe. These two models were then encompassed into one by [Friedman \(1922\)](#).

By using Cepheids in nearby galaxies, [Hubble \(1929\)](#) established a linear relationship between the distance of a galaxy and its radial velocity out to 2 Mpc. This proportionality came to be known as the Hubble constant. [Lemaitre \(1931\)](#) soon pointed out that an increasing homogeneous universe could explain the [Hubble \(1929\)](#) relationship. Further development ([Robertson 1935](#); [Walker 1937](#)) gave rise to the Friedmann-Lemaitre-Robertson-Walker (FLRW) metric describing the expanding universe. This model possessed spherical symmetry but allowed for the possible overall curvature and expansion. Curvature in the FLRW metric is modeled by a dimensionless parameter K , which encompasses models of a sphere-shaped ($K = 1$), hyperbolic ($K = -1$) and a flat universe ($K = 0$). The overall expansion of the universe is modeled by the scale factor $a(t)$, scaling the spatial part of the FLRW metric. The scale factor yields two different measures of distances, the co-moving distance, χ and the proper distance, $a(t)\chi$. In the FLRW model, [Hubble \(1929\)](#) observations can thus be explained by the rate of change of the scale factor, which follows from the derivative of the proper distance. This rate of change, $\dot{a}(t)/a(t)$, is identified as the Hubble parameter $H(t)$ in the FLRW model. Its present-day values are denoted as H_0 .

[Adams \(1941\)](#) discovered CN molecular absorption lines interpreted by [McKellar \(1941\)](#) as consistent with the CN molecules being in a heat bath of 2.3 K. Independently from [Adams \(1941\)](#), by using microwave continuum observations, [Penzias & Wilson \(1965\)](#) discovered an excess of radiation at 3.5 ± 1.0 K (see, e.g., [Bennett 1995](#)). The discovered radiation was isotropic, unpolarized, and free from seasonal variations. [Dicke et al. \(1965\)](#) interpreted these results as CMB. The CMB radiation, shown in Fig. 1.1, is the source having the best-measured blackbody spectrum ([Fixsen et al. 1996](#); [Fixsen 2009](#)).

Even though the CMB spectrum exhibits no deviations, small anisotropies in intensity and polarization were found by the Cosmic Background Explorer (COBE) satellite ([Smoot et al. 1992](#)). The anisotropies have the frequency and spatial characteristics expected for primordial fluctuations and were found to be consistent with models of inflation, wherein fluctuations are created on small distance scales and expanded to large scales, eventually giving rise to an almost scale-free spectrum ([Bardeen et al. 1983](#)). These results were soon interpreted to be consistent with the cold dark matter models ([Efstathiou et al. 1992](#)).

Further experiments (de Bernardis et al. 2000; Balbi et al. 2000; Miller et al. 2002; Macias-Pérez et al. 2007) established that the universe was flat, leaving open the question of determining precisely other cosmological parameters. Perlmutter et al. (1999) analyzed data of 42 type Ia supernovae and found the mass contribution to the energy density content of the universe to be only $0.28^{+0.09}_{-0.08}$, with the remainder being interpreted as a positive cosmological constant (Λ) with very high accuracy. Further constraints have been provided by the Wilkinson Microwave Anisotropy Probe (WMAP) telescope (Kogut et al. 2003; Bennett et al. 2003) and, later, Planck (Aghanim et al. 2019), which strongly favor the Λ cold dark matter model (Λ CDM) model.

To summarize, we briefly list all the assumptions of the Λ CDM model, as outlined in Aghanim et al. (2019), and which are, or will become, testable by observations. The underlying assumption is that physics is the same throughout the observable Universe and General Relativity is an adequate description of gravity. On large scales, the Universe is found to be statistically the same everywhere and was once much hotter and denser and has been expanding since early times and possesses a trivial topology. The Universe consists of 1) dark energy, 2) pressure-less, stable and gravitationally interacting dark matter, 3) regular atomic matter, 4) photons and 5) neutrinos. The Universe has very small curvature, if any, and its density variations are Gaussian, adiabatic, and nearly scale invariant.

1.2 Galaxies

Even though there is no formal definition of a galaxy, Forbes & Kroupa (2011) proposed a definition of a galaxy to be a gravitationally bound system containing stars while requiring a two-body relaxation time greater than H_0^{-1} and a half-light radius greater than 100 pc, to exclude globular star clusters from the definition. A few galaxies, like the Andromeda galaxy and our Milky Way galaxy, can be observed by the naked eye and have thus been known to exist for a very long time, even though they were still considered to be nebulae (as evidenced in the Messier and the NGC catalogs, Messier 1781; Dreyer 1888). By determining the distances to nearby galaxies, Hubble (1925) determined that ‘spiral nebulae’ are extragalactic objects.

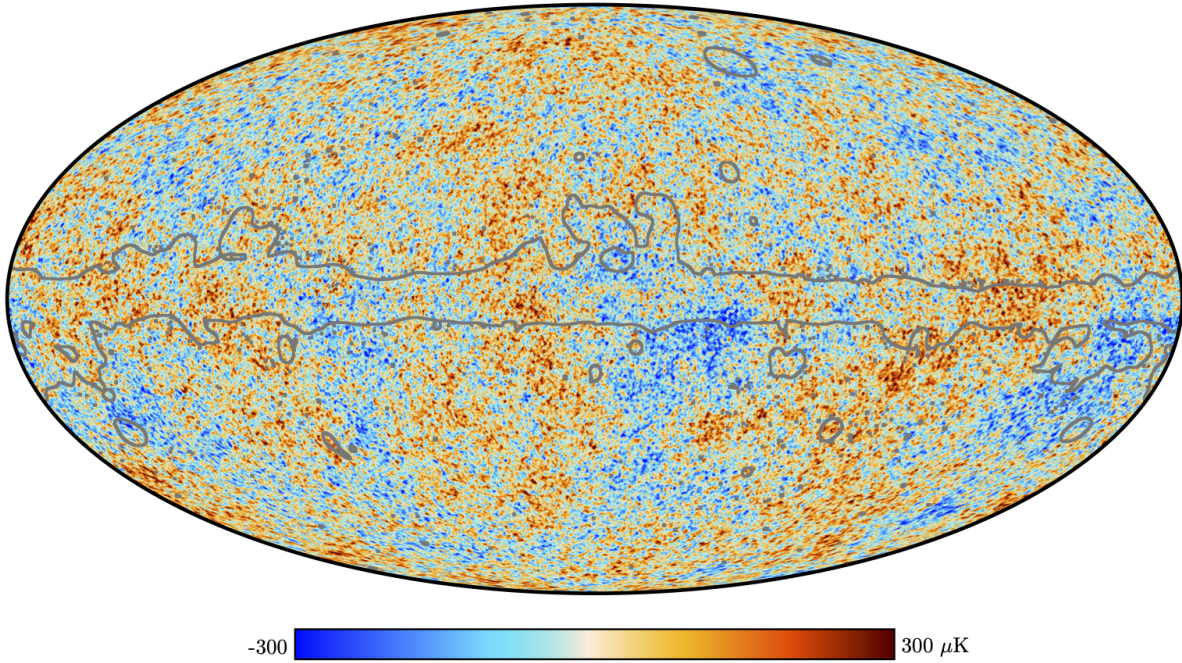


Figure 1.1: The CMB temperature map adapted from [Aghanim et al. \(2019\)](#).

1.2.1 Classification and origin

The first classification scheme for galaxies was proposed by [Hubble \(1926\)](#), dividing galaxies broadly by their shape into ellipticals, spirals and irregular galaxies. In the [Hubble \(1926\)](#) scheme, the elliptical category was further classified into subgroups $E1 - 7$, based on their ellipticity, while the spirals were separated by the presence of bulge into barred (SB) and those without an apparent bulge (S). The spiral categories S and SB were further divided into groups: early (Sa and SBa), intermediate (Sb and SBb), and late (Sc and SBc) types. [Hubble \(1926\)](#) noted that the naming of the groups, despite its temporal connotations, expresses the progression from simple to more complex forms of the spiral structure. In a further classification by [de Vaucouleurs \(1959\)](#), there are four classes (ellipticals E , lenticulars $S0$, spirals S , irregulars I), with the lenticular and spiral classes being divided first into two families, then into two varieties and finally into four stages. The families are retained from the [Hubble \(1926\)](#) classification, SA and SAB , depending on the presence of a central bulge and with intermediate objects classified as SAB . Each of the two families is further subdivided into ring-shaped (r) and spiral-shaped (s) varieties, depending on whether the spiral arms emerge from an inner circular ring. The early

to late progression is retained by the use of stages from early (*a*) to ‘very late’ (*cd*).

Explaining the provenience of galaxies with differing morphologies required complex numerical simulations. Since elliptical galaxies have simpler morphologies, first papers explaining the evolution of galaxies dealt with near-spherical elliptical galaxies. [Mathews & Baker \(1971\)](#) suggested that the gas in elliptical galaxies is lost due to heating by supernova explosions, while [Gallagher \(1972\)](#) considered efficient consumption of gas by continuing star-formation. [Larson \(1969, 1974a\)](#) performed the first numerical simulations of a two-fluid hydrodynamical model, taking into account both gas and stars, of the protogalaxy collapse reproducing the structure of nearby nearly-spherical elliptical galaxies. The model was later expanded to include the effects of supernovae ([Larson 1974b](#)), and to describe general axisymmetric galaxies ([Larson 1975](#)). Regarding spiral galaxies, [Eggen et al. \(1962\)](#) interpreted various correlations in the stellar motion in the galactic plane, namely between the chemical compositions of stars in the Milky Way, the eccentricity of their galactic orbits, their galactic angular momenta and the height they reach above the galactic plane, as a consequence of dynamics of a contracting protogalaxy condensing from a pregalactic medium. In their model, the protogalaxy started to condense out of intergalactic medium approximately 10 Gyr ago, with the collapse ending with the formation of a rotationally supported disk. [Lin & Shu \(1964\)](#) showed that density waves create a spiral gravitational field that underlies the observable concentration of young stars and the gas. [Larson \(1976\)](#) simulated the formation of disk galaxies by including a stage of slower star formation to allow the gas to settle in a disk shape.

Further numerical simulations yielded an interesting hierarchical model of structure formation in the Universe. [Toomre & Toomre \(1972\)](#) modeled the process of galaxy mergers which was able to explain the shape of irregular galaxies like the Antenna nebula and further argued that elliptical galaxies could actually be merger remnants. [White \(1978\)](#) carried out a simple simulation of merging wherein two spheroidal galaxies produced remnants with density profiles agreeing with observed elliptical galaxies, a result that was supported by further simulations (see, e.g., [Gerhard 1981](#); [Farouki & Shapiro 1982](#)). The first simulations had to consider spherical systems because of instabilities of self-gravitating disks, which were found to be stabilized by a heavy halo ([Ostriker & Peebles 1973](#)), and had problems reproducing giant elliptical galaxies

from mergers (Ostriker 1980). White & Rees (1978) proposed a two-stage theory of galaxy formation, wherein dark halos, made of ‘dark’ objects, form a potential well in which visible matter later condenses and invoked the Larson (1974b) feedback from supernovae and young stars that ejects a portion of the gas from the galaxy as star-forming processes start. Fall & Efstathiou (1980) explained the rapid rotation of galactic disks by dark matter halos that are at least five times more massive than the disk. A confirmation of dark matter came after the discovery of dark matter affecting the radial velocity profiles of galaxies (Rubin & Ford 1970; Rubin et al. 1978), which implied a massive, invisible, spherical halo around galaxies (Sancisi 1987). More detailed models can be divided into semi-analytical, that use the knowledge about the structure of the cold dark matter (CDM) model halos to model the gravitational potential wells encompassing and affecting galaxy evolution (White & Frenk 1991), and hydrodynamical models, which combine hydrodynamics and dark matter halos (Katz & Gunn 1991; Navarro & Benz 1991; Katz 1992; Navarro & White 1994).

1.2.2 Star formation

The rate of star formation varies along the Hubble sequence (Roberts 1963; Kennicutt 1983), an effect seen as a bimodality in galaxy colors, with the bluer colors being populated by late-type galaxies and red color with early-type galaxies (see, e.g., Mo et al. 2010). Determining the present and historic values of the star formation rate (SFR) is therefore important for understanding how galaxies evolved with cosmic time.

van den Bergh (1957) and Schmidt (1959) developed a simple model of the SFR in which the SFR is proportional to the gas density of the interstellar medium as a power law with the exponent of 1.4 (Kennicutt 1998b). A complication to this basic picture is the fact that in order to determine SFR, one needs to know the initial mass function (IMF). The simplest power law model of Salpeter (1955) of the IMF has been expanded to explain a wider range of stellar masses, which result in different scale factors for the SFR-gas density relation (Kroupa & Pavel 2001; Chabrier 2003).

Galaxies have been found to typically reside in the ‘main sequence’ of the stellar mass-SFR plane (Noeske et al. 2007; Elbaz et al. 2007, 2011). Galaxies can undergo a starburst

phase, which may be a result of a major merger (Sanders & Mirabel 1996). It has been found using simulations that mergers trigger starbursts, increasing star formation rate by two orders of magnitude (Mihos & Hernquist 1996). Lilly et al. (2013) developed a simple model in which a typical galaxy moves along a blue star-forming main sequence by increasing in mass by accreting cold gas from the cosmic web. As it approaches a critical mass, its gas supply is shut off and its star formation becomes quenched, a process which is still unclear (Heckman & Best 2014).

Many different tracers of star formation can be used, but require different calibrations. Kennicutt & Kent (1983) measured $H\alpha$ recombination line emission, which is proportional to the number of Lyman continuum photons emitted by massive stars. However, as noted in Kennicutt (1983), dust present in HII regions affects galaxy colors and therefore the star formation rate may be underestimated. Ultraviolet continuum radiation is another tracer of recent star formation (Buat et al. 1989), with the proportionality constant being dependent on the assumed initial mass function (Kennicutt 1998a). However, due to dust, an extinction correction of the order of a few magnitudes has to be applied (Buat 1992) and requires detailed knowledge of the extinction law (Calzetti et al. 1994). Interstellar dust absorbs UV light and re-radiates it in the infrared, making FIR emission a sensitive tracer of young stellar populations (Kennicutt 1997, 1998b).

Panchromatic measurements, from UV to infrared offer a way to interpret various galaxy properties via population synthesis models (Bruzual & Charlot 2003), as e.g. the MAGPHYS package (Da Cunha et al. 2008). Adopting a panchromatic view has become important for high redshift objects, since Madau et al. (1996, 1998) concluded that star formation rate density peaks about $z \sim 2$ and then begins to fall with higher redshift, as shown in Fig. 1.2. This result can be seen from both UV and infrared data, but UV estimates are an order of magnitude underestimated due to extinction (Madau & Dickinson 2014). Analyzing correlations between SFR tracers has therefore become important for future high redshift work (see, e.g., Hao et al. 2011; Mahajan et al. 2019).

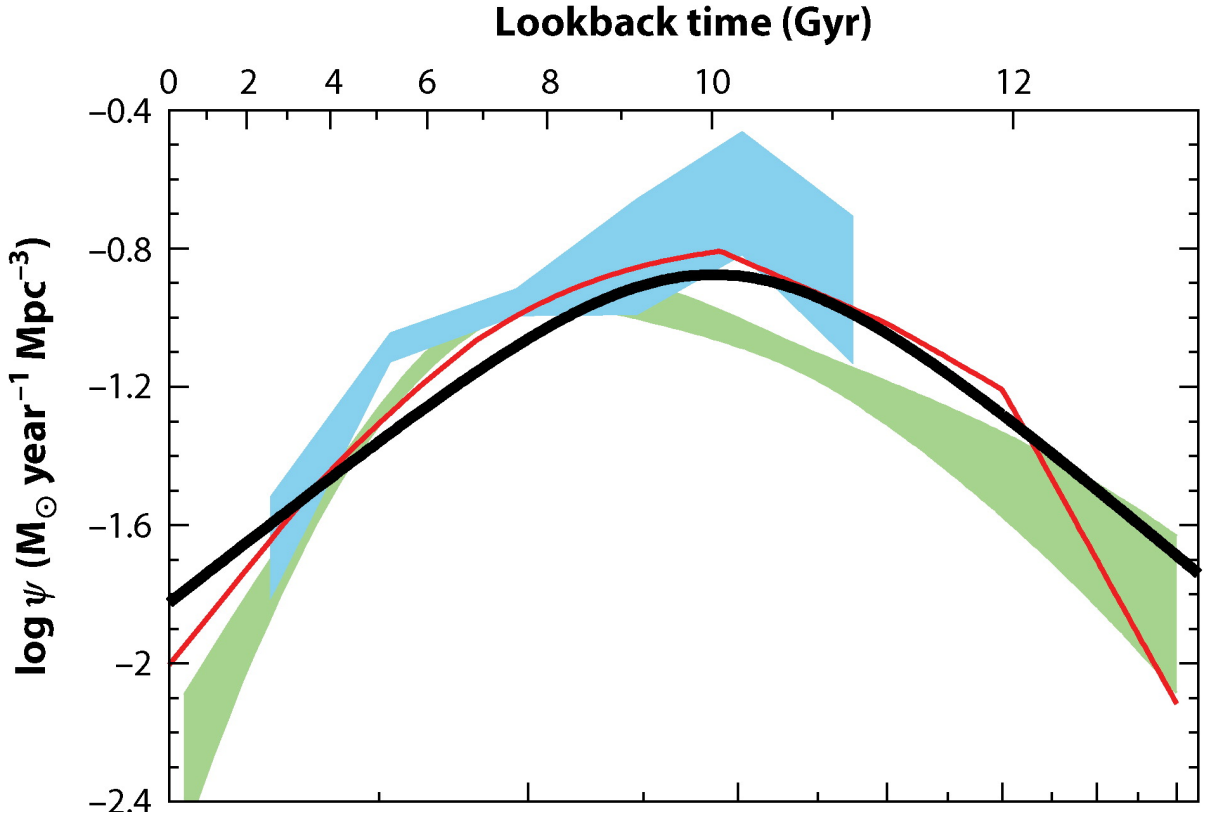


Figure 1.2: Comparison of the best-fit star-formation history (thick solid curve) with the massive black hole accretion history from X-ray [red curve [Shankar et al. \(2009\)](#)]. The shading indicates the $\pm 1\sigma$ uncertainty range on the total bolometric luminosity density. The comoving rates of black hole accretion have been scaled up by a factor of 3,300 to facilitate visual comparison to the star-formation history. Figure adapted from [Madau & Dickinson \(2014\)](#).

1.2.3 Active Galactic Nuclei

Processes that affect galaxy quenching are still unclear, but models explaining galaxy evolution require an additional component for explaining the physical properties of galaxies - an active galactic nucleus (AGN) ([Heckman & Best 2014](#)).

The supermassive black hole (SMBH) have long been suspected to be at the center of the AGN, with first indirect confirmation coming from mass estimates within the central parsecs of nearby elliptical and spiral galaxies ([Kormendy & Richstone 1995](#)). The direct confirmation came only recently by observing the shadow of SMBH in the center of the giant elliptical galaxy M87 ([Akiyama et al. 2019](#)).

AGN show a dichotomy of physical processes governing accretion onto the SMBH. In a radiative mode, SMBH accrete matter via a geometrically thin and optically thick accretion disk (Shakura & Sunyaev 1973), while in the jet mode the accretion disk is replaced by a geometrically thick advection-dominated accretion flow, wherein the bulk of the energy is carried in by the accreting gas as entropy rather than being radiated away (Narayan & Yi 1994). Therefore, AGN governed by the former (latter) mode have luminosities greater (smaller) than 1% of the Eddington luminosity¹ (Heckman & Best 2014). Judging by their luminosity ratios, these two modes are also labeled as radiatively efficient and radiatively inefficient AGN.

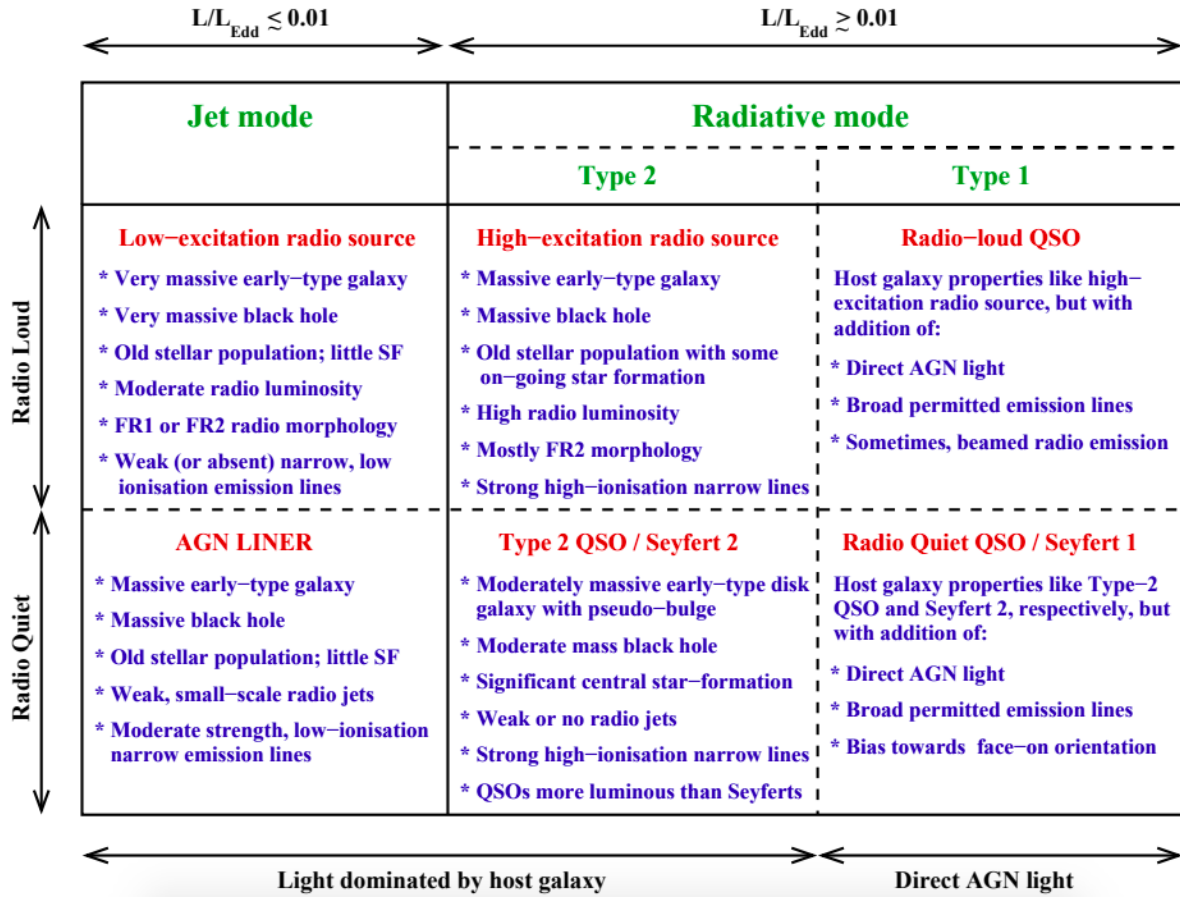


Figure 1.3: The categorization of the local AGN population. The blue text describes typical properties of each AGN class. Figure adapted from Heckman & Best (2014).

¹Defined as $L_{\text{Edd}} = 1.28 \times 10^{31} (M/M_{\odot}) \text{ W}$ (Sparke & Gallagher 2007).

Here we briefly describe a simple unification model of AGN ([Antonucci 1993](#); [Heckman & Best 2014](#)), summarized in Fig. 1.3. Radiatively efficient AGN can be classified into two Seyfert types ([Seyfert 1943](#)). [Seyfert \(1943\)](#) analyzed nuclei of nearby galaxies and found broad emission lines alongside absorption lines in their spectra, which lead to a conclusion that gas was being ejected from the nucleus at high velocities ([Burbidge et al. 1959](#)). Type I AGN show broad (1000 – 20000 km/sec) permitted and semi-forbidden emission lines and a bright central point source visible at all wavelengths, while type II sources contain strong narrow (300 – 1000 km/sec) emission lines, spanning from ultraviolet to near infrared frequencies ([Netzer 2015](#)). Independently, [Schmidt \(1963\)](#) observed a very luminous star-like (‘quasi stellar object’, QSO) object at a redshift of 0.158, a discovery which was later connected with earlier [Seyfert \(1943\)](#) finding. An interesting property of the QSOs was that they outshine their host galaxy in the radio by having their radio luminosities greater than $5 \times 10^8 L_{\odot}$ ([Sparke & Gallagher 2007](#)). These objects can be explained in a unified model of AGN ([Antonucci 1993](#)), wherein QSOs would be explained by high inclination angles with the AGN jet directly in our line of sight, while type I and type II AGN would correspond to objects with progressively smaller inclination angles with light passing through a narrow line or broad-line region, respectively. A further division can be made into radio loud and radio quiet sources, yielding High excitation radio sources (HERG, type II radio loud), radio loud QSOs (type I, radio loud), Seyfert II (type II, radio quiet), and Seyfert I (type I, radio quiet), as summarized in [Heckman & Best \(2014\)](#). The radiatively inefficient AGN into low-excitation radio sources (LERG, radio loud jet mode AGN) and low ionization narrow emission line AGN (LINERs, radio quiet jet mode AGN). [Netzer \(2015\)](#) point out that this simple unification scheme may be too simple to describe mergers.

In the radio spectrum, AGN emit non-thermal synchrotron radiation and can be classified by whether most of the emission arises from the central source (FR type I) or from the lobes (FR type II, [Fanaroff 1974](#)).

1.2.4 AGN-host galaxy co-evolution

[Kormendy & Richstone \(1995\)](#) found that black hole masses scale linearly with bulge blue luminosity, which was later strengthened by [Magorrian et al. \(1998\)](#), yielding a linear relation between black hole mass and bulge mass. [Ferrarese & Merritt \(2000\)](#) avoided statistical challenges ([Jaffe 1999](#)) which could arise from the large dispersion in the black hole mass-bulge luminosity relation by finding a tight correlation between black hole mass and bulge velocity dispersion. It is not yet understood whether these scaling relations were set in primordial structures or which physical processes established such correlations ([Madau & Dickinson 2014](#)).

Galaxy-galaxy mergers are a process that could affect both star formation and black holes. Using hydrodynamical simulations of galaxy-galaxy mergers [Di Matteo et al. \(2005\)](#) found that in addition to previously known ([Mihos & Hernquist 1996](#)) generation of a starburst, a galaxy-galaxy merger leads to strong inflows that feed gas to the SMBH, which in turn powers the quasar to expel gas and quench star formation and black hole growth. Using the relation between mass accretion rate onto the SMBH and bolometric luminosity function ([Sotan 1982](#)), yielded a striking alignment of the evolution of star formation rate density ([Madau et al. 1996](#)) and black hole accretion rate density ([Shankar et al. 2009](#)), as shown in Fig. 1.2. A possible explanation is the presence of a nuclear starburst ([Boyle & Terlevich 1998](#); [Silverman et al. 2008](#)).

It seems that feedback from a growing SMBH can occur in two distinct modes ([Alexander & Hickox 2012](#)). In the quasar mode (‘superwind mode’) feedback ([Kauffmann & Haehnelt 2000](#)), the cold gas reservoir is expelled from the AGN by means of AGN radiation and jets, while in the radio mode feedback the jets inject kinetic energy into the surrounding medium, heating it and therefore stopping star formation ([Croton et al. 2006, 2016](#)).

1.3 Radio spectra

The radio SED of sources in the frequency range of 1 – 10 GHz are often assumed to be described by a simple power-law, with a spectral index of $\alpha = 0.7$ (using the convention $S \sim \nu^{-\alpha}$, [Condon 1992](#)). The simple power-law shape of the radio SED is expected to be mainly due to synchrotron radiation, arising either from supernova remnants, tracing star formation, or from the vicinity of supermassive black holes, tracing AGN activity. A simple model of a galaxy's spectrum, covering infrared and radio frequencies is shown in Fig. 1.4.

However, the radio SEDs have been shown to exhibit deviations from these simple relationships, by having different spectral indices and complex spectral shapes (see, e.g., [Kukula et al. 1998](#); [Kimball & Ivezić 2008](#); [Clemens et al. 2008](#); [Leroy et al. 2011](#); [Calistro Rivera et al. 2017](#); [Galvin et al. 2018](#); [Tisanić et al. 2019](#)).

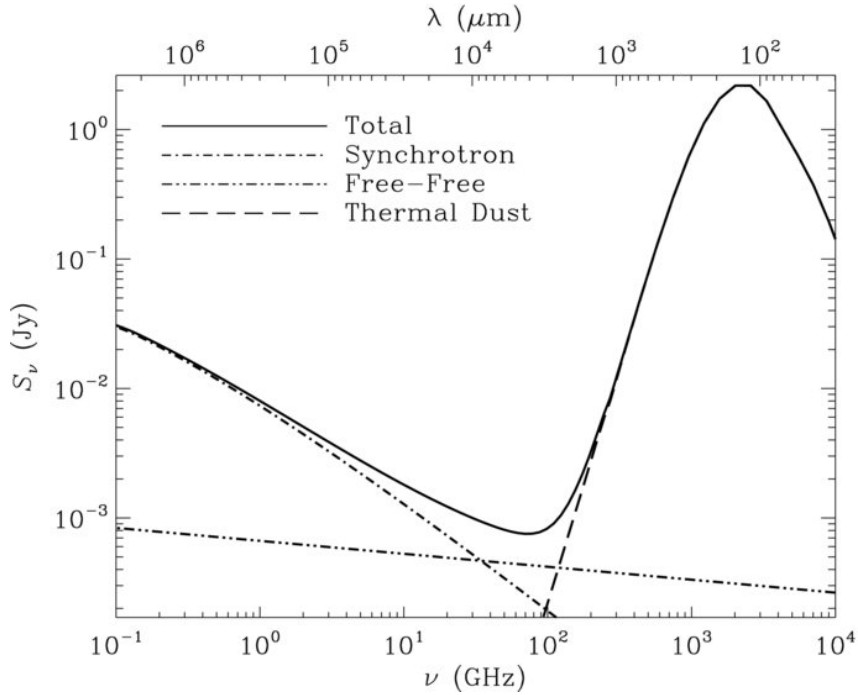


Figure 1.4: Model radio–FIR spectrum for a galaxy. Figure adapted from [Murphy \(2009\)](#).

Synchrotron emission

Synchrotron emission produces a non-thermal spectrum and is mostly due to diffuse electrons injected into the interstellar medium by core collapse SN events, with a small contribution of discrete sources like SN remnants (Bressan et al. 2002). The simplest description of synchrotron emission is by using a simple power law with a single spectral index, which is directly related to the synchrotron injection index. The mechanisms affecting the synchrotron spectrum can broadly be divided into those that shape the energy distribution of electrons and those that affect the light after emission.

The energy spectrum of relativistic electrons, $N(E)$, can initially be described by a single injection index, γ , $N(E) \sim E^{-\gamma}$, giving rise to a single power law SED with a spectral index $\alpha = (\gamma - 1)/2$. The electrons can be injected at one point in time (single injection model) or during a period of time (continuous injection models). Due to synchrotron and inverse Compton losses, usually described together as cosmic ray (CR) aging, the resulting SED starts to deviate from a simple power law. In the single injection model, the spectrum starts to develop features of a double power law, described by a spectral index of $(\gamma - 1)/2$ below $((2\gamma + 1)/3)$ above the break frequency, with the difference between the spectral indices being $\Delta\alpha = (\gamma + 4)/6$ (Kardashev 1962b). In the continuous injection model, this difference is independent of γ , $\Delta\alpha = 0.5$ (Kardashev 1962a). In this model, the spectral index below the break does not change with time, but the spectral index above the break steepens to $\gamma/2$. In both models, the surface brightness should behave as

$$S \propto \frac{\nu^{-\alpha}}{1 + \left(\frac{\nu}{\nu_b}\right)^{\Delta\alpha}}, \quad (1.1)$$

where ν_b is the break frequency. In the simplest case, where there are only synchrotron losses, the break frequency can be found using

$$\nu_b^{aging} = 11 \text{ GHz} \left(\frac{B}{\text{nT}}\right)^{-3} \left(\frac{t}{10 \text{ Myr}}\right)^{-2}, \quad (1.2)$$

where B is the strength of the galactic magnetic field and t the CR electron age (Pacholczyk 1977). Condon (1992) points out that the change in the spectrum is gradual, as can be seen from

the slope of the spectrum, i.e. the frequency-dependent spectral index

$$\alpha(\nu) = -\frac{d \lg S}{d \lg \nu} = \alpha + \Delta\alpha - \frac{\Delta\alpha}{1 + \left(\frac{\nu}{\nu_b}\right)^{\Delta\alpha}}, \quad (1.3)$$

yielding a difference in the spectral index from large frequencies to ν_b of only $\Delta\alpha/2$. This model does not produce a maximum in the spectrum, and forming a “knee” instead.

The electron energy spectrum can be modified by processes like inelastic scattering (free-free interactions), convective energy losses, Coulomb elastic scattering and ionization losses. These processes can be described by halo models, which can be divided into two categories. The first are the static halo models, that predict a spectrum without breaks and the second are the dynamic halo models, that predict breaks in synchrotron spectra of spiral galaxies (Pohl 1991). The latter further account for effects like diffusion, acceleration in random magnetic fields, radiative energy losses and adiabatic acceleration. More recent models even take into account variable star-formation history, which changes the amount of core-collapse supernovae that accelerate CR electrons, escape from the galactic halo due to convective winds, diffusion and adiabatic losses (Lisenfeld et al. 2004).

Free-free emission

Unlike synchrotron radiation which is more diffusely distributed within the galaxy, free-free emission is more concentrated towards brighter HII regions (Clemens et al. 1999; Bressan et al. 2002; Lisenfeld et al. 2004). For a sufficiently high electron temperatures (10 kK) the free-free emission in the \sim GHz range can be approximated by a simple power law with a spectral index of 0.1. This contribution can be included to the non-thermal part of the surface brightness as $S \propto (1 - f_{th})S^{NT} + f_{th}\nu^{-0.1}$, where f_{th} is the thermal fraction. The overall effect of the presence of free-free emission is that the spectrum becomes concave where synchrotron radiation is suppressed due to its power-law behavior.

The free-free emission produces a relatively flat spectrum, but due to the dominant non-thermal synchrotron contribution, it becomes important above ~ 10 GHz (Condon 1992). This is however not always the case. Bressan et al. (2002) discuss the radio SEDs of dusty starburst galaxies and conclude that if the *SFR* changes abruptly, the core-collapse SN rate will lag

behind due to the finite lifetime of stars, leading to a suppressed synchrotron emission in young starbursts. This effect can produce flat spectra below 10 GHz, as f_{th} is initially very large. [Prouton et al. \(2004\)](#) analyzed the behavior of thermal fraction with the age of the starburst. They found the thermal fraction to fall from the initial value of almost 100% to below 10% at 1.4 GHz within $10^{7.5}$ yr.

Processes affecting the emitted light

The unpolarized emitted radiation can be modified by three processes: Razin-Tsytovič (RT) effect ([Razin 1960](#)), synchrotron self-absorption, and free-free absorption. As will be explained below, we find that only free-free absorption is relevant above $\sim 0.5 - 1$ GHz.

The RT effect is caused by the increase of the refractive index of the medium due to the presence of weak plasma, resulting in a decreased effective Lorentz factor in the medium. In the presence of non-relativistic plasma, it becomes significant only below a frequency of

$$\nu_b^{RT} = 2 \text{ MHz} \left(\frac{n_e}{\text{cm}^{-3}} \right) \left(\frac{B}{\text{nT}} \right), \quad (1.4)$$

where n_e is the electron number density and B is the magnetic field strength.

The synchrotron self-absorption (SSA) is usually important below

$$\nu_{SSA} = 340 \text{ MHz} \left(\frac{S}{\text{Jy}} \right)^{2/5} \left(\frac{\theta}{\text{arcsec}} \right)^{-4/5} \left(\frac{B}{\text{nT}} \right)^{1/5}, \quad (1.5)$$

where θ is the source size. In the frequency range of 1 – 100 MHz it can become important if the brightness temperature of the source reaches 10 GK ([Condon et al. 1991](#)).

Free-free absorption produces a convex spectrum. It can either be due to a medium that is in the line of sight of the observer (i.e. in the foreground) or occur within the emitting region. The opacity in both cases is dependent on the electron temperature, T_e and the emission measure, EM ,

$$\tau_\nu = 8.3 \times 10^{-2} \left(\frac{T_e}{\text{K}} \right)^{-1.35} \frac{EM}{\text{pc cm}^{-6}} \left(\frac{\nu}{\text{GHz}} \right)^{-2.1} \quad (1.6)$$

Assuming the emitted light had an initial surface brightness, $S_0(\nu)$, the two cases can be described by

$$S_\nu = S_0(\nu) \begin{cases} e^{-\tau_\nu}, & \text{foreground} \\ \nu^{2.1}(1 - e^{-\tau_\nu}), & \text{within source.} \end{cases} \quad (1.7)$$

If S_0 can be modeled as a power law with spectral index α_0 , the behavior of these models affects in the frequency-dependent spectral index

$$\alpha(\nu) = -\frac{d \lg S}{d \lg \nu} = \alpha_0 - 2.1 \begin{cases} \tau_\nu, & \text{foreground} \\ \left(1 - \frac{\tau_\nu}{e^{\tau_\nu} - 1}\right), & \text{within source.} \end{cases} \quad (1.8)$$

Both models predict a maximum frequency, above which the spectral index is positive, but flatter than α_0 near the maximum and approaching α_0 farther from the maximum. The difference between these two models are more pronounced only at frequencies below the maximum frequency, where the spectral index becomes negative for both models, but has a minimum value of $\alpha_0 - 2.1$ for within-source absorption. [Galvin et al. \(2018\)](#) point out that for individual galaxies, one may find more than one star-forming region with different optical depths, producing a non-monotonous SED with multiple breaks.

1.3.1 Radio SED of SFGs

In this section we first describe how radio SEDs of star-forming galaxies (SFGs) have been found to behave for different SFRs, due to different contributions of free-free emission. To this end, we describe separately the “Normal” SFGs, with $SFR < 10 M_\odot/\text{yr}$ and (U)LIRGs, which have higher star-formation rates.

Normal star-forming galaxies

The typical SED of Normal SFGs ($SFR < 10 M_\odot/\text{yr}$) is described by a simple non-thermal power law with a spectral index of ~ 0.8 and a thermal fraction of $8 - 10\%$ ([Klein et al. 1988](#); [Condon & Yin 1990](#)). Below we describe how this simple picture might be influenced by different parameters, such as the galactic morphological type, SFR density, and magnetic field strength.

[Niklas \(1997\)](#) have derived mean values for the non-thermal spectral index versus morphological type, $\alpha_{NT} = 0.76 \pm 0.04$ for S_a Hubble type and its sub-type, S_{ab} , $\alpha_{NT} = 0.85 \pm 0.13$ for S_b and $\alpha_{NT} = 0.74 \pm 0.14$ for irregular galaxies. They argue that a flatter spectral index for early-type spirals comes from the emission of compact cores that may be present in them.

By using the KINGFISHER sample of nearby galaxies at $3 - 30$ Mpc ($z \approx 0.01$) with $SFR < 10 M_{\odot}/\text{yr}$, [Tabatabaei et al. \(2017\)](#) found the expected thermal fraction ($f_{th} = 10\%$), but with a steeper mean non-thermal spectral index. They find no correlation between these two parameters, but instead point out that the non-thermal spectral index flattens with increasing SFR density (see Sect. 6.1.1). They also found that the strength of the magnetic field rises for larger SFR s.

Highly star-forming galaxies

In contrast to normal SFGs, LIRGs and ULIRGs have much higher SFRs. One of the main differences to normal SFGs is that the electron lifetimes are shorter than in normal galaxies [Condon et al. \(1991\)](#). Extrapolating the [Tabatabaei et al. \(2017\)](#) relation, ULIRGs would also have higher magnetic field strengths compared to normal galaxies. They also do not have pronounced free-free emission and exhibit more flattening at lower frequencies. Some studies ([Clemens et al. 2008](#); [Leroy et al. 2011](#)) also indicate that the spectrum above 10 GHz might steepen instead of flatten, which cannot be explained even by complete suppression of free-free emission. Below we describe these recent studies of ULIRG and their conclusions.

[Clemens et al. \(2008\)](#) assessed the SED for a subsample of 40 ULIRGs from the IRAS Bright galaxy sample (BGS, [Condon et al. 1991](#), $z \leq 0.1$), that had detections in more than one radio frequency. They discussed the SEDs of individual sources, but also give the average properties. They found that the spectral index steepens with frequency, from $\alpha_{4.8}^{1.4} = 0.521$ for the 1.4 – 4.8 GHz range, to a gradually steeper spectrum: $\alpha_{8.4}^{4.8} = 0.698$ and $\alpha_{22.5}^{8.4} = 0.813$. Between the two largest observed frequencies, they found an even steeper spectral index of $\alpha_{22.5}^{15} = 0.842$. While the average spectral index flattens at a lower frequency, they comment that there are sources in their sample that show only free-free absorption or free-free emission, which they explain by the varying compactness of HII regions in different galaxies. Using the foreground screen model, described in the previous section, smaller HII regions have higher densities than more extended regions and therefore smaller regions absorb more light than large ones. After analyzing the low-frequency GMRT observations of the same sample of galaxies, they point out that the free-free absorption effect can be explained if the They could not explain

the steepening at higher frequencies with the available data. They tried to explain this effect using the continuous injection model. While this model has a small $\Delta\alpha \approx 0.5$, they argue that the exact shape of the radio SED would be susceptible to stochastic effects. They, however, do not expect these effects to be important in the integrated spectrum of the whole galaxy, as effects such as radio hypernovae contribute only a few percent to the total flux of the galaxy (Lonsdale et al. 2006). They argue that, while the convective winds and rapidly varying SN rate, introduced in the Lisenfeld et al. (2004) model, could explain the steeper spectral index above ~ 10 GHz, the electron lifetimes of ~ 10 kyr reported by Condon et al. (1991) do not leave enough time for either winds to push electrons or the SN rate to change significantly.

Leroy et al. (2011) observed 22 brightest nearby ULIRGs from the IRAS BGS sample. They find the spectral index above 4 GHz of 0.67 ± 0.15 , which was in agreement with Condon et al. (1991), while they also find deviations from a simple power law at low (~ 1 GHz) and high (> 10 GHz) frequencies. They suspect that the modified injection index is the probable cause of the high-frequency behavior, but comment that AGN might dominate the high-frequency spectrum of the steepest sources in their sample.

A more recent study conducted by Galvin et al. (2018) investigated the SED of nearby LIRGs ($z < 0.23$). They found a steep non-thermal spectral index $\alpha = 1.06$, which they associate with a steeper injection index of the CR distribution. They also find that the low-frequency SEDs exhibit multiple free-free absorption turnover frequencies, due to different compositions of star-forming regions within the individual galaxies.

1.3.2 Radio SED of AGN

Quasars have been shown to have spectral indices in the 1 – 10 GHz range that may be either steep (>0.5) or flat (<0.5) (Kukula et al. 1998). At 150 MHz, Toba et al. (2019) find an even greater variety in radio spectral indices, ranging from 0.5 to 2.5. The shape of the radio SED of individual sources at higher frequencies is related to the synchrotron aging process and additionally to free-free emission in star-forming galaxies, while lower-frequency part of the spectrum may be influenced by the different absorption processes (see, e.g., Condon 1992). In bright samples (~ 1 Jy), alongside flat-spectrum sources ($\alpha < 0.5$), a significant fraction

(40 – 50%) shows either a steeper SED ($\alpha > 0.5$), or a peaked or inverted spectrum, (Kapahi 1981; Peacock & Wall 1982; De Zotti et al. 2010). Kimball & Ivezić (2008) found that individual SEDs of complex and resolved sources (at a 5 arcsec resolution) are best described by a spectral index of ~ 0.8 , while unresolved sources have a flat spectral shape ($\alpha \sim 0$). They point out that emission from extended radio lobes tends to be steeper, while flatter emission might arise from compact quasar cores/jets due to self-absorbed synchrotron emission. Synchrotron aging is usually described either assuming a single injection of electrons with a constant or isotropic pitch angle, or assuming continuous injection of electrons (Kardashev 1962b; Jaffe & Perola 1973; Pacholczyk 1977). Absorption processes affecting the SED shape are synchrotron self-absorption and free-free absorption, which have been used to explain radio spectra of gigahertz peaked-spectrum and compact steep-spectrum sources (O’Dea 1998; Collier et al. 2018). O’Dea & Baum (1997) found that the source size for these types of sources is negatively correlated with turnover frequency in their spectra (Fanti et al. 1990; O’Dea & Baum 1997), while sources have been found with turnover frequencies above 10 GHz (Edge et al. 1998). By using The Low-Frequency Array (LOFAR) observations, Calistro Rivera et al. (2017) find statistically significant steepening in their AGN SED in the 150 MHz – 600 MHz range compared to the AGN SED around 1 GHz. Previous studies of radio SEDs of individual sources find that the average value of the spectral index is consistent with the expected value of $\alpha = 0.7$ (e.g., Kukula et al. 1998; Toba et al. 2019).

1.3.3 Radio as a star formation tracer

It has been found that the infrared and radio luminosities are bound by a tight correlation over many orders of magnitude (van der Kruit 1971; Helou et al. 1985; Condon 1992). This infrared-radio correlation, defined by the so-called q parameter, provides the basis for radio luminosity as a star-formation tracer, by connecting it to the better-understood infrared luminosity, which is linked to SFR (Kennicutt 1998b). Radio luminosities have the potential of being good tracers of star formation because emission in star-forming galaxies below ~ 30 GHz is unbiased by dust (Condon 1992).

In the calorimeter model (Voelk 1989), q is expected to be constant over a wide range of

magnetic field strengths due to electrons losing their energy because of synchrotron and inverse Compton losses. This produces a tight correlation, even though individual galaxies may show deviations.

Analytic considerations (Murphy 2009), predict q to increase with redshift, mostly due to the synchrotron electrons' inverse Compton scattering off cosmic microwave background photons. Recent stacking and survival analysis studies find q to be decreasing with increasing redshift (Ivison et al. 2010; Magnelli et al. 2015; Delhaize et al. 2017; Calistro Rivera et al. 2017). The interpretation of the $q - z$ studies is complicated by the necessary conversion of radio fluxes to radio luminosities. This conversion, called the K-correction, requires assumptions on the shape of the radio SED. Delhaize et al. (2017) point out that the computation of rest-frame radio luminosity via a K-correction using a simple, single power-law assumption of the star-forming galaxies' SED could possibly cause declining q - z trend, which was further investigated by Tisanić et al. (2019, see chapter 4), finding that the SEDs probably do not cause such a trend.

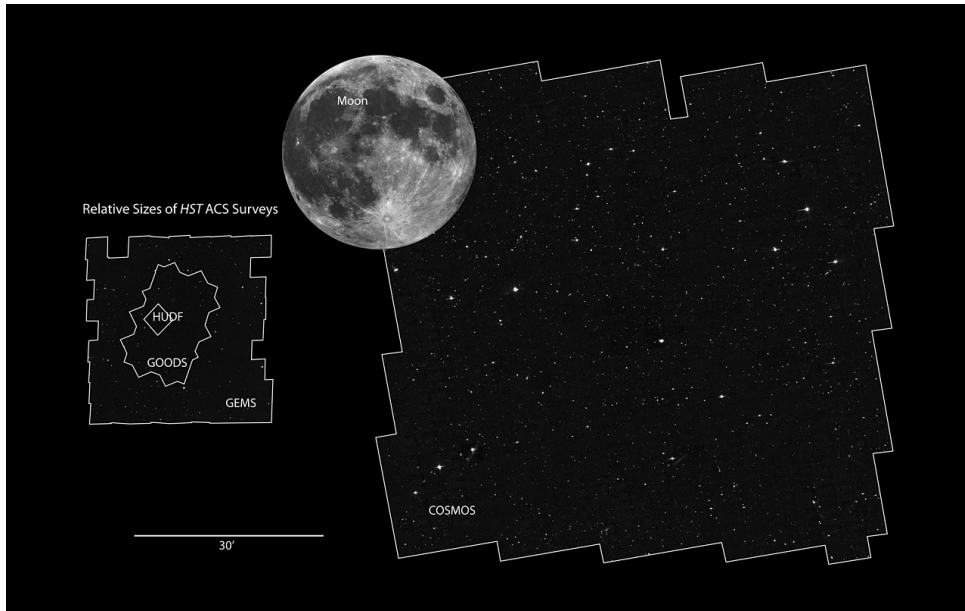


Figure 1.5: Visualization of the covering area of the COSMOS field, adapted from www.spacetelescope.org/images/heic0701f. Credit: NASA, ESA and Z. Levay (STScI).

1.4 The VLA-COSMOS project

Cosmological Evolution Survey (COSMOS) is a panchromatic survey of a 2 square degree field (Fig. 1.5) in the constellation Sextans, that was designed to addresses 1) the assembly of galaxies, clusters, and dark matter 2) reconstruction of the dark matter distributions and content 3) the evolution of galaxy morphology, galactic merger rates, and star formation 4) evolution of AGN and the dependence of black hole growth on galaxy morphology and environment, and 5) the mass and luminosity distribution of the earliest galaxies, AGNs, and intergalactic gas, all in a broad redshift range $z \in \langle 0.5, 6 \rangle$ (Scoville et al. 2007).

The largest panchromatic catalog covering the COSMOS field published to date is the COSMOS2015 catalog (Laigle et al. 2016), a catalog comprising of 30 photometry bands covering both optical and near infrared frequencies in addition to precise photometric redshifts for over half a million objects within the COSMOS field.

At radio frequencies, there exist the VLA and GMRT maps of the entire COSMOS field (Schinnerer et al. 2007, 2010; Smolčić et al. 2014, 2017b; Tisanić et al. 2019). Schinnerer et al. (2007, 2010) published two iterations of the radio catalog of the COSMOS field centered at 1.4 GHz, observed by the Karl G. Jansky Very Large Array (VLA), while Smolčić et al. (2017b) observed the same field at 3 GHz. Sub-GHz frequencies are covered by the Smolčić et al. (2014) VLA catalog at 324 MHz and with two GMRT catalogs at 325 MHz and 610 MHz (Tisanić et al. 2019, see chapter 4).

1.5 PHD thesis outline

The objective of this dissertation is to constrain the radio SED in the GHz range of different populations of galaxies in the COSMOS field.

The aim of the project is to construct average radio SEDs of galaxies as a function of various properties (including, SFR, the q-parameter and AGN classifications). This would provide a major step forward in understanding the average radio SEDs of various populations detected in deep radio surveys, such as the COSMOS survey, particularly given that major radio observations with next-generation radio interferometers are already in their early stages (see, e.g, Norris et al.

2013; Prandoni & Seymour 2015).

This PHD thesis is based on one published paper (chapters 2-4 [Tisanić et al. 2019](#)), one submitted paper (chapter 5) and one paper in preparation (chapter 6). Chapter 2 focuses on the construction of the GMRT COSMOS catalogs, chapter 3 focuses on the method used in constructing average radio SEDs, chapter 4 applies this method for constructing the average SED of highly star-forming galaxies, chapter 5 on the radio SED of AGN, while chapter 6 analyzes high redshift behavior of the infrared-radio correlation. Chapters 2-4 contain text, tables and figures presented as they appeared in the version of the [Tisanić et al. \(2019\)](#) before signing-off of copyright, with little adaptation.

Chapter 2

Data

The following chapter focuses on describing the multiwavelength radio observations used in constructing the radio SEDs. Sect. 2.1 describes the 1.4 GHz and 3 GHz observations of the COSMOS field ([Schinnerer et al. 2007, 2010](#); [Smolčić et al. 2017b](#)), while sect. 2.2 focuses on construction of the GMRT catalogs, as presented in [Tisanić et al. \(2019\)](#). Sect. 2.3 describes construction and comparison of Giant Meterwave Radio Telescope (GMRT) source counts.

2.1 Available VLA data

The VLA COSMOS 3 GHz Large Project map ([Smolčić et al. 2017b](#)) was constructed from 384 hours of observations of the 2 deg^2 COSMOS field. Observations were carried out over 192 pointings in the S-band with VLA in A and C antenna configurations. This was a wide-band observation with a total bandwidth of 2084 MHz derived from 16 spectral windows, each 128 MHz wide. The final mosaic reached a median root-mean-square (RMS) of $2.3 \mu\text{Jy}/\text{beam}$ at a resolution of 0.75 arcsec. Considering the large bandwidth and the volume of the data, each pointing was imaged separately using the multi-scale multi-frequency synthesis algorithm (hereafter MSMF, [Rau & Cornwell 2011](#)) and then combined into a single mosaic. The MSMF algorithm had been found to be optimal for both resolution and image quality in terms of the RMS noise and sidelobe contamination ([Novak et al. 2015](#)). The 3 GHz catalog has been derived using BLOBCAT ([Hales et al. 2012](#)) with a 5σ threshold. In total, 10830 sources were recovered

(67 of which were multi-component sources). For more details, see [Smolčić et al. \(2017b\)](#).

The 1.4 GHz catalog is a joint catalog comprised of the VLA COSMOS 1.4 GHz Large ([Schinnerer et al. 2007](#)) and Deep surveys ([Schinnerer et al. 2010](#)). The joint catalog was constructed by combining the observations of the central $50 \text{ arcmin} \times 50 \text{ arcmin}$ subregion of the COSMOS field (VLA-COSMOS Deep Project [Schinnerer et al. 2010](#)) at a resolution of $2.5 \text{ arcsec} \times 2.5 \text{ arcsec}$ and previously published observations of the entire 2 deg^2 COSMOS field at a resolution of $1.5 \text{ arcsec} \times 1.4 \text{ arcsec}$ (VLA-COSMOS Large Project [Schinnerer et al. 2007](#)). The average RMS in the resulting map was found to be $12 \mu\text{Jy}$. The large survey consisted of 240 hours of observations over 23 pointings spread out over the entire COSMOS field in the L band centered at 1.4 GHz and with a total bandwidth of 37.5 MHz in VLA A configuration and 24 hours in the C configuration. [Schinnerer et al. \(2010\)](#) supplemented the 7 central pointings with an additional 8.25 hours of observations per pointing using the A configuration and the same L-band configuration. These new measurements were then combined in the uv-plane with the Large Project observations. The joint catalog was constructed by using the SExtractor package ([Bertin & Arnouts 1996](#)) and the AIPS task SAD, yielding 2865 sources ([Schinnerer et al. 2010](#)).

2.2 Construction of GMRT catalogs

Here we describe the calibration, imaging, source extraction, and validation (including all of the corrections applied) of the GMRT 325 and 610 MHz data.

2.2.1 Observations and imaging

The GMRT observations of the 2 deg^2 COSMOS field were conducted using 30 antennas, their longest baseline being 25 km. The channel width of observations was 125 kHz, with a total bandwidth of 32 MHz. The observations were reduced with the source peeling and atmospheric modeling pipeline (SPAM, described in detail in [Intema et al. 2017](#)). It accounts for radio interference at low radio frequencies and for direction-dependent effects, such as ionospheric dispersive delay.

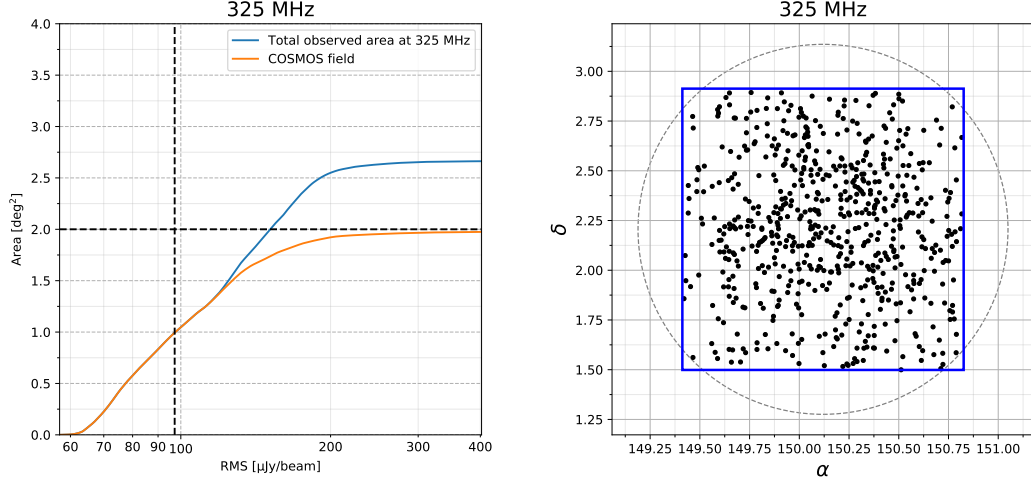


Figure 2.1: The left panel shows the visibility function for the entire 325 MHz map (blue line) and the 2 deg^2 COSMOS field (orange line). The median RMS within the COSMOS field is denoted by the black dashed line. The positions of sources detected using blobcat in the 325 MHz map are shown in the left panel. The blue rectangle denotes the 2 deg^2 COSMOS field, while the dashed circle shows the pointing half-power radius.

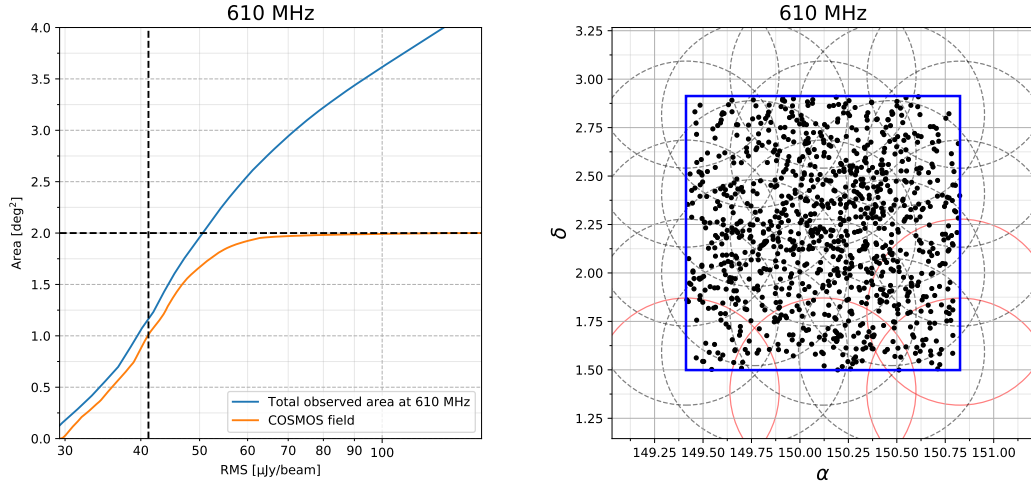


Figure 2.2: The left panel shows the visibility function for the entire 610 MHz map (blue line) and the 2 deg^2 COSMOS field (orange line). The median RMS within the COSMOS field is denoted by the black dashed line. The right panel shows the positions of sources detected using blobcat in the 610 MHz mosaic. The blue rectangle shows the COSMOS field. Black dashed lines show the areas covered by individual pointings, while the red dashed lines show pointings that were excluded from the analysis.

Table 2.1: Summary of data reduction results of the GMRT maps. Columns b_{maj} [arcsec], b_{min} [arcsec], and BPA [$^{\circ}$] show the beam major and minor axes and the beam position angle, respectively. Column *Sources* shows the number of sources that are detected toward the COSMOS field, column *Resolved* shows the number of resolved sources, column *FDR* shows the false-detection rate, column *Cross-matched* shows the number of sources that are present in the respective GMRT catalog and in the VLA 3 GHz catalog, and column *HSFG Sample* shows the number of sources in the subset of the GMRT catalog that is present in the highly star-forming galaxy sample described in Sect. 4.1. Percentages in the table are derived relative to the column *Sources*.

Map	b_{maj} [arcsec]	b_{min} [arcsec]	BPA [$^{\circ}$]	Sources	Resolved	<i>FDR</i>	Cross-matched	HSFG Sample
325 MHz	10.8	9.5	-62.8	634	177 (28.0%)	3.0%	567 (89.6%)	29
610 MHz	5.6	3.9	65.5	999	196 (19.6%)	1.3%	870 (87.1%)	52

The 325 MHz observations were carried out in a single pointing (see the right panel of Fig. 2.1) under the project 07SCB01 (PI: S. Croft). The observations were allocated 45 hours in total and comprised four observations with an average time per observation of ~ 120 min and a total time on target of ~ 40 hours. Data reduction and imaging were performed using the SPAM pipeline, with the final map being imaged at a resolution of 10.8×9.5 arcsec². A primary beam correction was then performed using the parameters from the GMRT manual. The RMS as a function of fractional area is shown in the left panel of Fig. (2.1). We find a median RMS of $97 \mu\text{Jy}/\text{beam}$ over the $\sim 2 \text{ deg}^2$ COSMOS field, uniformly rising toward the edges of the map.

The 610 MHz observations were carried out over 19 pointings (see the right panel of Fig. 2.2) under the project 11HRK01 (PI: H. R. Klöckner). The observations were allocated 86 hours in total and were spread over eight observations with an average time on source of ~ 4 hours per pointing. We found that four pointings (labeled 14, 16, 22, and 23) deviated by more than 2σ from the mean beam axes and beam position angles, and these were therefore excluded. The beam properties of the remaining pointings are shown in Fig. (2.3). After excluding the four pointings, we used one common restoring beam for the remaining pointings. The pointing images were imaged at a common resolution of 5.6×3.9 arcsec². A primary beam correction was then performed on each pointing image before we combined them into one mosaic using the

parameters from the GMRT manual, following the procedure outlined in Smolčić et al. (2018). The RMS as a function of fractional area is shown in the left panel of Fig. (2.2), yielding a median RMS of $39 \mu\text{Jy}/\text{beam}$ over the 2 deg^2 COSMOS field.

A summary of the GMRT data reduction statistics can be found in Table (2.1). Below we describe the source extraction method, reliability tests, and corrections we applied to the catalogs.

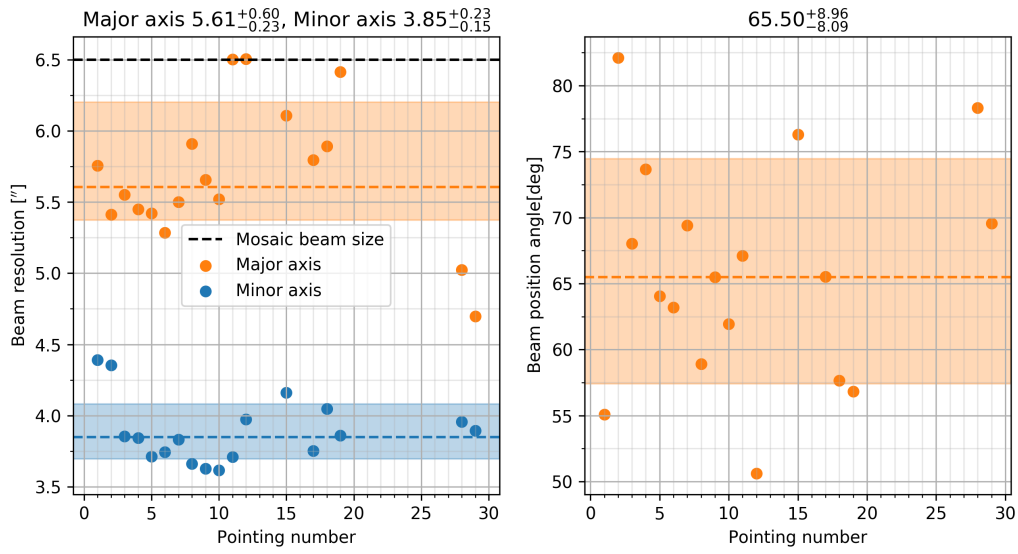


Figure 2.3: The panels show the beam major and minor axes and the beam position angle for the GMRT 610 MHz pointings. The 1σ intervals for the respective beam parameters are shown as colored regions, with dashed lines showing their medians.

2.2.2 Source extraction

BLOBCAT (Hales et al. 2012) was used to extract sources down to five times the local RMS value (5σ) in each map. The local RMS values were taken from the RMS map produced by the AIPS task RMSD. We used default BLOBCAT input parameters except for the minimum blob size, which was set to 3 pixels in right ascension and declination, as described in Smolčić et al. (2017b). Even though the imaged pointing extends beyond the COSMOS field, we restricted the catalog and further analysis to the 2 deg^2 COSMOS field.

We find 633 source components in the 325 MHz map and 999 source components in the 610 MHz map. After accounting for multicomponent sources and blending, the number of sources in the COSMOS field is 633 (see below for details) in the 325 MHz map, while the number of sources remaining in the 610 MHz map is 986. All of the sources detected by BLOBCAT within the 2 deg^2 COSMOS field are shown in the right panels of Figs. (2.1) and (2.2). Below we describe the various tests and corrections performed to generate the final source catalogs.

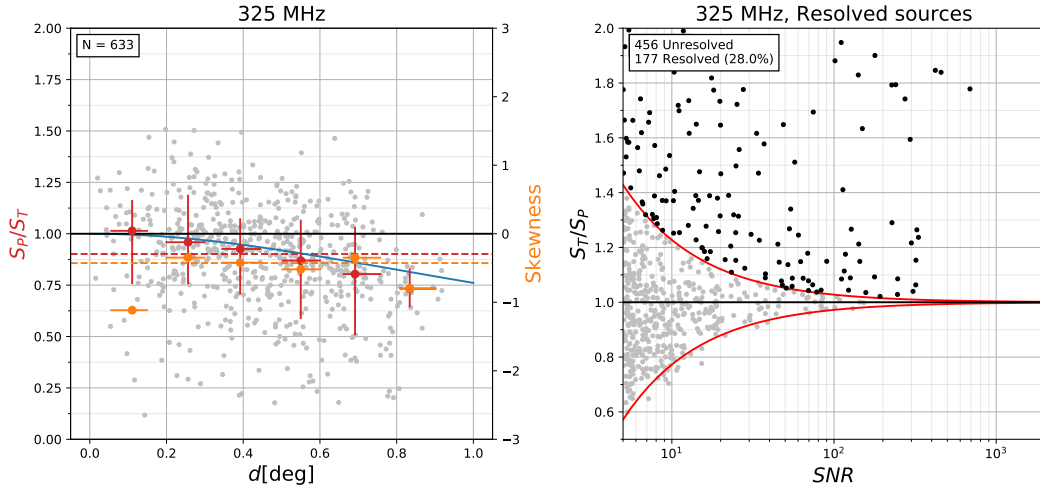


Figure 2.4: The left panel shows the peak-over-total flux ratio, S_P/S_T , as a function of the distance to the pointing center (d) for the 325 MHz map. Red dots show the medians of S_P/S_T for different d bins, with 1σ percentiles as error bars. The fitted [Bridle & Schwab \(1999\)](#) is shown by a blue line. The orange points show the skewness for different d bins, while the orange dashed line shows the overall skewness in this dataset. The right panel shows the total-over-peak flux ratio, S_T/S_P , as a function of the signal-to-noise ratio (S/N) for the 325 MHz map. The red line shows the fit we used to discern resolved sources. Sources above the red envelope were considered resolved.

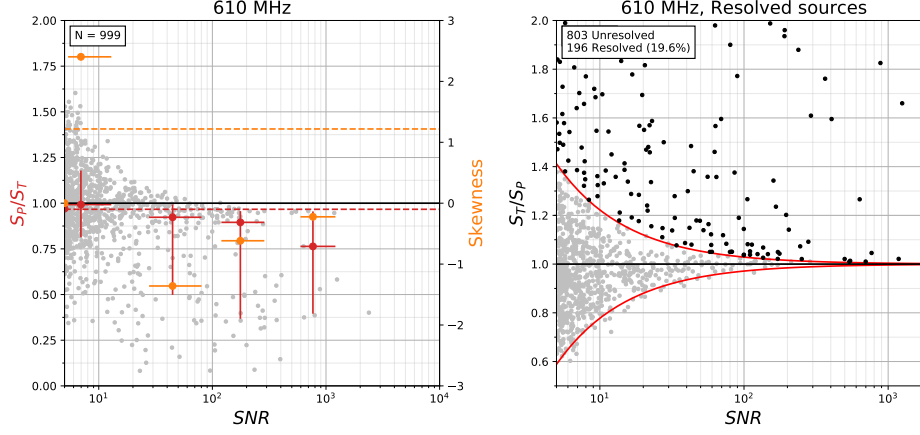


Figure 2.5: The left panel shows the peak-over-total flux ratio, S_P/S_T , as a function of the S/N for the 610 MHz map with sources extracted using blobcat. Red dots show the medians of S_P/S_T for different S/N bins, with 1σ percentiles as error bars. The red dashed line shows the median S_P/S_T of all the data points, while the orange dashed lines shows the overall skewness in this dataset. The right panel shows the total-over-peak flux ratio, S_T/S_P , as a function of the S/N for the 610 MHz map after bandwidth smearing correction. The red line shows the fit used to discern resolved sources.

2.2.3 Bandwidth smearing

Given the finite bandwidth of the map, a certain amount of bandwidth smearing is expected. To assess the effect of bandwidth smearing on the extracted fluxes, we computed the peak-over-total flux ratio, S_P/S_T .

For the 325 MHz map, which consists of only one observed pointing, in the left panel of Fig. (2.4) we show the S_P/S_T ratio as a function of the distance to the pointing center. Bandwidth smearing reduces the value of peak fluxes compared to the total fluxes with increasing distance to the pointing center (Bridle & Schwab 1999). We binned the data, calculated the median S_P/S_T , and used the expected functional dependence of the flux ratio and distance to the pointing center in the presence of bandwidth smearing (as explained in detail in Bridle & Schwab 1999) to account for bandwidth smearing of the peak fluxes. We used this relation to correct the peak flux for each source, and we verified that the S_P/S_T ratio does not depend on distance to the pointing

center after the correction. The final total fluxes are consistent with the shallower [Smolčić et al. \(2014\)](#) 324 MHz Catalog (Fig. 2.6).

In the left panel of Fig. (2.5), we show the peak-over-total flux ratio, S_P/S_T , as a function of the S/N of sources extracted from the 610 MHz mosaic, combined from 19 pointings. We corrected for bandwidth smearing in the 610 MHz mosaic by dividing the peak flux of each source with the median value of the peak-over-total flux distribution.

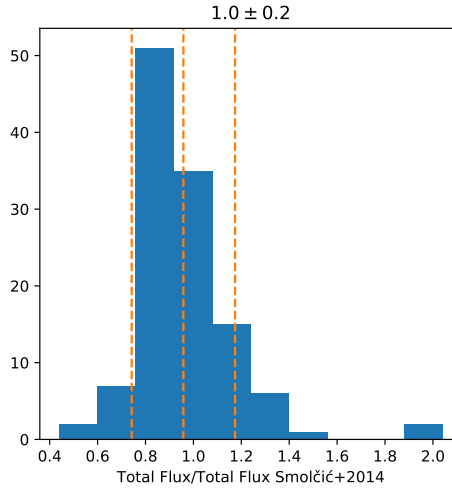


Figure 2.6: The panel shows the ratio of total fluxes detected in the 325 MHz map and in the [Smolčić et al. \(2014\)](#) map. The mean and the 1σ interval of the ratio are shown as vertical orange lines.

2.2.4 Resolved and unresolved sources

In radio maps, ideal unresolved sources with infinitely high S/Ns have peak fluxes in Jy/beam equal to their total fluxes because their flux is contained within the area that is covered by the beam. However, because of the noise properties of the map, we expect the S_T/S_P ratio for unresolved sources to increasingly scatter around unity with decreasing S/N. We thus discerned resolved sources in the 325 MHz map and the 610 MHz mosaic through the following procedure. We first fit the fifth percentile in the total-over-peak ratios that are lower than 1 as a function of the S/N, as the total flux can only be lower than 1 as a result of statistical effects. We did

this by fitting all detections with a total flux lower than the peak flux with a relation of the form $S_T/S_P = 1 - a(S/N)^b$, as is commonly used in the literature (see, e.g., [Smolčić et al. 2017b](#); [Bondi et al. 2003](#)). Second, we assumed that the noise is symmetric around unity. We therefore mirrored this envelope around $S_T/S_P = 1$ and considered all sources above it resolved.

The best-fit parameters are $a = 3.58$ and $b = -1.13$ and $a = 1.26$ and $b = -0.76$ for the 325 MHz and 610 MHz catalogs, respectively. Therefore, we consider 177 (196) sources with $S_T/S_P > 1 + 3.58(S/N)^{-1.13}$ ($S_T/S_P > 1 + 1.26(S/N)^{-0.76}$) to be resolved at 325 MHz (610 MHz), as shown in the right panel of Fig. (2.4) (Fig. 2.5). We set their total fluxes of unresolved sources to the values of their respective peak fluxes. We note that the fraction of resolved sources (see Table 2.1) is higher in the 610 MHz catalog because the 610 MHz map is 1.3 – 1.8 times more sensitive than the 325 MHz map (derived by assuming spectral indices in the range from 1 to 0.5).

2.2.5 Multicomponent sources and deblending

If the resolution of the map is good enough, source extraction algorithms start to separate jets, lobes, and star-forming regions of radio sources into separate sources. We therefore need to associate these components with a single source, termed multicomponent. To quantify this effect in our GMRT maps and find multicomponent sources, we made use of the 3 GHz source catalog. This catalog was used because it reaches a much higher depth (it is 4 – 13 times more sensitive than the 325 MHz map and 3 – 7 times more sensitive than the 610 MHz map for spectral indices of 1-0.5) and a higher resolution (0.75 arcsec at 3 GHz vs ~ 10 arcsec at 325 MHz and ~ 5.6 arcsec at 610 MHz). If the source has multiple components, that is, components that are not connected by detectable emission, in this higher resolution 3 GHz map (see [Smolčić et al. 2017b](#), for details), it is a good candidate for a multicomponent source in the map of lower resolution. Conversely, we do not expect single-component sources at 3 GHz to appear as multicomponent at lower resolution.

By visually inspecting cutouts of the maps extracted at positions of multicomponent sources in the 3 GHz source catalog, we found components that needed to be combined into one multicomponent source. The method used to detect multicomponent sources was independently

verified using the algorithm described in detail in [Vardoulaki et al. \(2019\)](#). This algorithm generated 3 GHz cutouts that were convolved to a 10 arcsec resolution, and we then used them to create masks for the component-finding algorithm. The algorithm searches for positions within the mask and within a radius that is defined by the linear projected size of the source (linear projected sizes are measured by a semi-automatic machine-learning technique and have been verified by eye, [Vardoulaki et al. 2019](#)). To be consistent with [Smolčić et al. \(2017b\)](#), the total flux was measured after the multicomponent source was identified using the AIPS task TVSTAT after clipping all the pixels below 2σ . This is consistent with the method used for all other radio source catalogs in the COSMOS field ([Schinnerer et al. 2007, 2010](#); [Smolčić et al. 2014, 2017b](#)). In the 325 MHz map, we find only 2 components that needed to be combined into 1 multicomponent source, and in the 610 MHz mosaic we find 25 components that needed to be combined into 12 multicomponent sources. As our analysis is based on the 3 GHz source catalog, in the final catalog, we set the position of the multicomponent source in the GMRT catalogs to its respective position in the 3 GHz catalog, its peak flux to -99, and we replaced its total flux by the value derived above and set the multicomponent flag to 1.

We further identified two sources that were blended into one source at 325 MHz. This number of blended sources was expected, based on the analysis of the 3 GHz source catalog (right panel of Fig. 2.4). We deblend the identified blended source in the 325 MHz map by using BLOBCAT to be consistent with other flux estimates of the catalog. To ensure that BLOBCAT separated the blended source into two sources, we set the fS/N parameter to 5.78. We tested these measured fluxes using the CASA task IMFIT with visually identified masks that separated the two sources. The sum of total fluxes of the two sources derived using BLOBCAT equals the total flux of the blended source. In the final catalog, we replaced the blended source with two entries in the catalog and the BLOBCAT -derived properties of the respective sources.

To summarize, we associated two source components with one source and deblended one source into two separate sources in the 325 MHz catalog. We also associated 25 source components with 12 multicomponent sources in the 610 MHz catalog. The total number of sources in the GMRT catalogs of the COSMOS field is therefore 633 and 986, respectively.

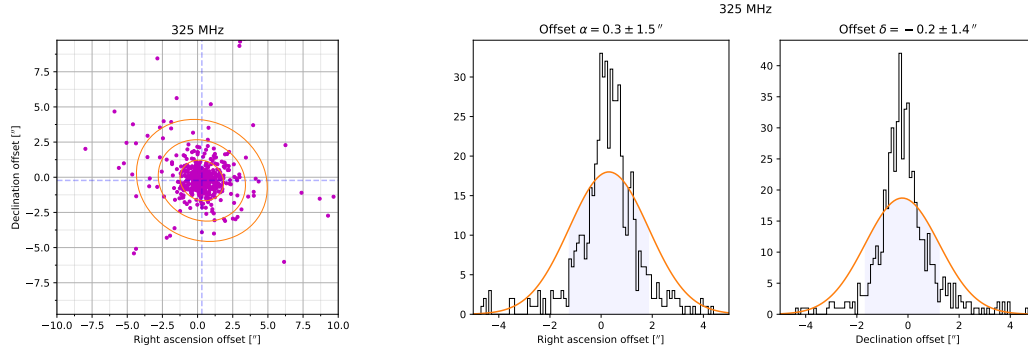


Figure 2.7: The panels show the astrometric offsets of the 325 MHz pointing positions to the 3 GHz catalog. The left panel shows the two-dimensional distribution of offsets. Dashed blue lines indicate the median offset in right ascension and declination, while the blue shaded region shows the 1, 2, and 3 σ covariance ellipses. The middle and right panels show their respective right ascension and declination offset histograms with fitted Gaussians.

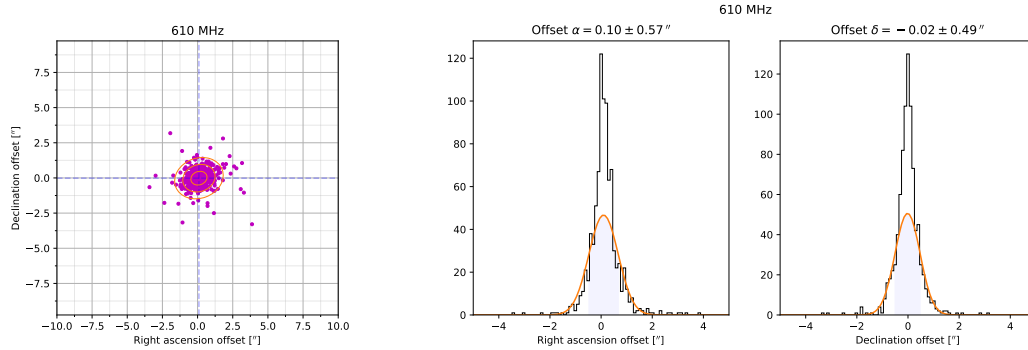


Figure 2.8: The panels show the astrometric offsets of the 610 MHz mosaic positions to the 3 GHz catalog. The left panel shows two-dimensional distribution of offsets. Dashed blue lines indicate the median offset in right ascension and declination, and the blue shaded region shows the 1, 2, and 3 σ covariance ellipses. The middle and right panels show their respective right ascension and declination offset histograms with fitted Gaussians.

2.2.6 False-detection rate

As noise in radio-interferometric images is non-Gaussian and source detection is based on a 5σ -base peak detection, we statistically expect that a small percentage of detections might be random noise fluctuations. To assess the false-detection rate, we assumed that the background noise is symmetric around zero and ran BLOBCAT on the inverted maps (i.e., map multiplied by -1), with the same input parameters as in the original maps. Given that sources with negative fluxes are not expected in the radio map, any source extracted from the inverted map can be reliably identified as a false detection. We find 19 “detections” in the inverted 325 MHz map, yielding a false-detection rate of 3% and 13 “detections” in the inverted 610 MHz map, yielding a false-detection rate of 1.3%.

2.2.7 Astrometry

To test the astrometric accuracy of the data, we show in the Figs. (2.7) and (2.8) the offsets of the source positions in the 325 MHz and 610 MHz catalogs, respectively, from those present in the 3 GHz catalog. The mean offsets in right ascension are within one tenth of the beam size of the GMRT maps, which means that the astrometric accuracy is good.

2.2.8 Final catalogs

In the final catalog we report the positions of sources as well as their peak (in Jy/beam), and total fluxes (in Jy). For the multicomponent sources, the total flux of both components is indicated in one catalog entry. The ‘Multicomponent’ column indicates the presence of more than one component to the source. For resolved sources, the column ‘Resolved’ is set to 1.

2.3 Source counts and flux errors of the GMRT catalogs

After publication of the [Tisanić et al. \(2019\)](#) paper, during a conversation with the co-authors, it transpired that GMRT fluxes of objects from the 610 MHz catalog of the COSMOS field might be lower than expected. Here we describe various tests performed on the GMRT 610 MHz mosaic and the construction of source counts, which were used as a basis for enlarging the errors in the published version of the GMRT 610 MHz catalog.

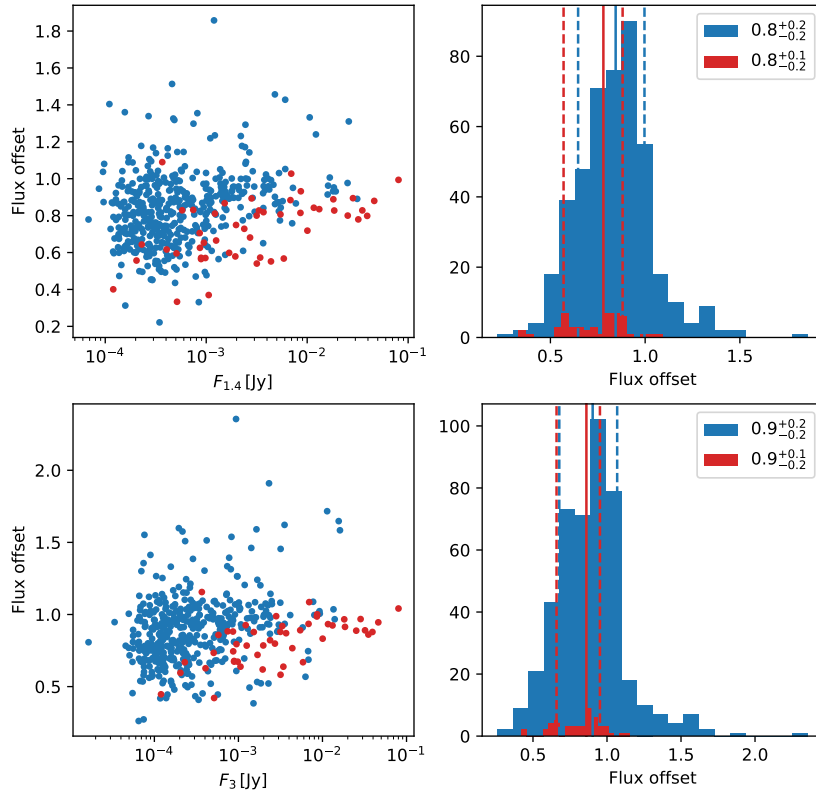


Figure 2.9: Ratio of expected flux at 610 MHz computed by assuming the spectral index between 325 MHz and 1.4 GHz, and the flux from the 610 MHz catalog. Bottom row shows the offset computed using the flux estimate based on the spectral index between 325 MHz and 3 GHz and red points show multicomponent sources.

In the top row of Fig. 2.9 we show the ratio of the expected flux at 610 MHz by assuming the spectral index $\alpha_{325-1.4}$ and the flux from the 610 MHz catalog (the bottom row shows the offset computed using the flux estimate based on α_{325-3} and red points show multicomponent sources). The 610 MHz fluxes are on average 20% lower than expected (a correction factor of 1.3 ± 0.3). There is no apparent trend with either the 1.4 GHz or 3 GHz flux or the number of pointings that overlap at the position of a source, as shown in the top panel of Fig. 2.10. However, this offset depends on right ascension and declination, as shown in the bottom left panel of Fig. 2.10. The greatest offset would correspond to a region between pointings 01, 02, 03, 05 and 08. There seem to be no significant differences in the local RMS values in that region, as shown in the bottom right panel of Fig. 2.10.

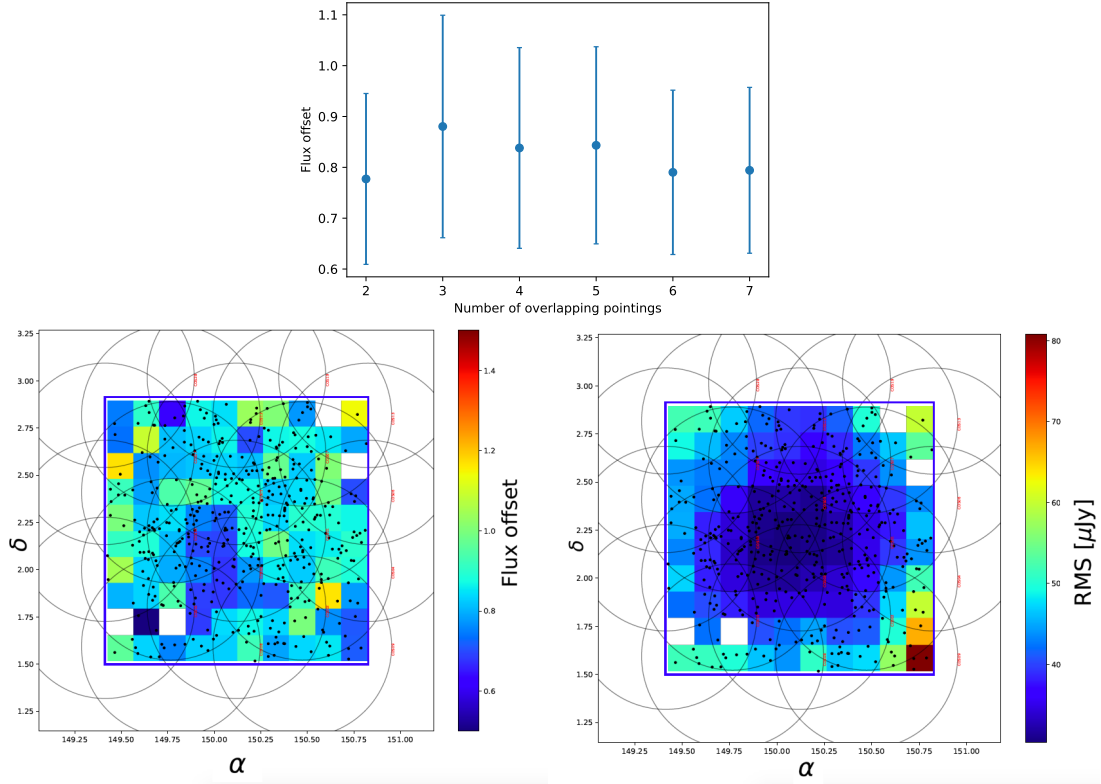


Figure 2.10: Positional offsets in the GMRT 610 MHz map. Top panel shows the flux offset as a function the number of pointings that overlap at the position of a source. Bottom left panel shows how the offset depends on right ascension and declination, while the bottom right panel shows the variations in the local RMS values within the GMRT 610 MHz mosaic.

Euclidean normalized source counts, shown in Fig. 2.11 were computed for the GMRT 610 MHz catalog and compared to the [Smolčić et al. \(2017b\)](#), scaled using an 0.7 spectral index, [Smolčić et al. \(2018\)](#), [Garn et al. \(2008\)](#), [Ibar et al. \(2008\)](#), and [Whittam et al. \(2017\)](#) source counts. The lower section of the plot shows source count ratios, limited to the flux density range from 10 mJy to 100 mJy. The flux density range was chosen to exclude lower flux densities, at which the [Smolčić et al. \(2017b\)](#) source counts are not reliable and we do not expect significant variation due to cosmic variance ([Heywood et al. 2013](#)).

A further attempt was made to compute source counts while excluding pointings COS02 and COS03 from the mosaic, which yielded no significant change in the computed spectral indices. Another approach was to compute the spectral index, $\alpha(610 \text{ MHz}, 3 \text{ GHz})$ and use it to scale the VLA-COSMOS source counts. To this end, the median RMS of the GMRT-COSMOS map was used to compute the median Kaplan-Meier estimates for different flux bins, for sources is the VLA-COSMOS counterpart catalog, as shown in the upper panels of Fig. 2.12. The mean Kaplan-Meier estimate was problematic due to significant dispersion in α , but the median Kaplan-Meier estimate converged as expected. We computed the spectral index using both a constant ($\alpha = 0.32 \pm 0.07$) and linear model ($\alpha = 0.389 \pm 0.002 \log(F_{3000} / \text{mJy}) + 0.3738 \pm 0.0005$) fits of the $\alpha - F$ relationship. By using just the bins within the dashed lines, it was found that the spectral index was rising with rising flux. This $\alpha - F$ relationship to recompute VLA-COSMOS source counts at 610 MHz. The source count ratios are now very similar to unity when using the linear model, as shown in the lower right panel of Fig. 2.12. In this figure, we also show the source counts based on the [Wilman et al. \(2008a\)](#) simulation, which also shows source count ratio differences when compared to [Smolčić et al. \(2017b, 2018\)](#).

Due to significant variation between the different literature source counts, a definitive conclusion regarding our flux densities cannot be made based on source counts. The conclusions of these analyses are:

1. For sources detected at both GMRT and VLA frequencies, there seems to be a deficit in flux computed at 610 MHz based on the VLA fluxes. This correction is appropriate for some of the sources, while blindly applying a 20% correction of the total flux induces overcorrection in others, as indicated by a large spread in the flux deficit histograms, which

persists even if using only high-SNR sources.

2. The flux offset is different when computed based on the 1.4 GHz catalog and when computed using the 3 GHz catalog, indicating complications due to complex spectral shapes.
3. There is discrepancy between source counts around 600 MHz for various fields, with source count ratios varying up to ~ 20 between surveys below 10 mJy.
4. By looking at source counts the effect might be flux-dependent, but this analysis cannot be easily extended to all of the sources in the catalog since it can be reliably computed only between 1 mJy and 10 mJy, a flux range limited by cosmic variance at large-flux end and completeness effects at the low-flux end.
5. The flux offset effect might be positionally dependent, but simple exclusion of pointings did not yield a specific pointing which produces these offsets. This would indicate that a simple correction of the total flux would be a significant overcorrection if the correction is needed only for one part of the map.

While increasing fluxes for a small sample of individual sources is not without precedent (Kolokythas et al. 2015), considering points 1-5, we advise caution in applying a similar correction to the whole catalog and instead model the errors of the total flux by having an independent 20% additional error contribution.

The points 1-5 and the preceding passage have been included in the final published GMRT 610 MHz catalog, now publicly available on IRSA¹.

¹<https://irsa.ipac.caltech.edu/cgi-bin/Gator/nph-scan?projshort=COSMOS>.

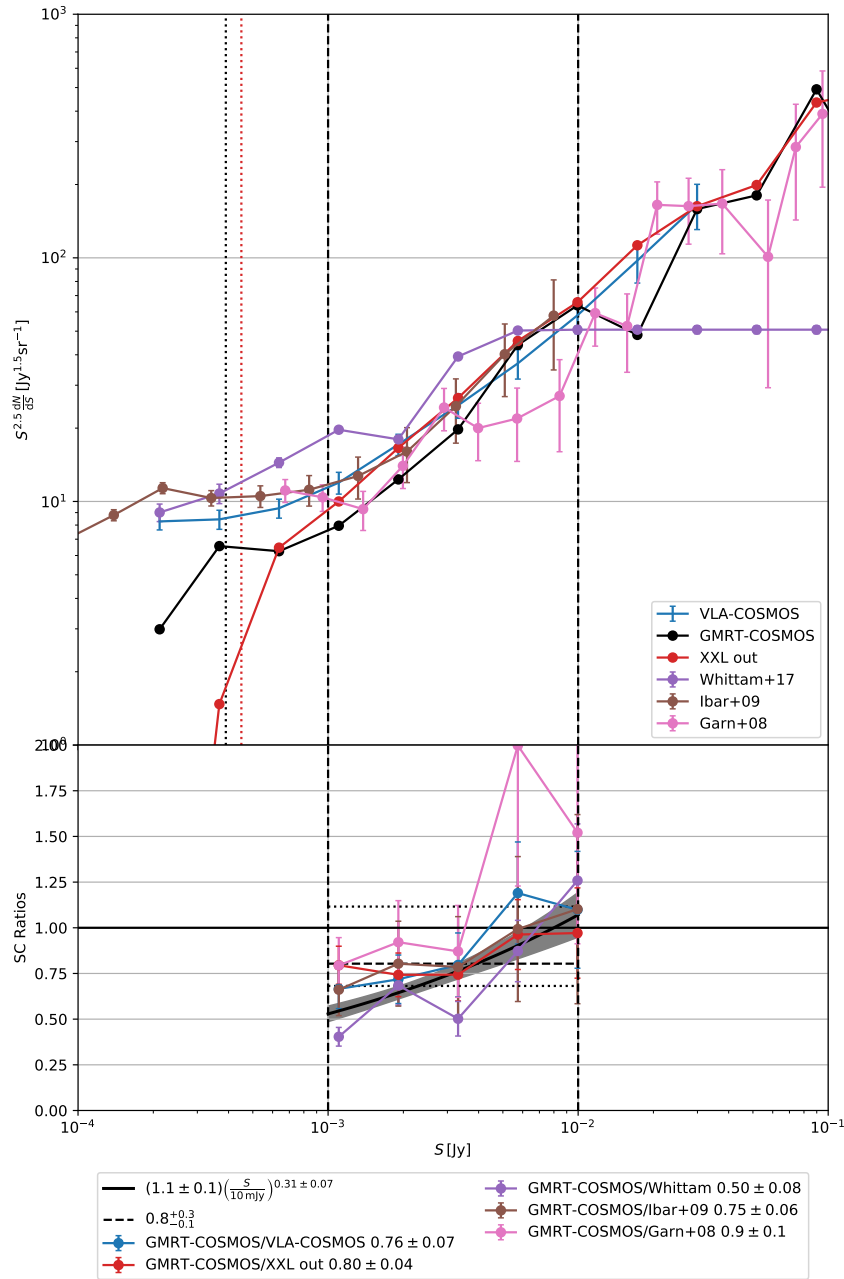


Figure 2.11: Euclidean normalized source counts for the GMRT 610 MHz catalog (solid black line), VLA-COSMOS 3 GHz source counts (Smolčić et al. 2017b), scaled using an 0.7 spectral index, XXL 610 MHz source counts (labeled as XXL-out and shown with a solid red line Smolčić et al. 2018). Garn et al. (2008) source counts are shown in pink, Ibar et al. (2008) source counts in brown, and Whittam et al. (2017) source counts in purple. The lower section of the plot shows source count ratios, limited to the flux density range from 10 mJy to 100 mJy.

2.3. Source counts and flux errors of the GMRT catalogs

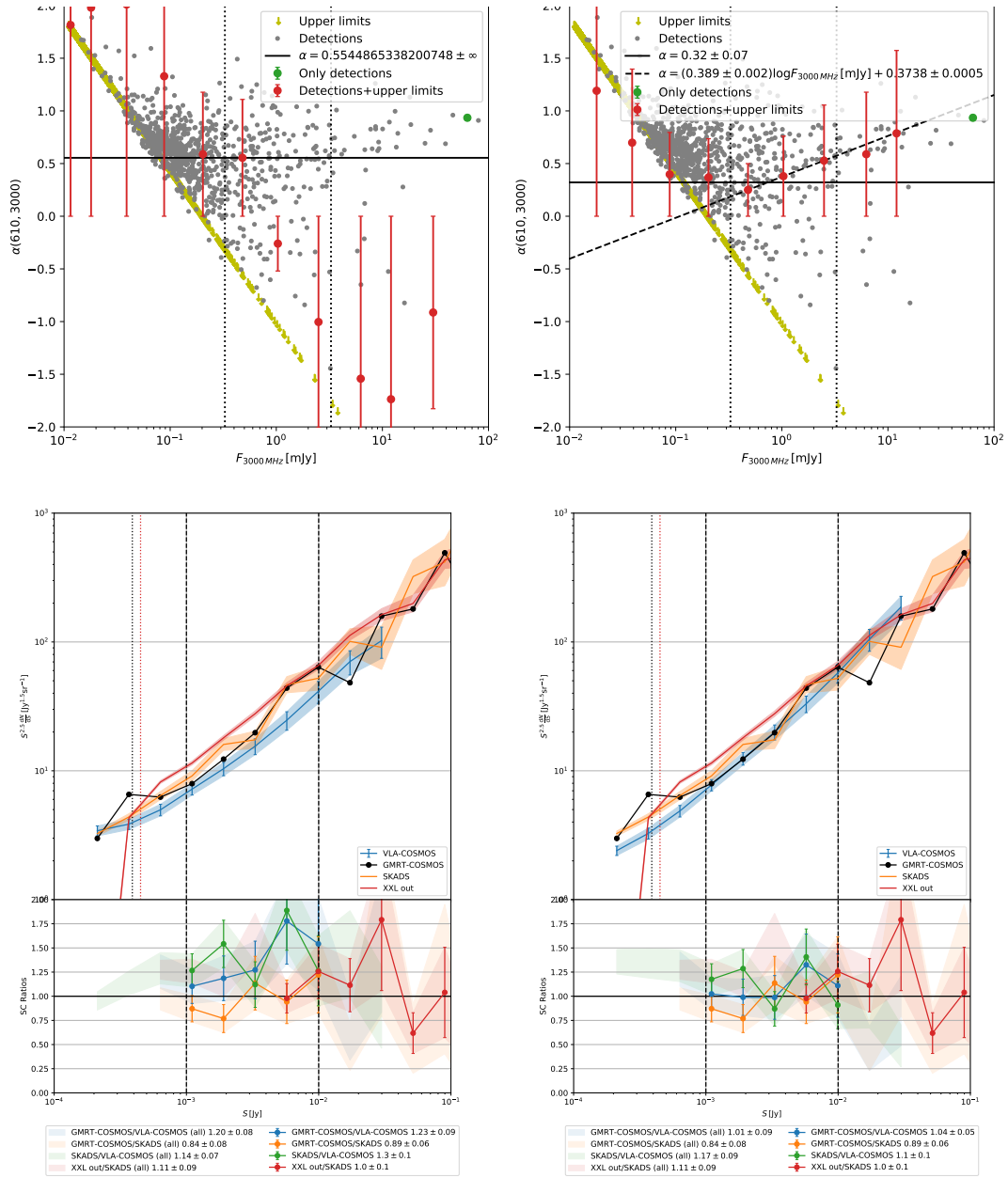


Figure 2.12: Upper panels show the mean (left) and median (right) spectral indices $\alpha(610, 3000)$, estimated using survival analysis (red points) for various 3 GHz flux density bins. These spectral indices were fitted with a constant (solid horizontal line) and a linear model (dashed line). In the lower panels, the Euclidean normalized source counts for the GMRT 610 MHz catalog resulting from the constant spectral index model (left panel) and a linear spectral index model (right panel) are shown. Source count ratios are shown in the lower parts of the panels, with their estimated 16-84 percentile interval shown as shaded regions.

Chapter 3

Construction and models of the average radio SED

In this chapter, we describe the method used to construct the radio SED and the models used to analyze it.

The methods used in this chapter were designed for 1.4 GHz-selected samples of highly star-forming galaxies (HSFGs), having $\text{SFR} > 100 \text{ M}_{\odot}/\text{yr}$, and radio-excess AGN (RxAGN), AGN identified by their 3σ radio excess with respect to the value of radio luminosity expected only from star formation. Details about construction of these samples and resulting SEDs can be found in chapter 4, for HSFGs, and chapter 5, for RxAGN.

In Sect. 3.1 we describe how we constructed the radio SED for samples of galaxies from the GMRT and VLA observations of the COSMOS field while accounting for lower sensitivities of the GMRT maps using survival analysis. In Sects. 3.2 and 3.3 we describe the models of the radio SED and the Monte Carlo simulations that test the applicability of the fitting procedure, respectively.

3.1 Construction of the average radio SED

To construct a typical SED for a sample of galaxies in the COSMOS field, we normalized the spectra of individual galaxies at a particular rest-frame frequency. Considering that the redshifts

of sources in our samples vary from 0.3 to 4, we obtain a well-constrained SED from rest-frame frequencies of ~ 0.5 GHz to ~ 15 GHz.

A complication to this basic idea is that there are very few detections in the 325 and 610 MHz maps. For this reason, we normalized the flux densities at all frequencies based on a linear fit to the 1.4 and 3 GHz spectra. We chose the normalization rest-frame frequency to be the median log-frequency of sources in the selected sample at 1.4 GHz and 3 GHz. For example, for the HSFG sample, this frequency is 5.7 GHz. We constrained the 325 and 610 MHz flux densities of non-detections by five times the local RMS flux density of their respective maps. The problem is therefore to constrain the spectral index when a significant portion of the data is left-censored, meaning that many of the data points below a rest-frame frequency of 1 GHz, corresponding to observer frame 325 and 610 MHz frequencies, are upper limits. To correctly deal with upper limits, we decided to employ the survival analysis technique described in the following paragraph and illustrated in Fig. (3.1).

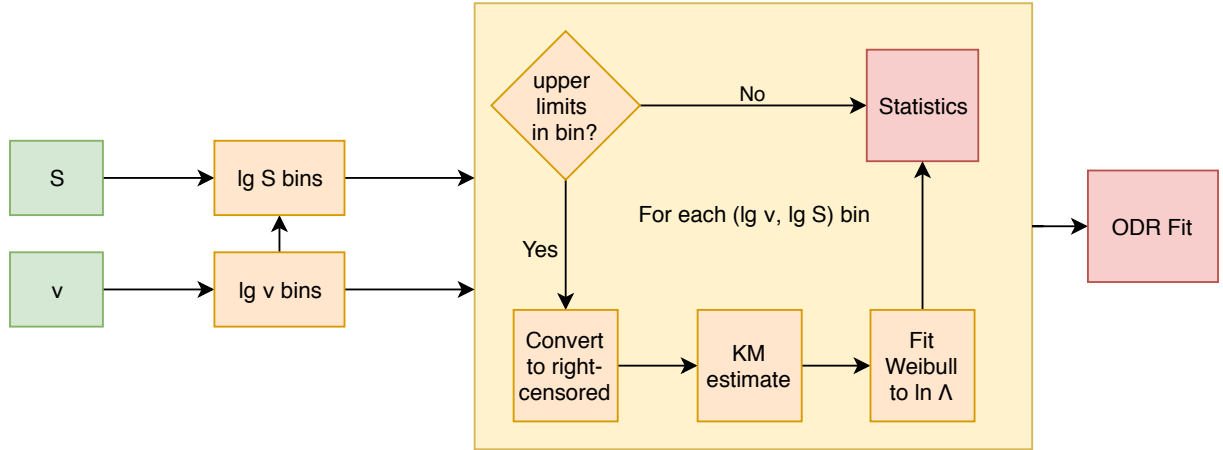


Figure 3.1: Flowchart of the radio SED fitting procedure described in Sect. 3.1. The input values are source fluxes, S , and rest-frame frequencies, ν . The log fluxes are then binned in log-rest-frame frequency bins. If there are no upper limits in a certain bin, the mean and standard deviation are calculated immediately, and if that is not the case, the log fluxes are converted into a right-censored dataset, and the Kaplan-Meier estimate is calculated. This estimate is then fit to a Weibull distribution, yielding the analytically determined means and standard deviations. The resulting different bins are then treated as data points with errors in both axes and are fit by a particular model by employing the orthogonal distance regression (ODR) method.

We combined into a single dataset the normalized fluxes and normalized upper limits of individual galaxies at different rest-frame frequencies. As we have four different observer-frame frequencies, the number of our data points is four times larger than the number of galaxies. To achieve uniform frequency binning, we used 20 bins that were equally separated in log space of the rest-frame frequencies. The number of bins was chosen empirically to achieve a satisfactory number of bins while retaining a sufficient number of data points within each bin for the statistical analysis.

For each bin, i , if there were no upper limits within the bin, we computed the mean of the log rest-frame frequency, $\nu_i = 10^{\langle \log \nu_r \rangle_i}$, and its standard deviation, $\sigma_{\log \nu_i}$, along with the mean normalized log flux, $\langle \log F_\nu \rangle_i$, and its standard deviation, $\sigma_{\log F_i}$. If there were upper limits within a particular bin, we constructed the Kaplan-Meier estimate of the survival function of fluxes within the bin using the *lifelines* package¹. We did this by converting this left-censored dataset into a right-censored one in accordance with Feigelson & Nelson (1985) as the *lifelines* package handles right-censored datasets.

We then fit the survival function with the Weibull distribution (Lai et al. 2006). We have found this method to be satisfactory because the Weibull distribution survival function, $S(x|\lambda, k) = e^{-(x/\lambda)^k}$, where λ and k are free parameters of the model, can be easily linearized. We estimated $\langle \log F_\nu \rangle$ from k and λ and calculated $\sigma_{\log F}$ as the standard deviation of the Weibull distribution.

Survival analysis assumes that upper limits have the same underlying distribution as the data, and the Kaplan-Meier estimator further assumes that detections and upper limits are mutually independent (Kaplan & Meier 1958). The latter condition is satisfied by normalizing spectra to one frequency, as the normalization redistributes both the data and the upper limits based on the source’s normalization flux. Further tests of this procedure are described in Sect. 3.3 using Monte Carlo simulations.

¹See <https://lifelines.readthedocs.io/>.

3.2 SED fitting

Previous studies, have shown that the shape of the radio SED deviates from a simple power law.

In both the HSFG and RxAGN samples, we observe that the SED flattens below 3 – 4 GHz (see Sect. 4.3 of chapter 4 and figures therein). To account for this, we assumed a broken power-law SED

$$\log F \begin{pmatrix} \alpha_1 \\ \alpha_2 \\ b \\ \nu_b \end{pmatrix} = \begin{cases} -\alpha_2 \log \frac{\nu_r}{\nu_n} + b, & \nu_r > \nu_b, \\ -\alpha_1 \log \frac{\nu_r}{\nu_n} + b + (\alpha_1 - \alpha_2) \log \frac{\nu_b}{\nu_n}, & \nu_r < \nu_b, \end{cases}. \quad (3.1)$$

where ν_n is the normalization frequency, ν_b the break frequency, α_1 (α_2) the spectral index below (above) ν_b , and b the normalization constant.

When fitting more complex models, some parameters might not be constrained by simple fitting strategies. In such cases, we employ the Markov chain Monte Carlo (MCMC) method (implemented using the affine invariant sampler of the *emcee* package [Foreman-Mackey et al. 2013](#)) to first find a 2σ confidence interval for each parameter, which we then use as bounds for the final fit. The MCMC code samples the log-likelihood distribution of parameters, $\theta = (\alpha_1, \alpha_2, b, \nu_b)$,

$$\ln \mathcal{L}(\theta) \propto -\frac{1}{2} \sum_i \left(\frac{\langle \log F \rangle_i - \log F(\nu_i, \theta)}{\sigma_{\log F_i}} \right)^2, \quad (3.2)$$

where the values $\langle \log F \rangle_i$ and $\sigma_{\log F_i}$ and ν_i are log-flux derived by using survival analysis in each log-frequency bin with the main value of log frequency in each bin being x_i . For the sake of simplicity of implementation, we considered only the errors in normalized log flux in the denominator of Eq. (3.2) when using the MCMC method.

The final fitting of the broken power-law model is performed using the orthogonal distance regression method (hereafter, ODR), which accounts for the errors on both axes. The 1σ confidence interval, $\sigma(\nu_r)$, is computed as $\sigma(\nu_r|\theta) = \sqrt{(\nabla_{\theta} \log F)^T \Sigma_{\theta} \nabla_{\theta} \log F}$, with Σ_{θ} being the covariance matrix of the fit parameters derived using the ODR method and θ being the vector of free parameters of the broken power-law.

3.3 Method verification through simulations

Our average SEDs were derived using survival analysis, where the percentage of upper limits below rest-frame 1 GHz is high. We tested the applicability of the survival analysis by deriving the radio spectral indices for a mock sample of galaxies. The mock samples were generated with preset spectral indices by simulating different properties of the HSFG sample and of the SED shape.

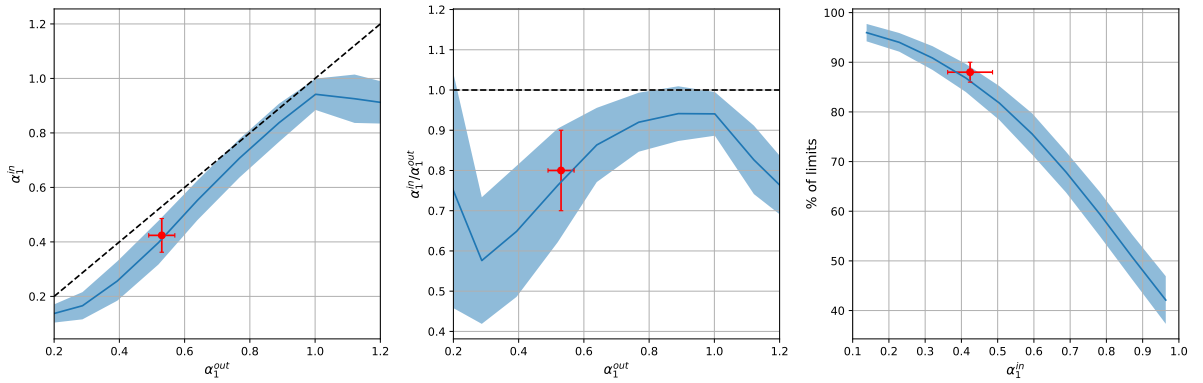


Figure 3.2: Results of simulations produced by varying the mean value of the input spectral index α_1 (labeled as α_1^{in}). The figure shows the interdependence of the following properties: the input spectral index α_1^{in} , the derived spectral index α_1^{out} , and the percentage of upper limits below 1 GHz. The left panel shows the dependence of the input spectral index, α_1^{in} , on α_1^{out} ; the middle panel shows the dependence of the $\alpha_1^{in}/\alpha_1^{out}$ ratio on the output spectral index, α_1^{out} ; and the right panel shows the dependence of the percentage of upper limits below 1 GHz on α_1^{in} . The solid lines show the means derived for different bins in the x-axes of their respective plot, while the colored intervals show the 1σ interval for the same bins. The red point shows the values of spectral index α_1 before and after correction, and the percentage of upper limits below 1 GHz, as presented in Sect. 4.3. The dashed lines are the equality lines.

We constructed the mock sample based on the distribution of individual galaxy redshifts, z , a spectral index between 1.4 and 3 GHz, α_2 , and the log-flux normalization, b , in the real HSFG sample. We have chosen to vary the mean value of the low-frequency spectral index, α_1 , to achieve different degrees of flattening in the simulations while keeping the number of galaxies

in the simulation equal to the number of galaxies in the real sample. In order to simulate the flattening of the spectral index below the break frequency, ν_b , we assumed a broken power-law with a spectral index of α_1 below ν_b , with the following assumptions: 1) α_1 has the same variance as α_2 and 2) α_1 is uncorrelated with α_2 , z , and b . Before creating the full mock catalog, we removed the sources in the mock 325 MHz and 610 MHz catalogs with fluxes below 5σ , where σ is the median RMS of the respective 325 MHz and 610 MHz COSMOS maps to simulate non-detections.

Overall, by analyzing the input (α_1^{in}) and output (α_1^{out}) spectral index, we find that it is necessary to correct the derived spectral index by 20% (downward) for $\alpha_1^{out} \sim 0.5$ and incrementally smaller correction for higher α_1^{out} . The simulation suggests that the reason for this is the large number of upper limits occurring for lower spectral indices (i.e., flatter input slopes). The left panel of Fig. (3.2) shows the dependence of the input spectral index of simulations, α_1^{in} , on the output spectral index of simulations, α_1^{out} , while the middle panel shows the dependence of the $\alpha_1^{in}/\alpha_1^{out}$ ratio on α_1^{out} . Additionally, we show the behavior of the fraction of limits below 1 GHz as a function of α_1^{in} in the right panel of Fig. (3.2). For $\alpha_1^{out} > 1$, this correction again rises to 20%. Considering the results presented in the next section, this multiplicative correction is 0.8 ± 0.1 for the real dataset, as indicated by the red points in Fig. (3.2). Turning the argument around, under the assumption that α_1 is normally distributed, the percentage of upper limits below 1 GHz (88%), observed in the real data, indicates $\alpha_1 \sim 0.4$.

Chapter 4

Average radio SED of highly star-forming galaxies

The analysis and results of this chapter have been published in [Tisanić et al. \(2019\)](#).

Star formation rate (SFR) measurements derived from the ultraviolet and optical emission are sensitive to dust ([Kennicutt 1998a](#)), and infrared-derived SFRs are easy to understand only in the optically thick case ([Kennicutt 1998a](#); [Condon 1992](#)). On the other hand, radio emission in star-forming galaxies (SFGs) below ~ 30 GHz is unbiased by dust ([Condon 1992](#)). Furthermore, it has been found that the infrared and radio luminosities are bound by a tight correlation over many orders of magnitude ([van der Kruit 1971](#); [Helou et al. 1985](#); [Condon 1992](#)). This infrared-radio correlation provides the basis for radio luminosity as a star-formation tracer, as infrared luminosity is linked to the SFR ([Kennicutt 1998b](#)). It is defined by the so-called q parameter, defined as $q = \log L_{\text{TIR}}/3.75 \text{ THz} - \log(L_{1.4 \text{ GHz}})$, where L_{TIR} is the total infrared luminosity ($8 - 1000 \mu\text{m}$) in units of W and $L_{1.4 \text{ GHz}}$ is the luminosity density at 1.4 GHz in units of W/Hz. A frequency of 3.75 THz is used to obtain a dimensionless quantity. In the calorimeter model ([Voelk 1989](#)), q is expected to be constant over a wide range of magnetic field strengths through electrons that lose their energy because of synchrotron and inverse Compton losses. This produces a tight correlation, even though individual galaxies may show deviations. Theoretical considerations ([Murphy 2009](#)) predict q to increase with redshift, mostly because of the synchrotron electrons' inverse Compton scattering off cosmic microwave background

photons. Recent stacking and survival analysis studies find q to be decreasing with increasing redshift (Ivison et al. 2010; Magnelli et al. 2015; Delhaize et al. 2017; Calistro Rivera et al. 2017). Delhaize et al. (2017) pointed out that the computation of rest-frame radio luminosity via a K-correction using only a simple, single power-law assumption of the star-forming galaxies' spectral energy distribution (SED) might cause such a trend.

The exact shape of the radio SED of star-forming galaxies is usually assumed to be a superposition of the steep synchrotron spectrum, described by a power law, and a $\sim 10\%$ contribution at 1.4 GHz of a flat free-free spectrum (Condon 1992). These results are supported by observations of nearby galaxies at $3 - 30$ Mpc ($z \approx 0.01$) with an $\text{SFR} < 10 M_{\odot}/\text{yr}$ (Tabatabaei et al. 2017).

For (ultra)luminous infrared galaxies ((U)LIRGs, $\text{SFR} > 10 M_{\odot}/\text{yr}$), observations in the local Universe find their radio SEDs to be steep around 10 GHz, corresponding to a spectrum that shows less flattening above 10 GHz than in galaxies with an $\text{SFR} < 10 M_{\odot}/\text{yr}$ (Clemens et al. 2008; Leroy et al. 2011; Galvin et al. 2018). Both free-free self-absorption and modifications to the spectrum due to the aging of the electron population would also be present. These processes result in deviations from a simple power-law at low ($\nu_{\text{rest}} \lesssim 1$ GHz) and high ($\nu_{\text{rest}} \gtrsim$ a few GHz) frequencies that are observationally hard to constrain.

In this chapter, we constrain the shape of the average radio spectral energy distribution (SED) of a 1.4 GHz-selected sample ($\text{SFR} > 100 M_{\odot}/\text{yr}$) of highly star-forming galaxies (HSFGs) in the $\sim 0.4 - 10$ GHz frequency range within the COSMOS field. To obtain a broad frequency range, we use the fluxes from the 1.4 GHz Very Large Array (VLA)-COSMOS Joint Project (Schinnerer et al. 2010) and the 3 GHz VLA-COSMOS Large Project (Smolčić et al. 2017b,a) and reduce previously unpublished Giant Meterwave Radio Telescope (GMRT) observations at 325 MHz and 610 MHz. We construct the average radio SED by using survival analysis to account for the lower sensitivity of the GMRT maps.

In Sect. 4.1 we describe the galaxy sample of HSFGs. In Sect. 4.3 we report the average radio spectral indices of HSFGs, while in Sect. 4.4 we discuss the shape of the radio spectrum of SFGs and the impact on the infrared-radio correlation. In this paper we use the convention for the spectral index $F_{\nu} \sim \nu^{-\alpha}$, where F_{ν} is the flux density and α is the spectral index.

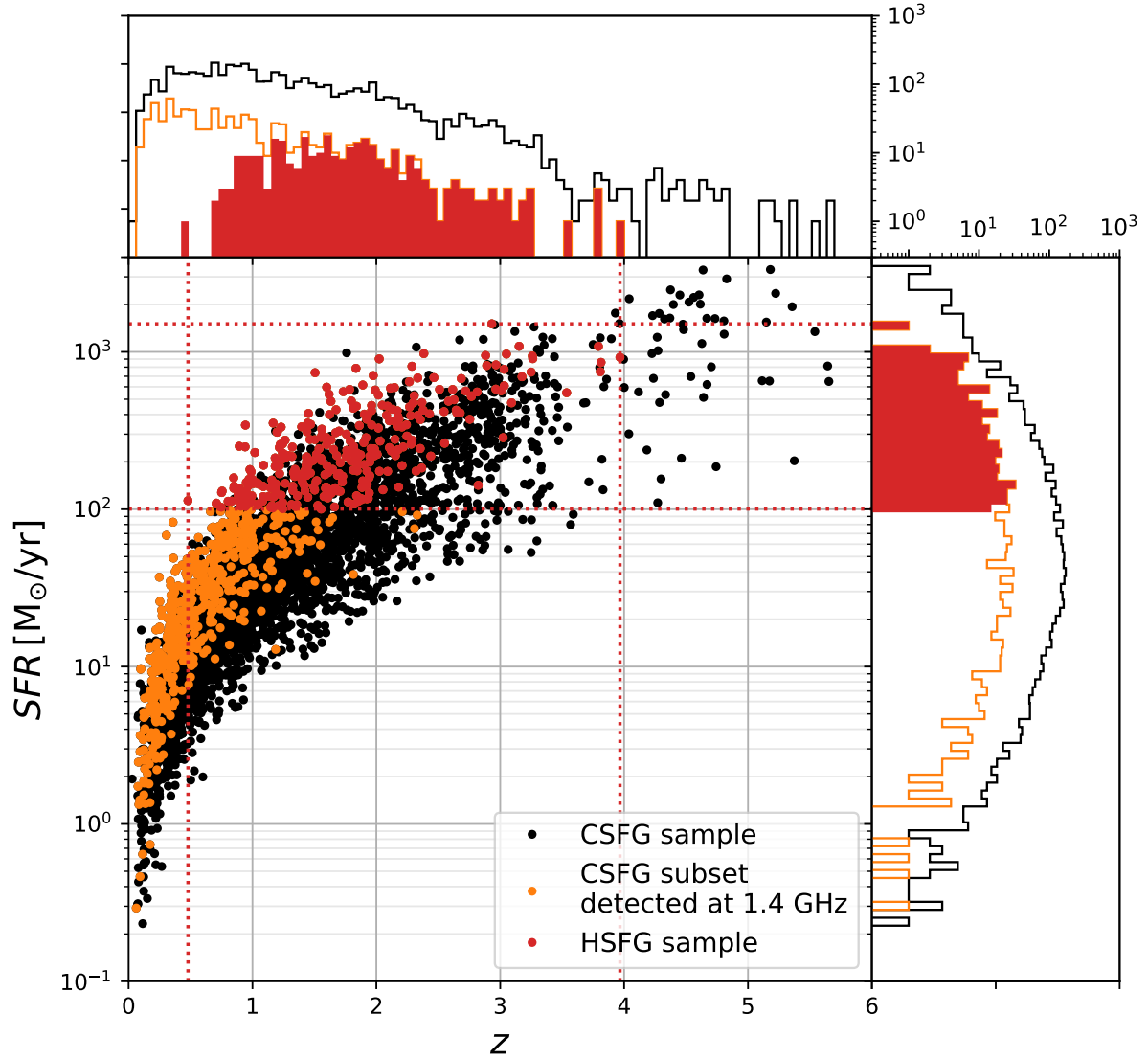


Figure 4.1: Star formation rate vs. redshift for the “clean star-forming galaxy sample” (CSFG, black points), as defined by [Smolčić et al. \(2017a\)](#), and described in Sect. 4.1. Orange points indicate a subset of the CSFG sample that was detected at both 1.4 GHz and 3 GHz. Red points indicate the HSFG sample used here, i.e., the subset of the CSFG sample with an additional cut of the infrared-derived SFR, $SFR > 100 M_{\odot}/\text{yr}$. Histograms show the redshift and SFR distributions with the different subsamples colored as in the main figure. For greater clarity, the HSFG sample is marked by filled histograms, and its limits in the main figure are denoted by dotted red lines.

4.1 Sample

To construct a complete and pure sample of star-forming galaxies over a wide range in redshift, we used the criteria described in [Smolčić et al. \(2017a\)](#), which we briefly summarize below. Starting from the VLA COSMOS Large Project 3 GHz Source Catalog, cross-correlated with multi-wavelength counterparts detected in the COSMOS field, we selected the clean star-forming galaxy sample (CSFG), as defined in [Smolčić et al. \(2017a\)](#), and imposed an additional cut of infrared-derived SFRs of $\text{SFR} > 100 \text{ M}_{\odot} \text{ yr}^{-1}$.

[Smolčić et al. \(2017a\)](#) cross-correlated the 3 GHz Source Catalog with multi-wavelength counterparts, drawn from three catalogs: i) the COSMOS2015 catalog ([Laigle et al. 2016](#)), which contains sources detected on a χ^2 sum of Y , J , H , K_s and z^{++} images, ii) the i-band catalog ([Capak et al. 2007](#)), which contains sources detected from a combination of the CFHT i^* and Subaru i^+ original point spread function (PSF) images, and iii) the IRAC catalog, which contains sources detected in the $3.6 \mu\text{m}$ band ([Sanders et al. 2007](#)). [Smolčić et al. \(2017a\)](#) combined counterparts from the three catalogs to maximize the number of counterparts as the i-band (IRAC) catalog is sensitive to potentially blue (red) sources undetected in the Y , J , H , K_s , z^{++} stack. Over the inner 1.77 deg^2 subarea of the COSMOS field, which excludes all regions affected by saturated or bright sources in the optical to near-infrared bands, and thus contains sources with the best possible photometry, [Smolčić et al. \(2017a\)](#) found 7729 COSMOS2015, 97 i-band, and 209 IRAC counterparts to the 8696 3 GHz sources within this area. The COSMOS2015 and i-band catalogs offer precise photometric redshifts, with a joint precision of $\sigma_{\Delta z/(1+z)} = 0.01$.

The CSFG sample was constructed from the full 3 GHz galaxy sample with COSMOS2015 or i-band counterparts as the cleanest sample of star-forming galaxies by excluding AGN through a combination of criteria, such as X-ray luminosity, mid-infrared (color-color and SED-based) criteria, $r^+ - \text{NUV}$ colors, and ($> 3\sigma$) excess in the distribution of the ratio of 1.4 GHz radio luminosity and IR-based SFRs as a function of redshift (see Sect. 6.4 and Fig. 10 in [Smolčić et al. 2017a](#)). To determine the physical properties of the galaxies, a three-component SED-fitting procedure ([Delvecchio et al. 2017](#)) was applied using all of the available photometry.

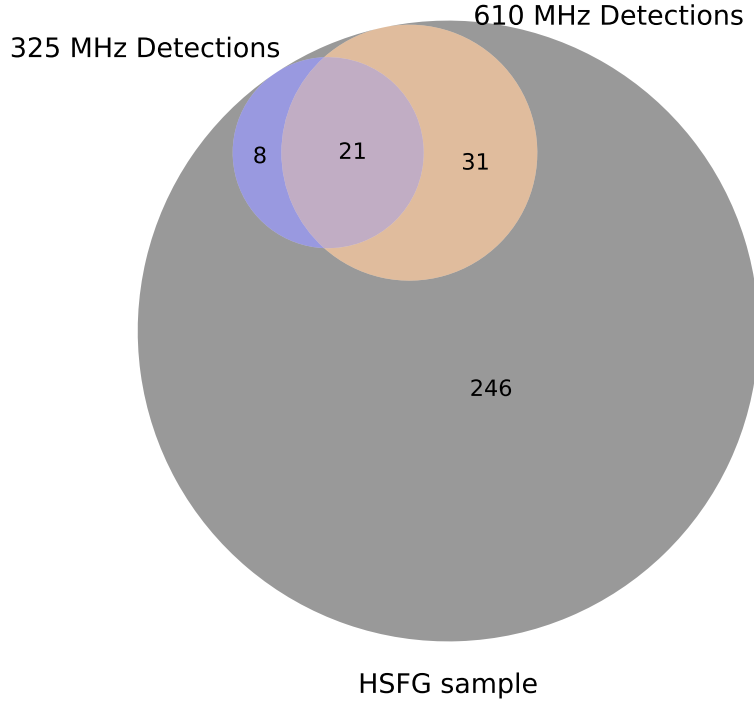


Figure 4.2: Number of detections in GMRT catalogs of sources in the HSFG samples. The gray area represents the sources that are not detected in the GMRT maps, while blue and orange areas represent sources detected at 325 MHz and 610 MHz, respectively.

The fitting procedure was based on MAGPHYS (Da Cunha et al. 2008) and SED3FIT (Berta et al. 2013) to account for the AGN component of the SED. SFRs were computed from the 8–1000 μm rest-frame infrared luminosity that was obtained by using the best-fit galaxy template and was then converted into SFR through the Kennicutt (1998a) conversion factor and scaled to a Chabrier (2003) initial mass function. Star formation rates are shown for the entire 3 GHz Large Project catalog and the subset of highly star-forming galaxies ($\text{SFR} \geq 100 \text{ M}_{\odot}/\text{yr}$) in Fig. (4.1) as a function of redshift. The figure shows that a cut above $100 \text{ M}_{\odot}/\text{yr}$ minimizes incompleteness above $z \approx 2$, which strongly influences the sample below $100 \text{ M}_{\odot}/\text{yr}$. To check

whether the remaining incompleteness could influence our results, we repeated our analysis of Sect. 4.3 for the more complete subsample of HSFGs out to $z \sim 2$. We find no significant difference in the resulting SED and therefore conclude that the $100 \text{ M}_\odot/\text{yr}$ cut sufficiently reduces incompleteness out to $z \sim 4$.

Finally, we cross-matched the 3 GHz catalog with the above described cuts and the 1.4 GHz joint catalog, to arrive at a sample of 306 galaxies that have two reliably determined fluxes in the rest-frame frequency-flux space. We call the subset of the CSFG sample that is detected at both 1.4 and 3 GHz and has $SFR > 100 \text{ M}_\odot/\text{yr}$ the highly star-forming galaxy (HSFG) sample. The 325 MHz and 610 MHz catalogs were then cross-matched with the HSFG sample catalog with a matching radius of 1 beam, leading to 29 and 52 sources in the HSFG sample, respectively. The summary of the number of detections and non-detections in the catalogs used to construct the radio SED of the HSFG sample is provided in Fig. (4.2).¹

In summary, the selected sample is effectively a 1.4 GHz data-selected HSFG ($SFR > 100 \text{ M}_\odot/\text{yr}$). With this dataset, we associated the 3 GHz data, with a much lower RMS ($\sim 12 \mu\text{Jy}/\text{beam}$ and $\sim 2 \mu\text{Jy}/\text{beam}$ at 1.4 GHz and 3 GHz, respectively), minimizing potential biases that could arise in the 1.4 to 3 GHz spectral index distribution, given that almost all 1.4 GHz sources (90%, Smolčić et al. 2017b) have counterparts at 3 GHz. In total, the HSFG sample contains 306 galaxies, out of which 9% (29) were detected at 325 MHz and 17% (52) at 610 MHz.

4.2 Methods

Previous studies have shown that the shape of the radio SED deviates from a simple power law. As the SED at higher frequencies ($\nu \gtrsim 10 \text{ GHz}$) is expected to have a contribution not only by synchrotron, but also by free-free emission, the simplest modification to a simple power-law would be adding a thermal contribution with a flat spectral index of 0.1 (Condon 1992) that

¹The table of the cross-matched fluxes is available in electronic form at the CDS via anonymous ftp to cdsarc.u-strasbg.fr (130.79.128.5) or via <http://cdsweb.u-strasbg.fr/cgi-bin/qcat?J/A+A/>.

would produce a flattening of the SED above 10 GHz:

$$F \left(\nu_r \left| \begin{array}{c} \alpha_2 \\ b \\ f \end{array} \right. \right) = 10^b \left[\left(\frac{\nu_r}{\nu_n} \right)^{-\alpha_2} (1 - f) + f \left(\frac{\nu_r}{\nu_n} \right)^{-0.1} \right], \quad (4.1)$$

where ν_r is the rest-frame frequency, and the parameters of the model are α_2 , the nonthermal spectral index, b , the normalization constant, ν_n , the normalization frequency, and $f = f(\nu_n)$, the thermal fraction at ν_n . In our HSFG sample, however, we observe that the SED flattens below 3 – 4 GHz (see Sect. 4.3 and figures therein).

The full SED model includes a broken power-law component and a thermal component

$$F \left(\nu_r \left| \begin{array}{c} \alpha_1 \\ \alpha_2 \\ b \\ f \\ \nu_b \end{array} \right. \right) = \begin{cases} 10^b \left[\left(\frac{\nu_r}{\nu_n} \right)^{-\alpha_2} (1 - f) + f \left(\frac{\nu_r}{\nu_n} \right)^{-0.1} \right], & \nu_r > \nu_b \\ 10^b \left[\left(\frac{\nu_r}{\nu_n} \right)^{-\alpha_1} (1 - f) \left(\frac{\nu_b}{\nu_n} \right)^{\alpha_1 - \alpha_2} + f \left(\frac{\nu_r}{\nu_n} \right)^{-0.1} \right], & \nu_r < \nu_b \end{cases}, \quad (4.2)$$

where ν_n is the normalization frequency, ν_b the break frequency, α_1 (α_2) the spectral index below (above) ν_b , and b the normalization constant.

In the HSFG sample, as described in Sect. 4.4.1, we do not find f to be significantly greater than 0 for $\nu_n \sim 1$ GHz. We therefore simplified Eq. (4.2) to a broken power-law model for the log-normalized flux, using Eq. 3.1 from chapter 3

$$\log F \left(\nu_r \left| \begin{array}{c} \alpha_1 \\ \alpha_2 \\ b \\ \nu_b \end{array} \right. \right) = \begin{cases} -\alpha_2 \log \frac{\nu_r}{\nu_n} + b, & \nu_r > \nu_b, \\ -\alpha_1 \log \frac{\nu_r}{\nu_n} + b + (\alpha_1 - \alpha_2) \log \frac{\nu_b}{\nu_n}, & \nu_r < \nu_b, \end{cases}.$$

In the broken power-law model, the break frequency, ν_b , can be both a free parameter or fixed to a particular value prior to fitting.

In the broken power-law model, the break frequency, ν_b , can be both a free parameter or fixed to a particular value prior to fitting. The break frequency is derived using the MCMC method, explained in Sect. 3.2 of chapter 3, to constrain the broken power-law fit with the

break frequency as a free parameter. By inspecting the distribution of limits and detections, we find that the break frequency should lie above the highest frequency at which the last upper limit occurs. We thereby conclude that the break frequency would not be significantly affected by upper limits. The final fitting of the broken power-law model is performed using the ODR method, which accounts for the errors on both axes.

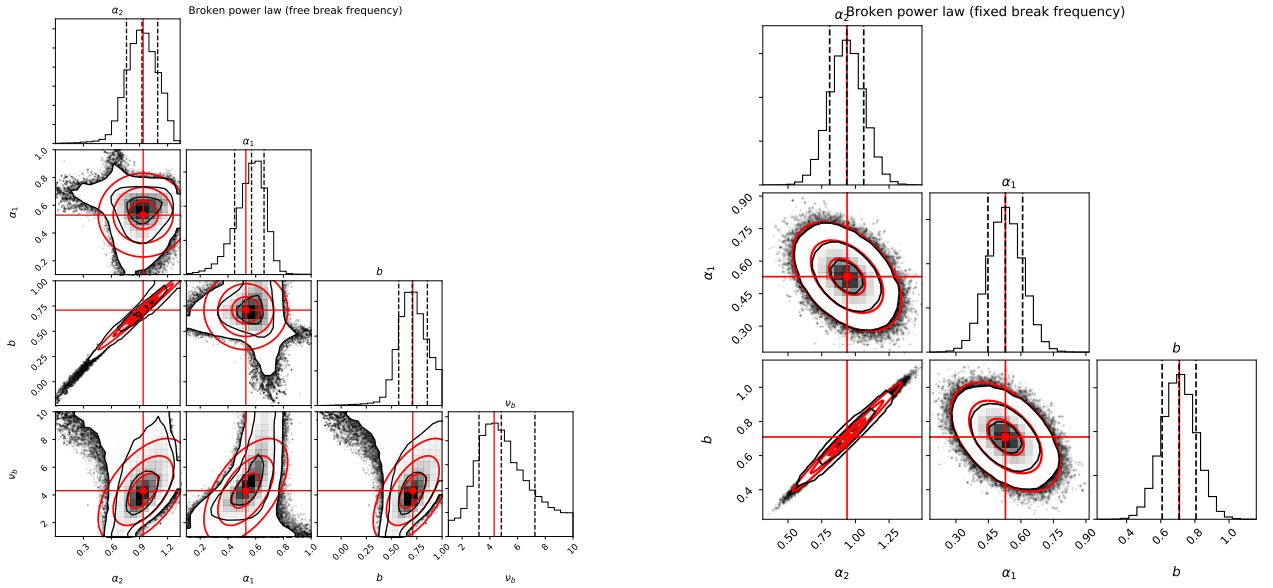


Figure 4.3: Broken power-law parameter estimation based on the MCMC algorithm used in deriving the break frequency. The red lines and ellipses show the results of the corresponding ODR fit, while the black contours show the 1, 2, and 3σ contours of the MCMC samples. The left panel shows the four-parameter fit with the break frequency treated as a free parameter, while the right panel shows the three-parameter broken power-law fit derived by fixing the break frequency to the best-fit value of ν_b in the left panel.

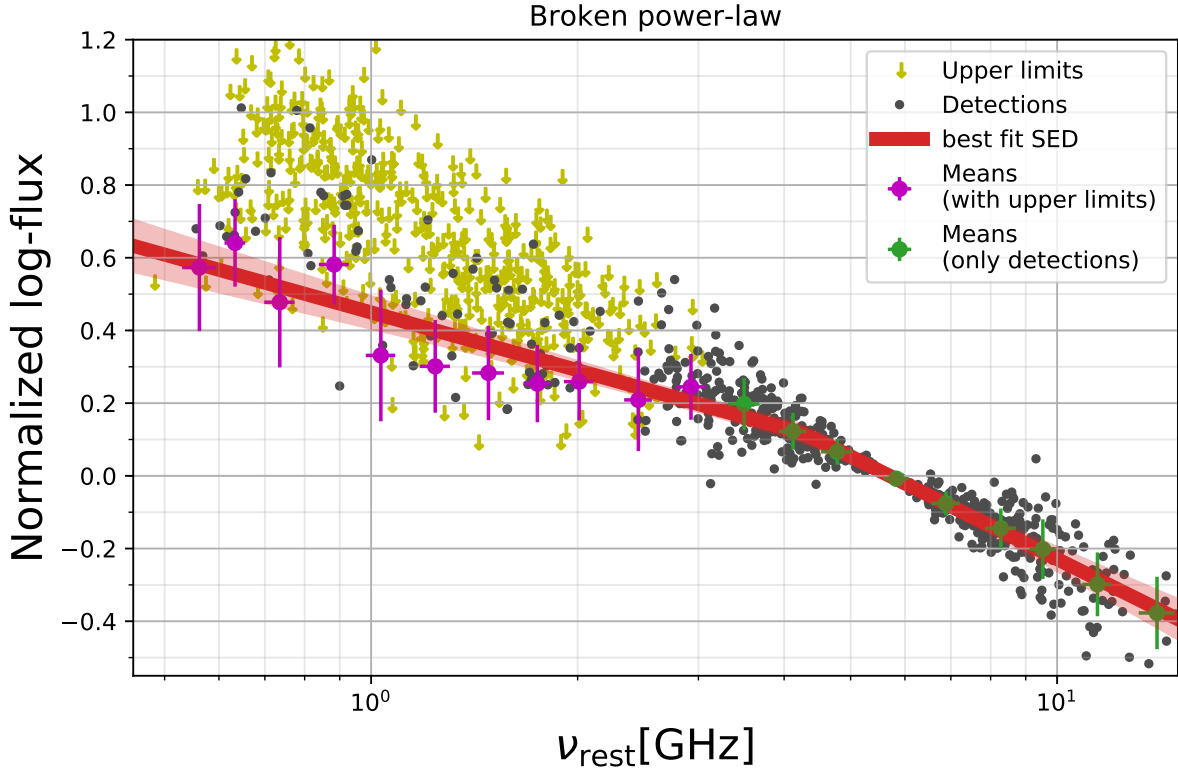


Figure 4.4: Average SED of the star-forming galaxy sample. Gray data points show individual detections, yellow arrows show upper limits, green circles show means in bins with no upper limits, and magenta circles show mean values derived using survival analysis. The red shaded interval shows the broken power-law fit with its 1σ error confidence interval. The errors derived using survival analysis are the standard deviations of the Weibull distribution that was fit on the Kaplan-Meier survival function.

4.3 Results

Here we present the results of the radio spectral index of the HSFG sample modeled by a broken power-law. In deriving the upper limits, we used the local RMS values from the GMRT maps.

The results of this procedure are shown in the left panel of Fig. (4.3), yielding a break frequency of $\nu_b = 4.3 \pm 0.6$ GHz (derived by the ODR method). Outside the 2σ confidence interval (red ellipses in the left panel of Fig. 4.3), the distribution starts to diverge from the simple form expected by the fit. Furthermore, the MCMC-derived parameter medians in the

left panel of Fig. (4.3) are not aligned with the ODR-derived means and the covariance ellipses derived by ODR fitting diverge from the σ contours of MCMC parameter estimates. This divergence probably arises because the SED shape is not equally sensitive to the change of every parameter in the model, resulting in deviations in the MCMC method that are more pronounced outside the 2σ confidence interval. Therefore, for the final result, we chose to fix the break frequency to the best-fit value provided by the ODR method and use it to fit the SED with a broken power-law with a fixed break frequency. The break frequency derived in this way is fixed to be $\nu_b = 4.3$ GHz for all following considerations. We fixed the value of ν_b to the ODR-derived best-fitting value and not to the MCMC median because of the MCMC behavior outside the 2σ confidence interval. We note that these results using break frequency values in the range from 3 – 6 GHz are not expected to affect the presented results. This is visible from the wide distribution of ν_b in the lower left plot in the left panel of Fig. (4.3). As presented in the right panel of Fig. (4.3), the reduced model behaves according to expectations of a normal distribution.

In Fig. (4.4) we show the average radio SED of HSGs and the derived broken power-law SED with fixed ν_b . The percentage of upper limits was $88 \pm 2\%$, which is consistent with $\alpha_1 \sim 0.5$ in Fig. (3.2). The spectral index changes from $\alpha_1 = 0.53 \pm 0.04$ below ν_b to $\alpha_2 = 0.94 \pm 0.06$ above ν_b . Considering the correction calculated using simulations in Sect. 3.3, the corrected spectral index is $\alpha_1^{corr} = 0.42 \pm 0.06$. Some of the models described in Sect 4.4.1 can explain this difference, for example, the difference of 0.5 is expected by model 3 assuming continuous injection of electrons (Pacholczyk 1977). Although our data clearly do not follow a simple power-law, we also report the result of the simple power-law fit of 0.67 ± 0.05 to facilitate a quick comparison to the literature.

In the left and right panels of Fig. (4.5), we compute mean values of redshift and star-formation rates for different rest-frame frequency bins of our radio SED, respectively. The mean redshifts and SFRs do not vary more than one standard deviation of all the data points ($\sigma_z = 0.3$, $\sigma_{\log \text{SFR}} = 0.6$) below 10 GHz, and there is no clear trend between contiguous frequency bins below this frequency. Only a small fraction of the data points, corresponding to $z > 2.3$, lie above 10 GHz, and they could not influence the SED fitting procedure significantly. We therefore

conclude that our average SED represents the SED of a single population of highly star-forming galaxies (with properties $z = 1.7 \pm 0.6$ and $\log SFR = 2.4 \pm 0.3$) over the whole frequency range from 300 MHz to 10 GHz.

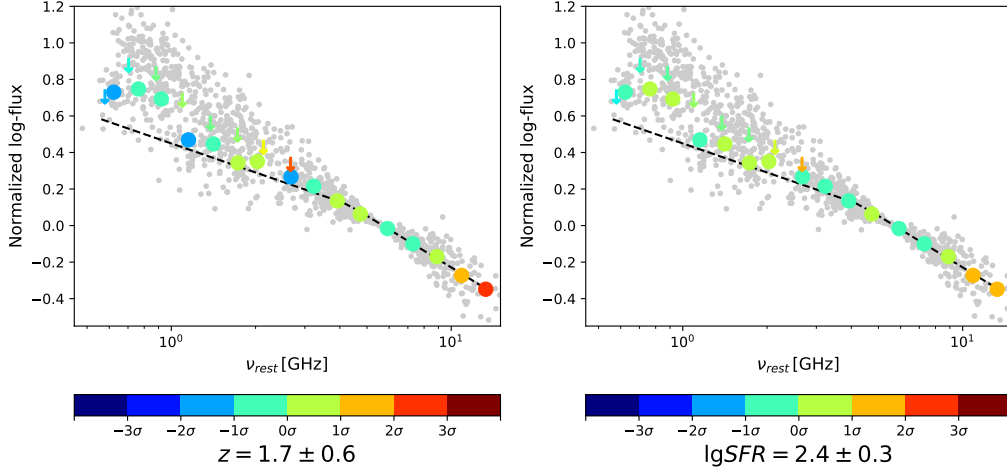


Figure 4.5: Mean properties of various rest-frame frequency bins in the HSFG radio SED. Shown are the mean redshift (left panel) and $\log SFR$ values (right panel) for each bin. Colored circles show the means of detections, while down-pointing arrows show the mean values for non-detections in each redshift bin. The dashed line shows the best-fitting broken power-law SED.

4.4 Discussion

In Sect. 4.4.1 we discuss the shape of the radio SED of star-forming galaxies and alternative, physically motivated fitting strategies. In Sect. 4.4.2 we discuss the impact of the shape of the radio SED on the infrared-radio correlation.

4.4.1 Shape of the radio SED

In the left panel of Fig. (4.7), we overplot the different SEDs from the literature and our broken power-law (BPL). Our results, covering a broad range of redshifts, are in overall agreement with

literature SEDs derived for (U)LIRGS in the nearby Universe ($z \lesssim 0.1$, $\text{SFR} > 10 \text{ M}_\odot/\text{yr}$) (for galaxies with an SFR in the $50 - 150 \text{ M}_\odot/\text{yr}$ range [Clemens et al. 2008](#); [Leroy et al. 2011](#)). We find disagreement with the typical model of “normal” star-forming galaxies (NSFGs) above $\sim 10 \text{ GHz}$ ([Klein et al. 1988](#); [Condon 1992](#); [Tabatabaei et al. 2017](#)), which may be due to the different thermal fractions in normal and highly star-forming galaxies. In the nearby Universe ($z < 0.1$), the typical SED of NSFGs is described by a simple nonthermal power-law with a spectral index of ~ 0.8 and a thermal fraction of $8 - 10\%$ at $\sim 1 \text{ GHz}$ ([Klein et al. 1988](#); [Condon & Yin 1990](#)), while studies of HSFGs find a flat spectrum around $\sim 1 \text{ GHz}$ and a steepening spectrum above 10 GHz ([Clemens et al. 2008](#); [Leroy et al. 2011](#)).

For our HSFGs with $\text{SFR} > 100 \text{ M}_\odot/\text{yr}$, we find a relatively flat ($\alpha \sim 0.5$) spectral index below $\sim 4 \text{ GHz}$. This result is in line with previous studies of (U)LIRGs ([Clemens et al. 2008](#); [Leroy et al. 2011](#); [Galvin et al. 2018](#)). There are multiple effects that could produce a flattening in the spectrum of galaxies in the radio, but only synchrotron aging and free-free absorption play a role in the $1 - 10 \text{ GHz}$ range. Effects like synchrotron self-absorption and the Razin-Tsytovič effect ([Razin 1960](#); [Razin, V. N. 1951](#)), an effect that is due to the refractive index of plasma in the radio, can be ruled out because they are usually found at frequencies below 1 GHz ([Deeg et al. 1993](#)). These effects could be even more suppressed, as magnetic fields have been found to be stronger for higher SFRs ([Tabatabaei et al. 2017](#)). Furthermore, we do not expect to be able to successfully find evidence for any more complex shape of the SED such as multi-peak behavior of free-free absorption because of the different opacities of different star-forming regions within a galaxy, as any such behavior would be averaged out when constructing an average SED. [Tabatabaei et al. \(2017\)](#) instead pointed out that the nonthermal spectral index (which can be compared to our α_1) flattens with increasing SFR density, which gives a possible explanation why this effect is pronounced in our HSFG sample.

[Bressan et al. \(2002\)](#) modeled the radio SEDs of dusty starburst galaxies that initially have SFRs in the range of $100 - 1000 \text{ M}_\odot/\text{yr}$. They concluded that if the SFR changes abruptly, the core-collapse supernova rate will lag behind as a result of the finite lifetimes of stars, leading to a suppressed synchrotron emission in young starbursts. This effect can produce flat spectra below 10 GHz , as the thermal fraction is initially very high. [Prouton et al. \(2004\)](#) analyzed the

behavior of the thermal fraction with the age of the starburst for galaxies with an SFRs from 30 to $\sim 150 M_{\odot}/\text{yr}$. They found that the thermal fraction decreases from the initial value of almost 100% to below 10% at 1.4 GHz within $10^{7.5}$ yr.

Table 4.1: Rankings of different fitted models with their parameters. For simplicity, we show models without their normalization parameter and indicate the additional contribution of free-free emission with a thermal fraction at 1GHz by ‘FFE’. We show the rankings based on the Akaike and Bayesian information criteria and the log-likelihood test ($\ln L$).

Model parameters	Normalized (normalized) flux density	Ranking		
		AIC	BIC	$\ln L$
Broken power-law ^a $\alpha_1 = 0.53 \pm 0.04$ ($\alpha_1^{corr} = 0.42 \pm 0.06$) $\alpha_2 = 0.94 \pm 0.06$	Eq. (3.1)	2	2	1
Model (1) - mixed model ^b $\alpha = 0.74 \pm 0.06$ $\tau_1 = 0.2 \pm 0.2$	$\nu^{-\alpha+2.1} \left(1 - e^{-\frac{\tau_1}{\nu^{2.1}}}\right)$	6	5	6
Model (2) - foreground screen model ^b $\alpha = 0.73 \pm 0.06$ $\tau_1 = 0.11 \pm 0.08$	$\nu^{-\alpha} e^{-\frac{\tau_1}{\nu^{2.1}}}$	6	7	7
Model (3) - synchrotron aging model ^b $\alpha = 0.24 \pm 0.06$ $\Delta\alpha = 0.55 \pm 0.04$	$\frac{\nu^{-\alpha}}{1 + \left(\frac{\nu}{\nu_b}\right)^{\Delta\alpha}}$	4	4	5
Model (4) - synchrotron self-absorption model ^c $\alpha = 0.70 \pm 0.05$ $\nu_b = 0.76 \pm 0.07$ GHz	$\nu^{5/2} \left(1 - e^{-\left(\frac{\nu}{\nu_b}\right)^{-\alpha-5/2}}\right)$	8	8	8
Model (5) - (Lisenfeld et al. 2004) ^b $\alpha = 0.47 \pm 0.03$	$\nu^{-\alpha} \left(1 - \left(1 - \sqrt{\frac{\nu}{\nu_b}}\right)^{1.1}\right)$	1	1	3
Model (6a) -synchrotron aging+FFE ^b $\alpha = 0.24 \pm 0.07$ $\Delta\alpha = 0.55 \pm 0.04$ $f_{ih}(1 \text{ GHz}) = 0.00 \pm 0.02$	$\frac{(1-f_{ih}(\nu_n))\left(\frac{\nu}{\nu_n}\right)^{-\alpha}}{1 + \left(\frac{\nu}{\nu_b}\right)^{\Delta\alpha}} + f_{ih}(\nu_n) \left(\frac{\nu}{\nu_n}\right)^{-0.1}$	7	5	4
Model (6b) - Lisenfeld et al. (2004)+FFE ^b $\alpha = 0.50 \pm 0.06$ $f_{ih}(1 \text{ GHz}) = 0.01 \pm 0.02$	$(1 - f_{ih}(\nu_n)) \left(\frac{\nu}{\nu_n}\right)^{-\alpha} \left(1 - \left(1 - \sqrt{\frac{\nu}{\nu_b}}\right)^{1.1}\right) + f_{ih}(\nu_n) \left(\frac{\nu}{\nu_n}\right)^{-0.1}$	3	3	2

(a) The broken power-law model was included in the table for comparison. (b) See Pacholczyk (1977) for details. (c) See Condon & Ransom (2016) for details.

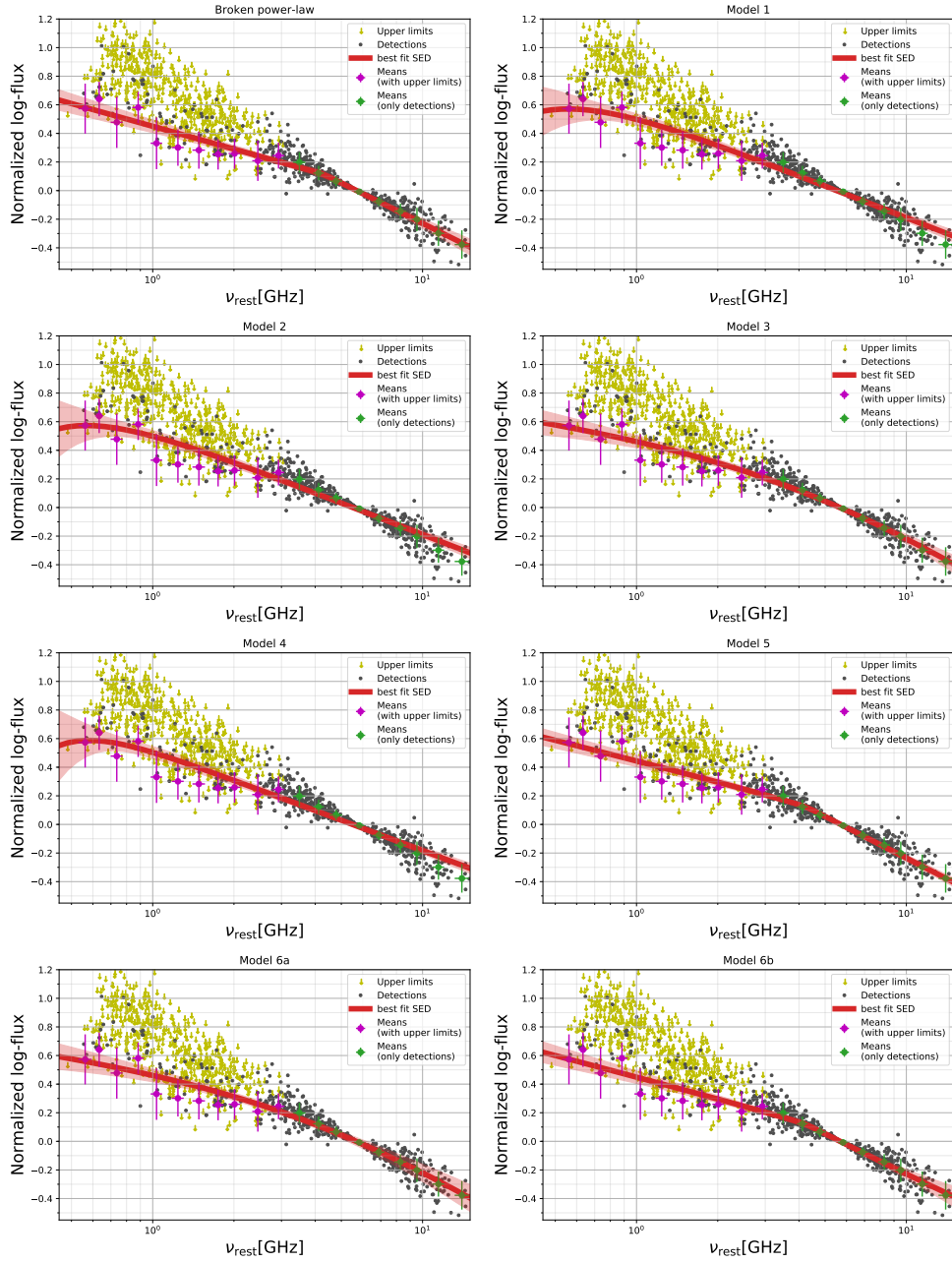


Figure 4.6: Average radio SED of HSFGs for the models from Sect. 4.4.1 plotted as in Fig. 4.4. The red solid lines and shaded intervals represent the best-fitting parameters of Table 4.1 and confidence intervals, respectively.

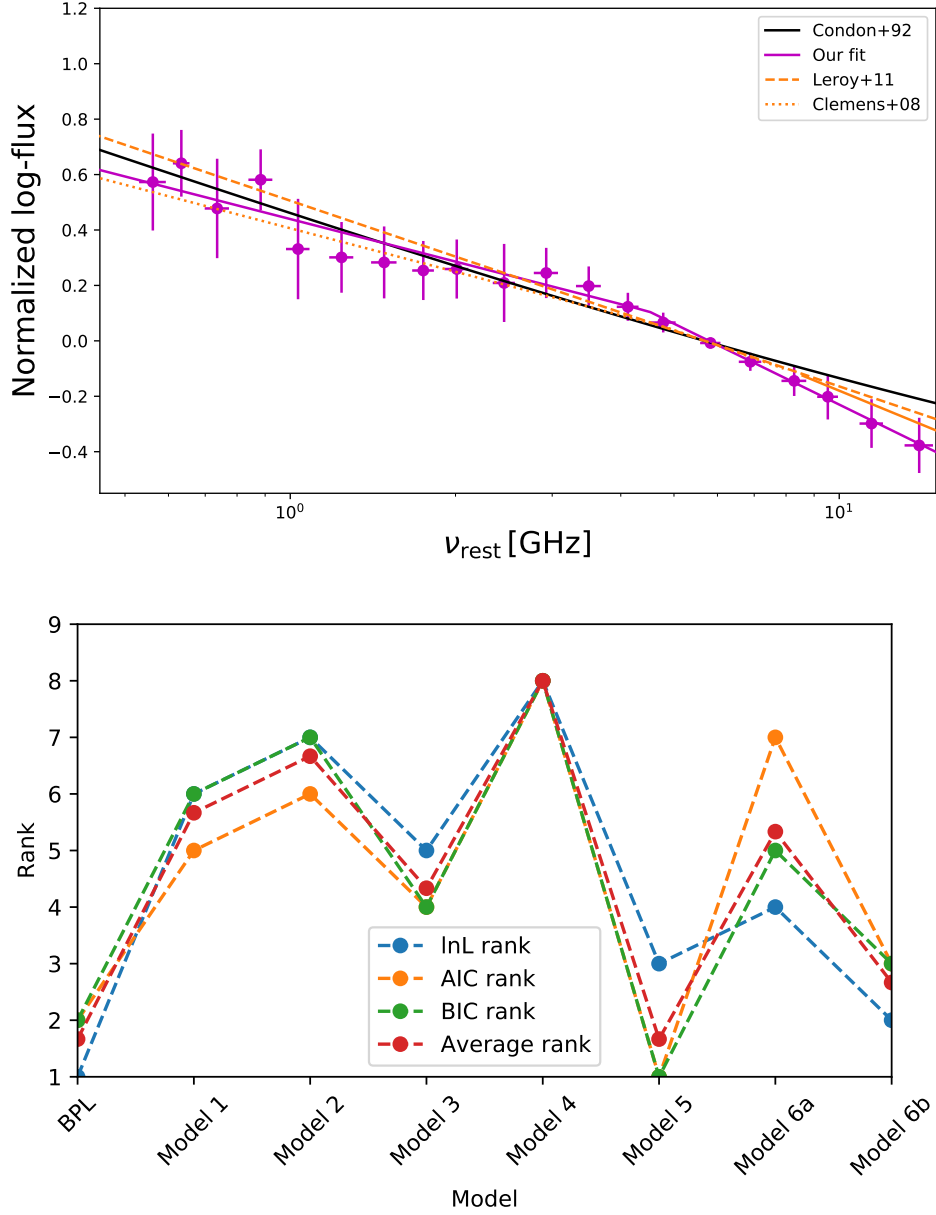


Figure 4.7: Left panel: Comparison of the average SED data (magenta points) and our broken power-law fit (magenta lines) with different literature SEDs (Clemens et al. 2008; Leroy et al. 2011) for ULIRGs. For comparison, we show the Condon (1992) model for a normal SFG. Right panel: Comparison of the different goodness-of-fit tests for different models. We show the log-likelihood test and the Akaike and Bayesian information criteria. We give the average of these three criteria for reference.

For the HSFGs in the COSMOS field, we find a steep ($\alpha \sim 1$) spectrum above 4 GHz that does not exhibit signs of free-free emission. A steep spectral index has also been found by [Galvin et al. \(2018\)](#) ($\alpha = 1.06$) for galaxies with an SFR in the range of $\sim 50 - 250 M_{\odot}/\text{yr}$, which they associated with a steeper injection index of the CR distribution. [Clemens et al. \(2008\)](#) found a similar trend (for galaxies with an SFR $\sim 50 - 150 M_{\odot}/\text{yr}$) that they tried to explain using the continuous injection model, which can explain differences in spectral indices up to $\Delta\alpha \approx 0.5$.

Since the SED of HSFGs has been found to differ from a simple power-law, we fit the following models often used in literature (e.g., [Calzetti et al. 1994](#); [Condon 1992](#); [Clemens et al. 2008](#); [Condon & Ransom 2016](#); [Lisenfeld et al. 2004](#); [Klein et al. 2018](#)) that might explain this behavior:

1. Mixed model

- This model assumes that the power-law synchrotron spectrum with a spectral index α is attenuated by free-free absorption with opacity $\tau_{\nu} = \frac{\tau_1}{\nu^{2.1}}$ arising from the same region.

2. Foreground screen model

- This model assumes that the power-law synchrotron spectrum with a spectral index α is attenuated by free-free absorption with opacity $\tau_{\nu} = \frac{\tau_1}{\nu^{2.1}}$ arising from a region that is in our line of sight, but is not cospatial with the emitting region.

3. Synchrotron aging model

- In contrast to the previous two models, this model does not take into account free-free absorption of synchrotron radiation initially described by a simple power-law. This model instead explains the shape of the SED by taking into account that the cosmic ray electron population loses energy with time. The model predicts a spectrum that was initially described by an injection index that produces a power-law SED with a spectral index α that gradually steepens above a frequency ν_b to a spectral index $\alpha + \Delta\alpha$ due to aging.

4. Synchrotron self-absorption

- The synchrotron self-absorption model has the same form as model 1, with the opacity of the form $\tau_\nu = (\nu/\nu_b)^{-(\alpha+5/2)}$, where α is the synchrotron spectral index and ν_b the break frequency.

5. [Lisenfeld et al. \(2004\)](#) model

- In this model, the electrons are propagated through and eventually out of the galactic halo by means of convective winds.

6. Free-free emission

- Models 1-5 can be extended by including an additional contribution of thermal free-free emission, f_{th} , as described by Eq. (4.2). We consider the following:
 - (a) Synchrotron aging model with free-free emission
 - (b) [Lisenfeld et al. \(2004\)](#) model with free-free emission

Among the models listed above, free-free absorption and synchrotron aging models would reproduce flattening at lower frequencies, while models (6a)-(6b) can be used to estimate the contribution of free-free emission to the spectrum. The parameterization of the fitted SEDs and their parameters can be found in Table (4.1). We find that models (1) and (2), which include free-free absorption, fit the low-frequency data well. They overestimate the measured flux at higher frequencies (by ~ 0.1 dex at 10 GHz), however. The synchrotron aging model (3) agrees with the broken power-law at both low and high frequencies. The low-frequency spectral index corresponds to the value typically found in supernova remnants (SNRs) and the Galactic plane in the Milky Way ([Green 2014](#); [Klein et al. 2018](#)). We tried to constrain the thermal fraction with the broken power-law model by using Eq. (4.2), but found a strong degeneracy between parameters f_{th} and α_2 and therefore cannot draw meaningful results from this model. This degeneracy is expected for this class of models ([Transtrum et al. 2010](#)) and can only be broken by more observations at even higher frequency (> 10 GHz).

To compare how well these models explain our dataset, we used the log-likelihood test and the Akaike and Bayesian information criteria (AIC and BIC, respectively). The greatest log likelihood means that the broken power-law is optimal in terms of the fitting. In contrast to the

log-likelihood test, AIC and BIC criteria favor models with a smaller number of free parameters, penalizing the models with a higher number of free parameters by higher AIC and BIC values. In the right panel of Fig. (4.7) we show the ranking in our statistical analyses (log likelihood, AIC, and BIC) for the models in Table (4.1). The results reported in Table (4.1) were computed using the ODR method restricted to a 2σ subset of the respective model's parameter space, derived using the MCMC procedure.

We found that our broken power-law model has the greatest log likelihood and the second lowest AIC and BIC values. The BPL model shares the same average rank of the AIC, BIC, and log-likelihood ranks with model (5) because model (5) has fewer free parameters and is therefore favored by the AIC and BIC values, while it ranks third on the log-likelihood test. As shown in Fig. 4.6, the broken power-law model and models (3), (5), (6a), and (6b) describe the average radio SED points sufficiently well. We therefore conclude that we can favor models ranking the lowest on all three tests. In addition to the broken power-law, the highest ranking models are model (5) and its extension that includes free-free emission (model 6b). Additionally, literature models of HSFGs (Clemens et al. 2008; Leroy et al. 2011) score better in all three tests than the standard NSFG model (Condon 1992). This comparison means that HSFGs do not have the same SED shape as the NSFGs. The main difference to the NSFGs is the behavior at higher frequencies, which might be due to a smaller thermal fraction at higher SFR. Since our empirical broken power-law describes our dataset better than simple theoretical models (models 1-3), and different goodness-of-fit criteria sort their preference differently, we conclude that neither simple free-free absorption over the whole sample nor synchrotron aging are the only drivers of the radio SED of HSFGs.

4.4.2 Infrared-radio correlation

Recent stacking and survival analysis studies (Iverson et al. 2010; Magnelli et al. 2015; Delhaize et al. 2017; Calistro Rivera et al. 2017) have found the infrared-radio correlation (described by the q parameter) to decrease with increasing redshift. Delhaize et al. (2017) mentioned the possibility that the computation of rest-frame radio luminosity via a K-correction using a single power-law assumption of the star-forming galaxies' SED could produce a redshift-dependent

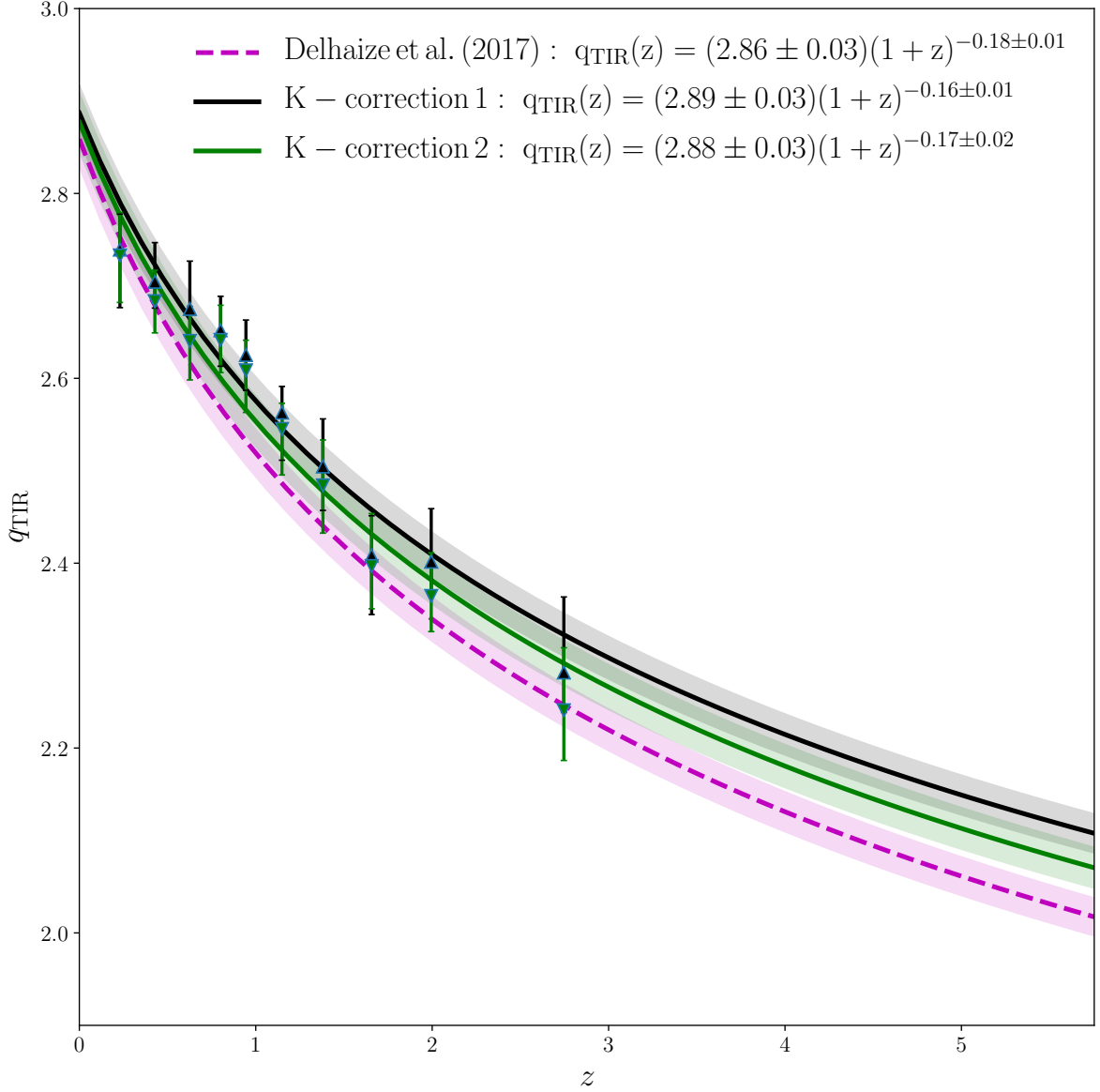


Figure 4.8: Infrared-radio correlation, q_{TIR} , as a function of redshift for galaxies in the [Delhaize et al. \(2017\)](#) joint radio and infrared sample. We used the broken power-law SED from this paper for star-forming galaxies with an $SFR > 10 M_{\odot}/\text{yr}$ and the following SED shapes for $SFR < 10 M_{\odot}/\text{yr}$ ([Tabatabaei et al. 2017](#)): 1) a simple power-law SED with a spectral index of 0.79 (black line, K-correction 1) or a nonthermal spectral index of 0.97, and a 10% thermal fraction at 1 GHz (green line, K-correction 2). We show the [Delhaize et al. \(2017\)](#) relation for reference (magenta line).

trend.

Here we calculate the infrared-radio correlation by using a K-correction based on our best-fitting broken power-law SED for galaxies with an $SFR > 10 M_{\odot}/\text{yr}$ and the combination of thermal and nonthermal emission, following Eq. (4.2), with a nonthermal spectral index of $\alpha = 0.97$ and a 10% thermal fraction (Tabatabaei et al. 2017) for $SFR < 10 M_{\odot}/\text{yr}$ (described in detail in Sect. B). We adopted a threshold between these two types of SFGs at $10 M_{\odot}/\text{yr}$, considering that our results are consistent with studies of (U)LIRGs ($SFR > 10 M_{\odot}/\text{yr}$ Clemens et al. 2008; Leroy et al. 2011). We find that the broken power-law derived luminosity is 20% lower than that derived by assuming a 0.7 spectral index for redshifts below $z \sim 1$. We also find that the difference is negligible for sources above $z \gtrsim 2$. We constrained the infrared-radio correlation using the same procedure as applied by Delhaize et al. (2017). In the infrared, we used Herschel-detected $\geq 5\sigma$ objects, with the COSMOS2015 (Laigle et al. 2016) $24\mu\text{m}$ catalog as priors to minimize blending, while in the radio, we used the Smolčić et al. (2017a) 3 GHz Large Project Counterpart catalog. If an object is undetected in the radio, we estimated its upper q limit as five times the local RMS value in the 3 GHz map convolved to a resolution at which its peak flux ceases to change significantly with increased convolution, while we used lower q limits based on upper limits to the infrared luminosity, derived through integration of the best-fit SED. For details, see Delhaize et al. (2017). In short, we used the joint radio- and infrared-detected samples of star-forming galaxies in the COSMOS field, and then used the survival analysis method to find the mean q value for different redshift bins and fit a power law of the form

$$q(z) = q_0(1 + z)^n, \quad (4.3)$$

where q_0 is the value of q derived for $z = 0$ and n is the exponent. Contrary to what would be expected from theory (Murphy 2009), but in line with previous studies (Delhaize et al. 2017; Calistro Rivera et al. 2017), the q value, shown in Fig. (4.8) and computed taking into account the K-corrections described above, decreases with redshift with $n = -0.17 \pm 0.02$, and $q_0 = 2.88 \pm 0.03$. In Fig. (4.8) we show the $q - z$ trend derived under various SED assumptions, as described above. In all the cases, we find that q decreases with increasing redshift.

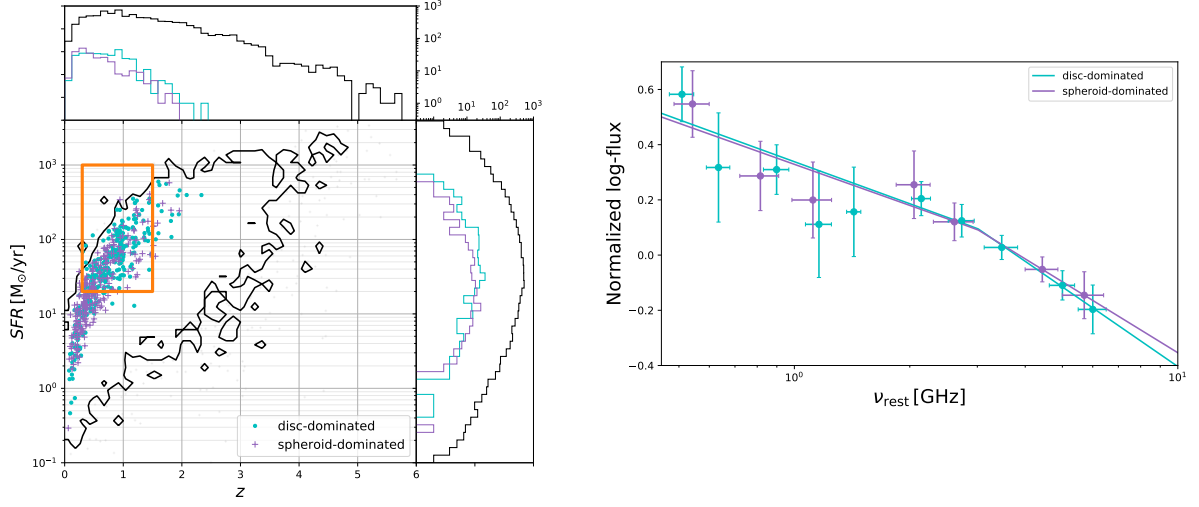


Figure 4.9: Left panel: Distribution of sources in the $SFR - z$ plane, analogous to Fig. (4.1). Cyan points and magenta crosses indicate the distributions of disk- and spheroid-dominated subsamples of star-forming galaxies, as defined in Molnár et al. (2018). The 3σ contours of the CSFG sample are shown as black lines, and the orange rectangle marks the edges of the chosen nearly complete disk- and spheroid-dominated samples. The right panel shows their respective SEDs.

We therefore conclude that the shape of the radio SED, as assumed here, probably does not explain the $q - z$ trend. For comparison, in Fig. (4.8), we also show the resulting $q - z$ trend based on a simple power-law fit with $\alpha = 0.79$ for galaxies with an $SFR < 10 M_{\odot}/\text{yr}$ (Tabatabaei et al. 2017). This fit is less complex, but has a lower parameter uncertainty. We find that this simplification does not significantly alter the resulting $q - z$ trend ($n = -0.18 \pm 0.01$ and $q_0 = 2.89 \pm 0.03$).

Molnár et al. (2018) have studied the impact of morphology on the evolution of the q parameter (for star-forming galaxies covering a broad SFR range of $1 - 1000 M_{\odot}/\text{yr}$ and in the redshift range of $0.2 - 1.5$) and found that spheroid-dominated star-forming galaxies show a steep redshift behavior ($n = -0.19 \pm 0.02$), while disk-dominated galaxies do not ($n = -0.04 \pm 0.01$). They argued that in order for the radio spectral index of spheroid-dominated galaxies to explain

the $q - z$ behavior, it would have to decrease with redshift from $\alpha = 0.7$ at $z = 0.8$ to $\alpha = 0.45$ at $z = 1.5$. To investigate this, we have derived an average radio SED for complete samples of star-forming galaxies based on morphology. To match the selection performed by Molnár et al. (2018), we selected SFGs with an $SFR > 20 M_{\odot}/\text{yr}$ to be fairly complete out to a redshift of $z = 1.5$, with the requirement that we included only galaxies marked as either spheroid- or disk-dominated, based on the classification of Molnár et al. (2018). We show the position in the $SFR - z$ plane of their respective complete subsets in the left panel of Fig. (4.9) and their respective broken power-law fits in the right panel. Overall, we find that the median MCMC-derived break frequency is 3 GHz and that the differences in the parameters of the broken power-law fit between spheroid ($\alpha_2 = 0.9 \pm 0.3$, $\alpha_1 = 0.5 \pm 0.1$) and disk-dominated ($\alpha_2 = 1 \pm 0.2$, $\alpha_1 = 0.51 \pm 0.09$) galaxies are smaller than 1σ . This suggests that a difference in radio-SEDs of these morphologically different galaxies, and thus a potentially different K-correction, is not the cause of the differing trend found by Molnár et al. (2018).

4.5 K-correction considerations

Generally, the luminosity at a rest-frame frequency ν_{e2} , $L(\nu_{e2})$, is connected to the flux measured at the observed frequency ν_{o2} , $S(\nu_{o2})$, as

$$L(\nu_{e2}) = \frac{4\pi D_L^2}{1+z} S(\nu_{o2}), \quad (4.4)$$

where z is the object redshift and the observed frequency is connected to the emitted frequency by $\nu_e = \nu_o(1+z)$. This relation does not depend explicitly on the shape of the SED, so we have the relation connecting ratios of luminosities at two different frequencies

$$\frac{L(\nu_{e2})}{L(\nu_{e1})} = \frac{S(\nu_{e2})}{S(\nu_{e1})} = \frac{S(\nu_{o2})}{S(\nu_{o1})}. \quad (4.5)$$

We can model $\frac{S(\nu_{e2})}{S(\nu_{e1})}$ by an SED. Inserting Eq. (4.5) into the first equation, we obtain

$$L(\nu_{e2}) = \frac{4\pi D_L^2}{1+z} \frac{S(\nu_{e2})}{S(\nu_{o1}(1+z))} S(\nu_{o1}). \quad (4.6)$$

We can now proceed to find the K-correction for a broken power-law.

4.5.1 Broken power-law

We assumed that the spectrum is that of a broken power-law with spectral indices α_0, α_1 , and so on, with each new spectral index, α_k , beginning above a fixed frequency ν_k . In this case, the flux for each frequency range k can be expressed as

$$\lg S_k = -\alpha_k \lg \nu + b_k, \quad (4.7)$$

where b_k is the k -th bin normalization constant. Using the fact that the flux needs to be a continuous function of ν , we can roll back b_k to the first bin, b_0 as

$$b_k = b_0 + \sum_{j=0}^{k-1} (\alpha_{k-j} - \alpha_{k-(j+1)}) \lg \nu_{k-j} = b_0 + \sum_{j=0}^{k-1} \Delta \alpha_{k-j} \lg \nu_{k-j}. \quad (4.8)$$

The bin number, k , is easily determined from ν and the list of break frequencies ν_i , giving functions $k(\nu)$ and $\alpha(\nu)$. We can repeat this process for each frequency ν_{e1} and ν_{e2} , yielding

$$\frac{S(\nu_{e2})}{S(\nu_{o1}(1+z))} = \frac{1}{(1+z)^{-\alpha(\nu_{o1}(1+z))}} \left(\frac{\nu_{e2}^{-\alpha(\nu_{e2})}}{\nu_{o1}^{-\alpha(\nu_{o1}(1+z))}} \right) 10^{b_k(\nu_{e2}) - b_k(\nu_{o1}(1+z))}. \quad (4.9)$$

Finally, we obtain the luminosity as

$$L(\nu_{e2}) = \frac{4\pi D_L^2 S(\nu_{o1})}{(1+z)^{1-\alpha(\nu_{o1}(1+z))}} \left(\frac{\nu_{e2}^{-\alpha(\nu_{e2})}}{\nu_{o1}^{-\alpha(\nu_{o1}(1+z))}} \right) 10^{b_k(\nu_{e2}) - b_k(\nu_{o1}(1+z))}. \quad (4.10)$$

For the broken power-law with a single break frequency, $\nu_{e2} = 1.4 \text{ GHz}$ and $\nu_{o1} = 3 \text{ GHz}$, we can express Eq. (4.10) as

$$L_{1.4 \text{ GHz}} = 4\pi D_L^2 S_{3 \text{ GHz}} \begin{cases} \frac{1}{(1+z)^{1-\alpha_1}} \left(\frac{1.4^{-\alpha_1}}{3^{-\alpha_1}} \right), & 3 \text{ GHz}(1+z) < \nu_b \\ \frac{1}{(1+z)^{1-\alpha_2}} \left(\frac{1.4^{-\alpha_1}}{3^{-\alpha_2}} \right) 10^{-(\alpha_2-\alpha_1) \log \nu_b}, & 3 \text{ GHz}(1+z) > \nu_b \end{cases}. \quad (4.11)$$

The left panel of Fig. (4.10) shows the luminosity at 1.4 GHz rest-frame derived using various K-corrections. From the right panel of the same figure, we see that luminosities are by up to 26% overestimated compared to the broken power-law for $z \leq 1$ if we assume a single spectral index of 0.7.

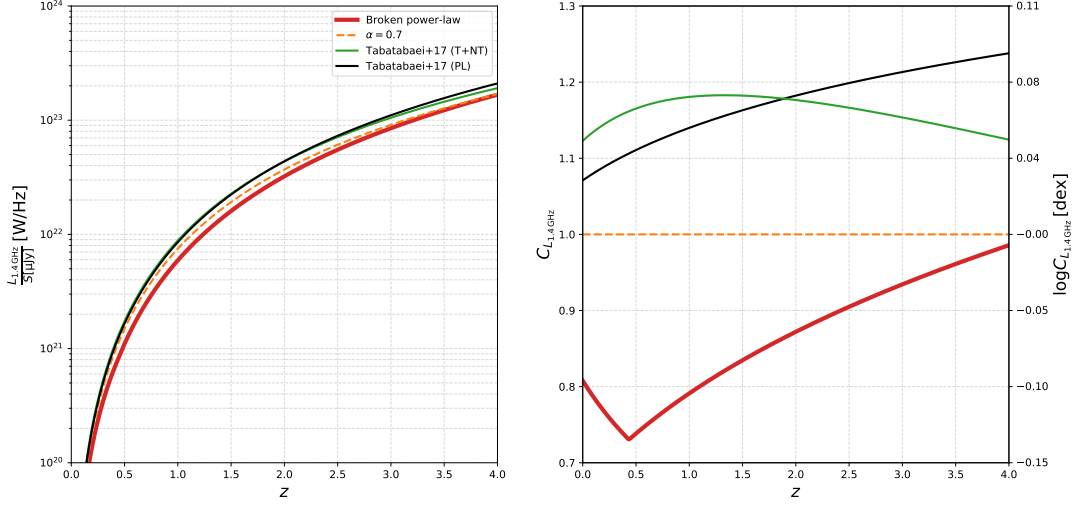


Figure 4.10: Left panel: Luminosity at a rest-frame frequency of 1.4 GHz for different redshifts computed using the fiducial value of $1 \mu\text{Jy}$ for (observer frame) 3 GHz flux densities, while the right panel shows the correction of 1.4 GHz radio luminosity, $C_{L_{1.4\text{GHz}}}$ computed using the spectral index of $\alpha = 0.7$ as reference. Solid lines are corrections based on either a broken power-law (red line), derived in Sect. 4.3 for our HSFG sample, and an SED (black line) of normal star-forming galaxies based on a 0.97 nonthermal spectral index and a 10% thermal fraction (Tabatabaei et al. 2017). The green line shows the SED of NSFGs based on a simple power law ($\alpha = 0.79$ Tabatabaei et al. 2017).

4.5.2 K-corrections and thermal fraction

We used the results of Tabatabaei et al. (2017) to derive luminosities of normal star-forming galaxies. They have found that the SED of normal star-forming galaxies has a steep nonthermal spectral index ($\alpha_2 = 0.97$) and a $\sim 10\%$ thermal fraction at 1.4 GHz. The K-correction in this case is

$$L_{1.4\text{GHz}} = \frac{4\pi D_L^2}{1+z} \frac{S_{3\text{GHz}}}{(1-f_{th}) \left(\frac{3(1+z)}{1.4} \right)^{-\alpha_2} + f_{th} \left(\frac{3(1+z)}{1.4} \right)^{-0.1}}. \quad (4.12)$$

As discussed in Sect. 4.4.2, we compared the $q-z$ trends derived using this K-correction and also the K-correction based on the Tabatabaei et al. (2017) simple power-law spectral index of

0.79. In the next section, we derive the average correction of radio luminosity needed for a sample of galaxies consisting of both NSFGs and HSFGs.

4.5.3 Average K-corrections

To better understand the impact of the different K-corrections on the $q - z$ trend, we also derived corrections of $L_{1.4\text{ GHz}}$ for an average 1.4 GHz luminosity by assuming a distribution of fluxes, $f(\text{SFR}, z)$, that is dependent on both SFR and z . We started by rewriting Eq. (4.10) for SFGs as $L_{1.4\text{ GHz}} = K(\text{SFR}, z)S_{3\text{ GHz}}$, where $S_{3\text{ GHz}}$ is the observed flux density. As discussed in Sect. 4.4.2, we used a K-correction, K_{BPL} , based on the broken power-law SED for galaxies with an $\text{SFR} > 10\text{ M}_\odot/\text{yr}$ and the [Tabatabaei et al. \(2017\)](#) SED-based K-correction, K_{Tab} , for $\text{SFR} < 10\text{ M}_\odot/\text{yr}$. The average 1.4 GHz luminosity at redshift z is

$$\langle L_{1.4\text{ GHz}} \rangle(z) = \int f(\text{SFR}, z) K(\text{SFR}, z) S(\text{SFR}, z) d\text{SFR}. \quad (4.13)$$

We divided this average luminosity by the average luminosity, $\langle L_{1.4\text{ GHz}} \rangle(z)_\alpha$, derived by assuming a K-correction, K_α , based on a simple power-law SED with a single spectral index $\alpha = 0.7$, yielding the correction of $L_{1.4\text{ GHz}}$,

$$C_{L_{1.4\text{ GHz}}}(p_{<10}, z) = (1 - p_{<10}(z)) \frac{K_{BPL}(z)}{K_{\alpha=0.7}(z)} + p_{<10}(z) \frac{K_{Tab}(z)}{K_{\alpha=0.7}(z)}, \quad (4.14)$$

where we have introduced the fraction of sources with an SFR below $10\text{ M}_\odot/\text{yr}$, $p_{<10}$, defined as

$$p_{<10} = \frac{\int_{<10\text{ M}_\odot/\text{yr}} f(\text{SFR}, z) S(\text{SFR}, z) d\text{SFR}}{\int f(\text{SFR}, z) S(\text{SFR}, z) d\text{SFR}}. \quad (4.15)$$

Given the finite number of sources in our sample, this fraction is estimated as the sum of fluxes of all sources within a redshift bin that have an $\text{SFR} < 10\text{ M}_\odot/\text{yr}$ divided by the sum of fluxes of all sources within the redshift bin. We see that $C_{L_{1.4\text{ GHz}}}(p_{<10}, z)$ is a linear interpolation between K-corrections derived by assuming a broken power-law SED and the [Tabatabaei et al. \(2017\)](#) SED and can be useful for quickly estimating the impact of using a simple K-correction based on an $\alpha = 0.7$ power-law SED instead of a more elaborate SED.

Table 4.2: Average corrections of luminosity at 1.4 GHz needed if the K-correction was performed by assuming a power-law SED with a spectral index of 0.7. The corrections were derived for the average luminosity at 1.4 GHz, as described in Sect. 4.5, and are based on the assumption that galaxies with an $\text{SFR} > 10 M_{\odot}/\text{yr}$ follow the broken power-law (BPL) SED and that galaxies with an $\text{SFR} < 10 M_{\odot}/\text{yr}$ follow the SED based on Eq. (4.2), with the nonthermal spectral index and thermal fraction taken from [Tabatabaei et al. \(2017\)](#). The percentage $p_{<10}$ is the percentage of 3 GHz flux that is due to galaxies with an $\text{SFR} < 10 M_{\odot}/\text{yr}$. Columns of $p_{<10} = 0\%$ and $p_{<10} = 100\%$ are also exact corrections for single objects derived by assuming the BPL or the [Tabatabaei et al. \(2017\)](#) SEDs, respectively. The values in parentheses are correction $C_{L_{1.4\text{GHz}}}$ expressed in dex.

z	$C_{L_{1.4\text{GHz}}} (\log C_{L_{1.4\text{GHz}}} [\text{dex}])$				
	$p_{<10}$				
	0%	25%	50%	75%	100%
0.0	0.81 (-0.09)	0.89 (-0.05)	0.97 (-0.02)	1.04 (0.02)	1.12 (0.05)
0.5	0.74 (-0.13)	0.85 (-0.07)	0.95 (-0.02)	1.06 (0.02)	1.17 (0.07)
1.0	0.79 (-0.10)	0.89 (-0.05)	0.99 (-0.01)	1.08 (0.03)	1.18 (0.07)
1.5	0.83 (-0.08)	0.92 (-0.04)	1.01 (0.00)	1.10 (0.04)	1.18 (0.07)
2.0	0.87 (-0.06)	0.95 (-0.02)	1.02 (0.01)	1.10 (0.04)	1.18 (0.07)
2.5	0.90 (-0.04)	0.97 (-0.01)	1.04 (0.02)	1.10 (0.04)	1.17 (0.07)
3.0	0.93 (-0.03)	0.99 (-0.00)	1.04 (0.02)	1.10 (0.04)	1.15 (0.06)
3.5	0.96 (-0.02)	1.01 (0.00)	1.05 (0.02)	1.09 (0.04)	1.14 (0.06)
4.0	0.99 (-0.01)	1.02 (0.01)	1.06 (0.02)	1.09 (0.04)	1.12 (0.05)

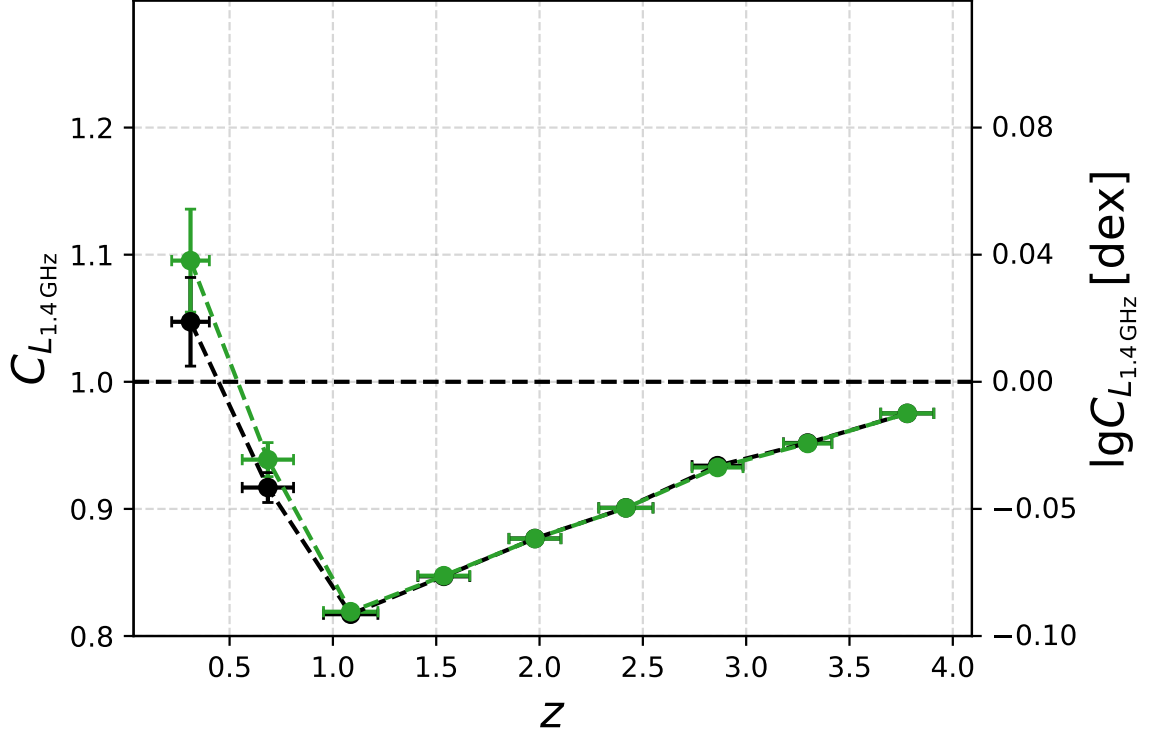


Figure 4.11: Average correction of $L_{1.4 \text{ GHz}}$ for galaxies detected in the radio from the [Delhaize et al. \(2017\)](#) sample. The dashed black line connects corrections in different redshift bins derived by using our broken power-law SED for galaxies with an $\text{SFR} > 10 \text{ M}_{\odot}/\text{yr}$, and an SED based on a 0.97 nonthermal spectral index and a 10% thermal fraction ([Tabatabaei et al. 2017](#)) for NSFGs ($\text{SFR} < 10 \text{ M}_{\odot}/\text{yr}$). The dashed green line similarly connects points based on the broken power-law for an $\text{SFR} > 10 \text{ M}_{\odot}/\text{yr}$ and a simple power-law SED for NSFGs ($\alpha = 0.79$ [Tabatabaei et al. 2017](#)).

Average corrections for selected redshifts and $p_{<10}$ values can be found in Table (4.2). In Fig. (4.11) we calculated average corrections for a subset of galaxies from the ([Delhaize et al. 2017](#)) sample that were detected in the VLA-COSMOS 3 GHz Counterpart catalog ([Smolčič et al. 2017a](#)). The corrections are significant only below $z \sim 1$. The fact that the corrections are not needed for higher redshift bins indicates that the shape of the radio SED cannot explain the $q - z$ relationship.

4.6 Chapter summary

We constructed the average radio spectral energy distribution for a 1.4 GHz-selected sample of highly star-forming galaxies with an $\text{SFR} > 100 \text{ M}_{\odot}/\text{yr}$ in the COSMOS field. To achieve a broad rest-frame frequency range, we combined previously published VLA observations at 1.4 GHz and 3 GHz with unpublished GMRT observations at 325 MHz and 610 MHz by employing survival analysis to account for non-detections in the GMRT maps caused by their higher RMS values. By fitting a broken power-law to the SED, we find the spectral index to change from $\alpha_1 = 0.42 \pm 0.06$ below 4.3 GHz to $\alpha_2 = 0.94 \pm 0.06$ above 4.3 GHz. Our results are in line with previous low-redshift studies of star-forming galaxies with an $\text{SFR} > 10 \text{ M}_{\odot}/\text{yr}$ that show that their SED differs from the one found in normal star-forming galaxies by having a steeper spectral index around 10 GHz, which could imply a smaller thermal fraction than in normal star-forming galaxies.

We further constructed the IR-radio correlation by using our broken power-law SED for galaxies with an $\text{SFR} > 10 \text{ M}_{\odot}/\text{yr}$ and an SED based on a steep nonthermal synchrotron spectral index ($\alpha = 0.97$) and a 10% thermal fraction at 1.4 GHz (Tabatabaei et al. 2017) for galaxies with $\text{SFR} < 10 \text{ M}_{\odot}/\text{yr}$. We find that the shape of the radio-SED is probably not the root cause of the redshift trend found by previous studies, as we see a clear trend of the IR-radio correlation decreasing with increasing redshift also when a more sophisticated K-correction is applied to the data.

Chapter 5

Average radio SED of active galactic nuclei

The analysis and results of this chapter have been submitted to the A&A as Tisanic et al. (subm.).

In recent years, investigation of the radio sky at sub-GHz frequencies has received more attention (see e.g., [Padovani 2016](#)) since the advent of LOFAR, which can operate in the 15 – 200 MHz frequency range ([van Haarlem et al. 2013](#)). Moreover, the Square Kilometer Array (SKA, [Braun 1996](#); [Dewdney et al. 2009](#)) is expected to operate at frequencies from 50 MHz to 20 GHz¹ with nanojansky sensitivities ([Norris et al. 2013](#)), with precursors, like The Murchison Widefield Array Commissioning Survey ([Hurley-Walker et al. 2014](#)) already producing catalogs of sources detected at ~ 100 MHz. Our ability to make predictions of these new instruments is tied to the knowledge of the SED of sources upon which semi-empirical simulations are devised ([Wilman et al. 2008b](#)).

The radio SED of sources in the frequency range of 1 – 10 GHz are often assumed to be described by a simple power-law, with a spectral index of $\alpha = 0.7$ (using the convention $S \sim \nu^{-\alpha}$, [Condon 1992](#)). The simple power-law shape of the radio SED is expected to be mainly due to synchrotron radiation, arising either from supernova remnants, tracing star formation, or from the vicinity of supermassive black holes, tracing AGN activity. However, the radio SEDs have been shown to exhibit deviations from these simple relationships, by having different spectral indices and complex spectral shapes (see, e.g., [Kukula et al. 1998](#); [Kimball & Ivezić 2008](#);

¹<https://www.skatelescope.org/wp-content/uploads/2018/08/16231-factsheet-telescopes-v71.pdf>

Clemens et al. 2008; Leroy et al. 2011; Calistro Rivera et al. 2017; Galvin et al. 2018; Tisanić et al. 2019). For example, quasars have been shown to have spectral indices in the 1 – 10 GHz range that may be either steep (>0.5) or flat (<0.5) (Kukula et al. 1998). At 150 MHz, Toba et al. (2019) find an even greater variety in radio spectral indices, ranging from 0.5 to 2.5.

The shape of the radio SED of individual sources at higher frequencies is related to synchrotron aging process and additionally to free-free emission in star-forming galaxies, while lower-frequency part of the spectrum may be influenced by the different absorption processes (see, e.g., Condon 1992). In bright samples (~ 1 Jy), alongside flat-spectrum sources ($\alpha < 0.5$), a significant fraction (40 – 50%) shows either a steeper SED ($\alpha > 0.5$), or a peaked or inverted spectrum, (Kapahi 1981; Peacock & Wall 1982; De Zotti et al. 2010). Kimball & Ivezić (2008) found that individual SEDs of complex and resolved sources (at a 5 arcsec resolution) are best described by a spectral index of ~ 0.8 , while unresolved sources have a flat spectral shape ($\alpha \sim 0$). They point out that emission from extended radio lobes tends to be steeper, while flatter emission might arise from compact quasar cores/jets due to self-absorbed synchrotron emission. Synchrotron aging is usually described either assuming single injection of electrons with a constant or isotropic pitch angle, or assuming continuous injection of electrons (Kardashev 1962b; Jaffe & Perola 1973; Pacholczyk 1977). Absorption processes affecting the SED shape are synchrotron self-absorption and free-free absorption, which have been used to explain radio spectra of gigahertz peaked-spectrum and compact steep-spectrum sources (O’Dea 1998; Collier et al. 2018). O’Dea & Baum (1997) found that the source size for these types of sources is negatively correlated with turnover frequency in their spectra (Fanti et al. 1990; O’Dea & Baum 1997), while sources have been found with turnover frequencies above 10 GHz (Edge et al. 1998). By using LOFAR observations, Calistro Rivera et al. (2017) find statistically significant steepening in their AGN SED in the 150 MHz – 600 MHz range compared to the AGN SED around 1 GHz.

Previous studies of radio SEDs of individual sources find that the average value of the spectral index is consistent with the expected value of $\alpha = 0.7$ (e.g., Kukula et al. 1998; Toba et al. 2019). Radio luminosity function of AGN has been shown to differ for flat and steep spectrum sources (Dunlop & Peacock 1990). Novak et al. (2018) quantify the impact of different SED shapes

on radio luminosity functions by pointing out that while the differences in individual galaxies' SEDs cancel out for large samples, even a slight change of 0.1 in the mean value of the spectral index could result in a 0.1 dex change in rest-frame luminosities.

In this paper we present a survival analysis study of the average radio SED of a sample of radio-excess AGN in the COSMOS field, identified by an excess in radio luminosity compared to that expected solely from star-forming processes. A combination of radio data available in the COSMOS field offers a way to construct approximately luminosity-complete samples out to $z \sim 4$, farther than would be possible when considering sources individually. We construct average radio SED following prescription by [Tisanić et al. \(2019\)](#).

In Sect. 5.1 we describe the available observations used in constructing the radio SED and the selection of the radio-excess AGN sample. In Sect. 5.2 we briefly summarize the method used to construct the radio SEDs and describe models used to analyze its shape. We use the convention that steeper SED means larger spectral index ($S \sim \nu^{-\alpha}$) throughout this paper and adopt the following cosmological parameters: $\Omega_M = 0.3$, $\Omega_\Lambda = 0.7$, and $H_0 = 70$ km/s/Mpc.

5.1 Sample

To assess the radio SED, we combined catalogs of the radio data in the COSMOS field at four observer-frame frequencies: 325 MHz and 610 MHz, obtained with the GMRT ([Tisanić et al. 2019](#)), and at 1.4 GHz ([Schinnerer et al. 2010](#)) and 3 GHz ([Smolčić et al. 2017b](#)), obtained with the VLA. Here we briefly describe the sample used in this paper (Sect. 5.1.1).

5.1.1 The 1.4 GHz selected sample

In order to obtain at least two data points per source for SED analysis, following [Tisanić et al. \(2019\)](#) we have defined and analyzed a 1.4 GHz-selected sample of sources from the VLA-COSMOS 1.4 GHz Joint Project (hereafter VLA1.4JP, [Schinnerer et al. 2010](#)) catalog that were detected in the VLA-COSMOS 3 GHz Large Project (hereafter VLA3LP, [Smolčić et al. 2017b](#)) counterpart catalog. The 3 GHz data have lower root-mean-square (RMS) ($\sim 2 \mu\text{Jy}/\text{beam}$) than the $\sim 12 \mu\text{Jy}/\text{beam}$ RMS of the 1.4 GHz data. This procedure introduced only minimal potential

biases stemming from the 1.4 to 3 GHz spectral index distribution, as almost all 1.4 GHz sources ($\sim 90\%$, [Smolčić et al. 2017b](#)) have counterparts at 3 GHz.

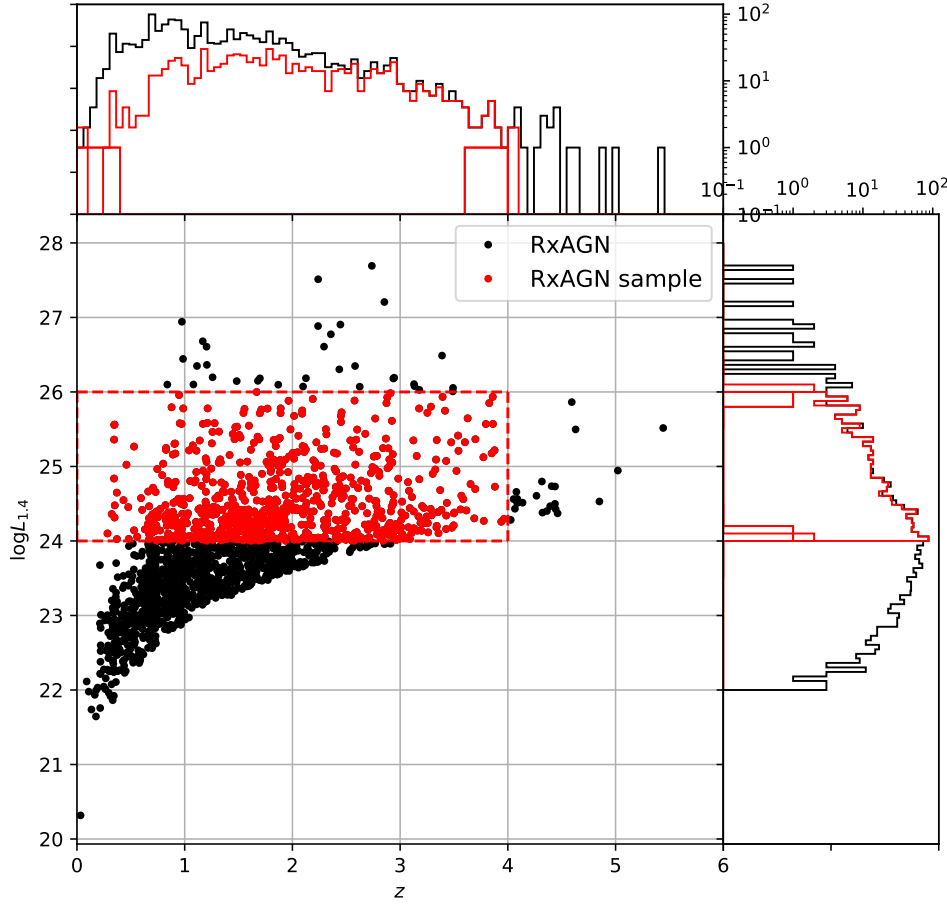


Figure 5.1: Radio luminosity $L_{1.4}$ and redshift for RxAGN (black points). Red points correspond to the selected redshift and radio luminosity sample of RxAGN used in this work and are contained within $\log L_{1.4} \in [24, 26]$ and $z \in [0, 4]$. The histograms show the distribution of radio luminosity and redshift for all RxAGN and the RxAGN sample used in this work with black and red bars, respectively.

[Smolčić et al. \(2017a\)](#) obtained photometric redshifts by cross-correlating the 3 GHz Source Catalog with multi-wavelength counterparts, drawn from three catalogs, resulting in 7729 COSMOS2015 ([Laigle et al. 2016](#)), 97 i-band ([Capak et al. 2007](#)), and 209 IRAC ([Sanders et al. 2007](#)) counterparts to the 8696 3 GHz sources found within the 1.77 deg^2 subarea of the COSMOS field. Spectroscopic redshifts were taken from the COSMOS spectroscopic catalog containing

97102 sources with a counterpart (M. Salvato, priv. comm.). In total, 7778 out of the 8035 sources had determined redshifts, of which 2740 had spectroscopic, and 5123 photometric redshifts. To determine the physical properties of the AGN host galaxies, a three-component SED-fitting procedure (Delvecchio et al. 2017) was applied using all of the available photometry.

As described by Smolčić et al. (2017a), AGN were divided into moderate-to-high radiative luminosity AGN (HLAGN) and low-to-moderate radiative luminosity AGN (MLAGN), which are analogs of high- and low-excitation emission line AGN, respectively. As summarized in Fig. 10 in Smolčić et al. (2017a), HLAGN were identified as either X-ray AGN (i.e. having X-ray luminosity $L_X > 10^{42}$ ergs/s, Szokoly et al. 2004), mid-infrared AGN (using the criteria from Donley et al. 2012), or using optical-to-millimeter SED fitting (Delvecchio et al. 2017). MLAGN were identified by requiring red optical colors $M_{NUV} - M_{r+} > 3.5$ and no Herschel-band detections. The MLAGN class contains both AGN exhibiting an excess in radio luminosity (described below) and quiescent AGN.

Within this dataset, we use a sample of RxAGN. The class of RxAGN is identified by their 3σ radio excess with respect to the value of radio luminosity expected only from contribution from star formation calculated using infrared luminosity (see Smolčić et al. 2017a; Delhaize et al. 2017; Delvecchio et al. 2017). We separate RxAGN into RxQMLAGN, RxSMLAGN, and RxHLAGN, depending on whether they satisfy the MLAGN or HLAGN criteria. We have combined fluxes at 1.4 GHz from the 1.4 GHz-selected sample of RxAGN sources with their corresponding fluxes at 3 GHz. To this dataset, we have added fluxes of corresponding sources in the GMRT catalogs, matched using TOPCAT.

In summary, we have selected a sample of RxAGN in the COSMOS field that appear to be relatively complete in the sense of redshift within $z \in [0, 4]$, and radio luminosity at 1.4 GHz, $\log L_{1.4} \in [24, 26]$, as shown in Fig. 5.1. In Fig. 5.2 we show the mean completeness correction for the sample of RxAGN as a function of redshift. Mean completeness corrections for different redshift bins were computed using the 3 GHz flux densities of sources in the RxAGN sample. The completeness corrections used were interpolated from the completeness correction table of the VLA3LP catalog (see table 2 in Smolčić et al. 2017b). The mean completeness is $\sim 100\%$ up to $z \sim 1$ and decreases at higher redshift, but is higher than $\sim 75\%$ out to redshift $z = 4$. In

total, our sample comprises 744 RxAGN, of which 230 are RxHLAGN, 134 RxQMLAGN and 380 are RxSMLAGN.

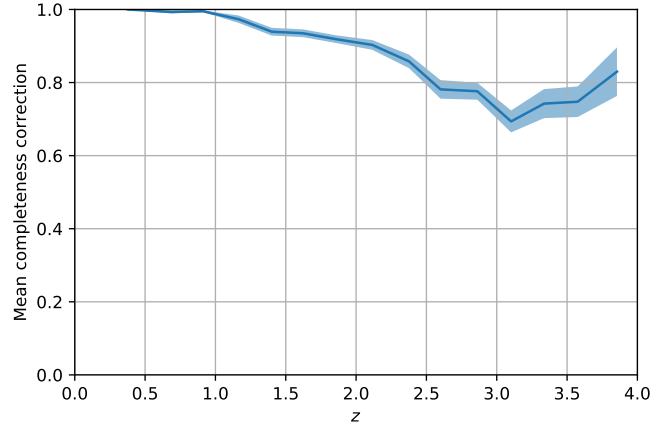


Figure 5.2: Mean completeness correction for the sample of RxAGN as a function of redshift. The mean completeness (solid line), with its corresponding standard deviation (shaded interval), were estimated for different redshift bins using the 3 GHz flux densities and interpolated completeness corrections for the VLA-COSMOS 3 GHz Large Project catalog (table 2 in [Smolčić et al. 2017b](#))

5.2 Methods

We have used the method developed and described in detail by [Tisanić et al. \(2019, see chapter 3\)](#) to derive survival-analysis based estimates of the average radio SED. In Sect. 5.2.1 we give a brief overview of the procedure used to combine the normalized fluxes and normalized upper limits, defined as 5 times the local RMS value at the position of the source, of individual galaxies into a single dataset. In 5.2.2 we give an overview of models used to describe the radio SED.

5.2.1 Construction of average radio SEDs

We present the radio SED as flux vs. frequency in logarithmic space. To achieve uniform frequency binning, we used equally separated bins in log space of the rest-frame frequencies. For each bin, we computed the mean of the log rest-frame frequency and its standard deviation.

We normalized fluxes of both detections and upper limits to a value based on a linear fit to the 1.4 GHz and 3 GHz spectra of individual sources, evaluated at the median rest-frame log-frequency of sources in our sample. If there were no upper limits within the bin, we computed the mean normalized log-flux and its standard deviation for each bin. If there were upper limits within a particular bin, we estimated the mean log-flux and its standard deviation from the constructed best-fitting Weibull model of the survival function to the Kaplan-Meier survival function.

Finally, we fitted a broken power-law (BPL) to the normalized log-flux, $\log F$,

$$\log F \left(\begin{array}{c} \alpha_1 \\ \alpha_2 \\ b \\ \nu_b \end{array} \right) = \begin{cases} -\alpha_2 \log \frac{\nu_r}{\nu_n} + b, & \nu_r > \nu_b, \\ -\alpha_1 \log \frac{\nu_r}{\nu_n} + b + (\alpha_1 - \alpha_2) \log \frac{\nu_b}{\nu_n}, & \nu_r < \nu_b, \end{cases}.$$

described by spectral indices α_1 , below a break frequency ν_b , and α_2 above ν_b , by employing the orthogonal distance regression method bounded within the 2σ confidence interval of parameters, as derived by using the Markov Chain Monte Carlo (MCMC) method. We also discuss the SED shape by employing models of synchrotron self-absorption and synchrotron aging, as outlined below.

5.2.2 Description of synchrotron spectrum

The spectrum of a synchrotron radio source is influenced by synchrotron self-absorption (SSA) and synchrotron aging (SA) processes. Here we briefly describe the influence of both processes on the radio SED.

If the synchrotron emission is described as a power-law with spectral index α , the resulting SSA SED for a homogeneous source has the following shape (constructed using transfer equation and a power-law SED absorption coefficient from [Pacholczyk 1977](#)):

$$F \sim \nu^{5/2} \left(1 - e^{-\left(\frac{\nu}{\nu_1}\right)^{-\alpha-5/2}} \right). \quad (5.1)$$

This model produces a peak around $\nu = \nu_1$ and a simple power-law SED with a spectral index α for $\nu \gg \nu_1$.

If a source is initially described with a spectral index α , the spectrum will deviate from a power-law at later times due to electrons losing energy over time. This produces a spectrum that is steepened by $\Delta\alpha$, a parameter that varies between single injection and continuous injection models, at frequencies higher than the break frequency ν_b (see, e.g., [Condon 1992](#)):

$$F \sim \frac{\nu^{-\alpha}}{1 + \left(\frac{\nu}{\nu_b}\right)^{\Delta\alpha}}. \quad (5.2)$$

We investigate the influence of both effects on the shape of our radio SED by combining the influence of both effects by introducing a fraction of synchrotron-aged flux, f ,

$$F \sim f \frac{\nu^{-\alpha_{SA}}}{1 + \left(\frac{\nu}{\nu_b}\right)^{\Delta\alpha}} + (1 - f) \nu^{5/2} \left(1 - e^{-(\frac{\nu}{\nu_1})^{-\alpha_{SSA}-5/2}}\right). \quad (5.3)$$

This equation reproduces Eq. 5.1 for $\nu \sim \nu_1 \ll \nu_b$, and $f \rightarrow 0$, and Eq. 5.2 for $\nu_1 \ll \nu \sim \nu_b$, and $f \rightarrow 1$. The model presented in Eq. 5.3 is chosen so that it can describe a population of sources that have either a synchrotron aged SED or a synchrotron self-absorbed SED. In this case, the fraction f would represent the fraction of the sample having a synchrotron-aged spectral shape. A further complication to this simple picture would be that a source in the sample has both effects present, but this would greatly increase the number of free parameters.

In contrast to simple models discussed in [Tisanić et al. \(2019\)](#), for which the fitting procedure was developed, model of Eq. 5.3 has multiple break frequencies. It is, therefore, a priori unclear which parameters can be fixed to a particular value. Therefore, to further discuss models of synchrotron self-absorption and aging, we have employed the MBAM in Sect. 5.4.1. The method is summarized in Sect. 5.2.3 and is explained in detail in [Transtrum et al. \(2010\)](#); [Transtrum & Qiu \(2014\)](#).

5.2.3 Manifold Boundary Approximation Method

The radio SED parameters have been estimated using the orthogonal distance regression constrained to the 2σ MCMC-derived confidence intervals. However, this procedure yielded large estimated parameter errors due to the complex shape of the fitting function. Moreover, as in [Tisanić et al. \(2019\)](#), the MCMC estimates are not simple ellipses, which we had solved by fixing

the obvious choice of the greatest uncertainty, the break frequency. Upon applying the same procedure to, e.g., Eq. 5.3, we have found that it is not easy to determine the parameters that has the greatest impact on the derived uncertainties. We have therefore employed the MBAM to determine which of the model parameters contributes to the estimated errors the most (for details, see e.g. [Transtrum et al. 2010](#); [Transtrum & Qiu 2014](#)). The MBAM method solves the geodesic equation in parameter space to determine the least-precise parameter (or combination of parameters). The method consists of computing the Fisher information metric (FIM) from the model parameters (labeled θ^μ) following the [Transtrum & Qiu \(2014\)](#) algorithm, described below.

The method first recognizes that in the space of model residuals of N_d measurements there is an N_d dimensional manifold, \mathcal{R} , with FIM equaling the Euclidean metric,

$$g_{\mathcal{R}} = \sum_{i=1}^{N_d} dr^i \otimes dr^i. \quad (5.4)$$

Each measurement's residual, r^i , is defined as the difference between the data point y^i , with uncertainty σ_i , and particular model's evaluation f^i as $r^i = (y^i - f^i)/\sigma_i$. A particular model's parameters, which we label $\theta^1, \dots, \theta^{N_p}$, constitute an N_p -dimensional manifold, \mathcal{M} . Residuals are therefore an embedding of the model manifold in the residuals' manifold. The metric on \mathcal{M} , g , is therefore computed using the pullback, r^* , as

$$g = r^* g_{\mathcal{R}} = \left(\sum_{i=1}^{N_d} \partial_\mu r^i \partial_\nu r^i \right) d\theta^\mu \otimes d\theta^\nu. \quad (5.5)$$

The geodesic equation in \mathcal{M}

$$\frac{d^2 \theta^\mu}{d\tau^2} + \Gamma^\mu_{\alpha\beta} \frac{d\theta^\alpha}{d\tau} \frac{d\theta^\beta}{d\tau} = 0, \quad (5.6)$$

is then solved as an initial value problem, where $\Gamma^\mu_{\alpha\beta}$ are the Christoffel symbols of the second kind. The initial position is chosen to be the best-fitting parameters $\theta^\mu(\tau = 0) = \theta^\mu_{bf}$. The 'velocity', $d\theta^\mu/d\tau(\tau = 0)$, is chosen to be the eigenvector of the FIM corresponding to the smallest eigenvalue. The components of the eigenvector corresponding to the smallest eigenvalue at a sufficiently large τ are compared to the values at $\tau = 0$.

5.3 Results

We have constrained the shape of the radio-SED of RxAGN and subsets of the RxAGN sample. In Fig. 5.3, we show the mean normalized log-flux and the corresponding standard deviation of the distribution of log-fluxes for each rest-frame frequency bin. Using a simple power-law (PL) model, the RxAGN SED, shown in the left panel of Fig. 5.3, can be described by a spectral index of 0.64 ± 0.07 . However, as can be seen from Fig. 5.3, this model does not describe the dataset well. Therefore, we fitted the BPL model to account for spectral curvature, shown in the right panel of Fig. 5.3. The spectral indices of this model are $\alpha_1 = 0.28 \pm 0.03$, and $\alpha_2 = 1.16 \pm 0.04$, while the break frequency, which in the full model was poorly constrained by $\nu_b = (4.1 \pm 0.2)$ GHz, was fixed to 4 GHz to reduce parameter uncertainties, as described in [Tisanić et al. \(2019\)](#).

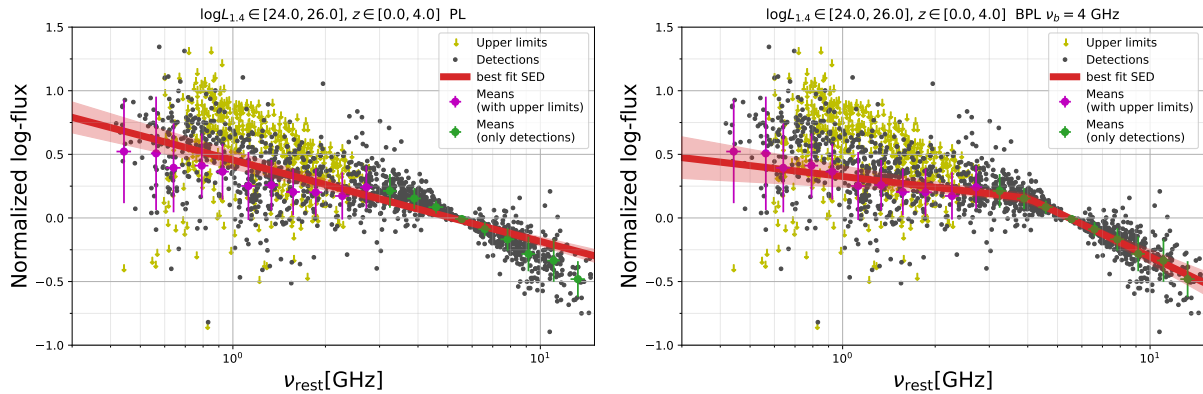


Figure 5.3: The radio SED of RxAGN as normalized log-flux vs. rest-frame frequency for $z \in [0, 4]$ and $\log L_{1.4} \in [24, 26]$. A single power-law (left panel) and a broken power-law (right panel) models of the radio SED are shown as red lines with red confidence intervals. Detections are shown as grey points, upper limits as yellow arrows, bins without upper limits as green points and bins with upper limits as magenta points. The derived power-law spectral index is 0.64 ± 0.07 , while the broken power-law parameters are $\alpha_1 = 0.28 \pm 0.03$, $\alpha_2 = 1.16 \pm 0.04$ and $\nu_b = (4.1 \pm 0.2)$ GHz.

5.4 Discussion

In this section we explore the properties of the derived radio SED of RxAGN. In Sect. 5.4.1, we investigate the cause for the derived SED shape. In Sect. 5.4.2 we analyze possible correlations with redshift of different RxAGN subsamples, source size and further classifications, while in Sect. 5.4.3 we derive the SED for a sub-sample of flat-spectrum sources.

5.4.1 Possible cause of the SED shape

It is clear from Fig. 5.3 that a simple PL model does not describe the SED well. Using the BPL model yields an SED shape with a spectral index difference $\Delta\alpha = \alpha_2 - \alpha_1 = 0.88 \pm 0.05$. This spectral index difference is higher than expected from the simple Kardashev-Perola model of synchrotron aging ($\Delta\alpha = 0.5$, Kardashev 1962b,a). This may indicate that the SEDs of individual sources may be better described by either more complex models of synchrotron aging (Jaffe & Perola 1973; Tribble 2014) or the SED shapes are affected by processes of synchrotron self-absorption or free-free absorption (Menon 1983; Tingay & de Kool 2003; Kamenon et al. 2005).

To investigate how SA and SSA processes could produce the observed SED, we have fitted Eq. 5.3 to the RxAGN dataset. By blindly applying this model, the RxAGN SED is described with the following set of parameters, exhibiting varying degrees of uncertainties, $f = 0.7 \pm 0.3$, $\alpha_{SA} = 0.4 \pm 0.5$, $\alpha_{SSA} = 0.8 \pm 0.6$, $\nu_1 = (1 \pm 2)$ GHz, $\nu_b = (6 \pm 2)$ GHz, $\Delta\alpha = 2 \pm 1$. As can be seen in the upper panel of Fig. 5.4, this model describes the data well, but is not very informative regarding the constraints of the spectral index and the fraction f . We have therefore used the MBAM method to reduce the uncertainties of these parameters, with the resulting SED shown in the lower panel of Fig. 5.4.

We have found that the model is best constrained by setting $\nu_b \rightarrow \infty$, which corresponds to a reduced model described using a synchrotron self-absorbed SED with a spectral index labeled α_{SSA} , and a power-law SED with a spectral index labeled α_{SA} and without any aging break. The thus derived model parameters are $\alpha_{SA} = 0.7 \pm 0.2$, $\alpha_{SSA} = 1.1 \pm 0.5$, $\nu_1 = (3.0 \pm 0.3)$ GHz and $f = 0.8 \pm 0.3$. The details of the applied MBAM procedure can be found in Sect. 5.2.3.

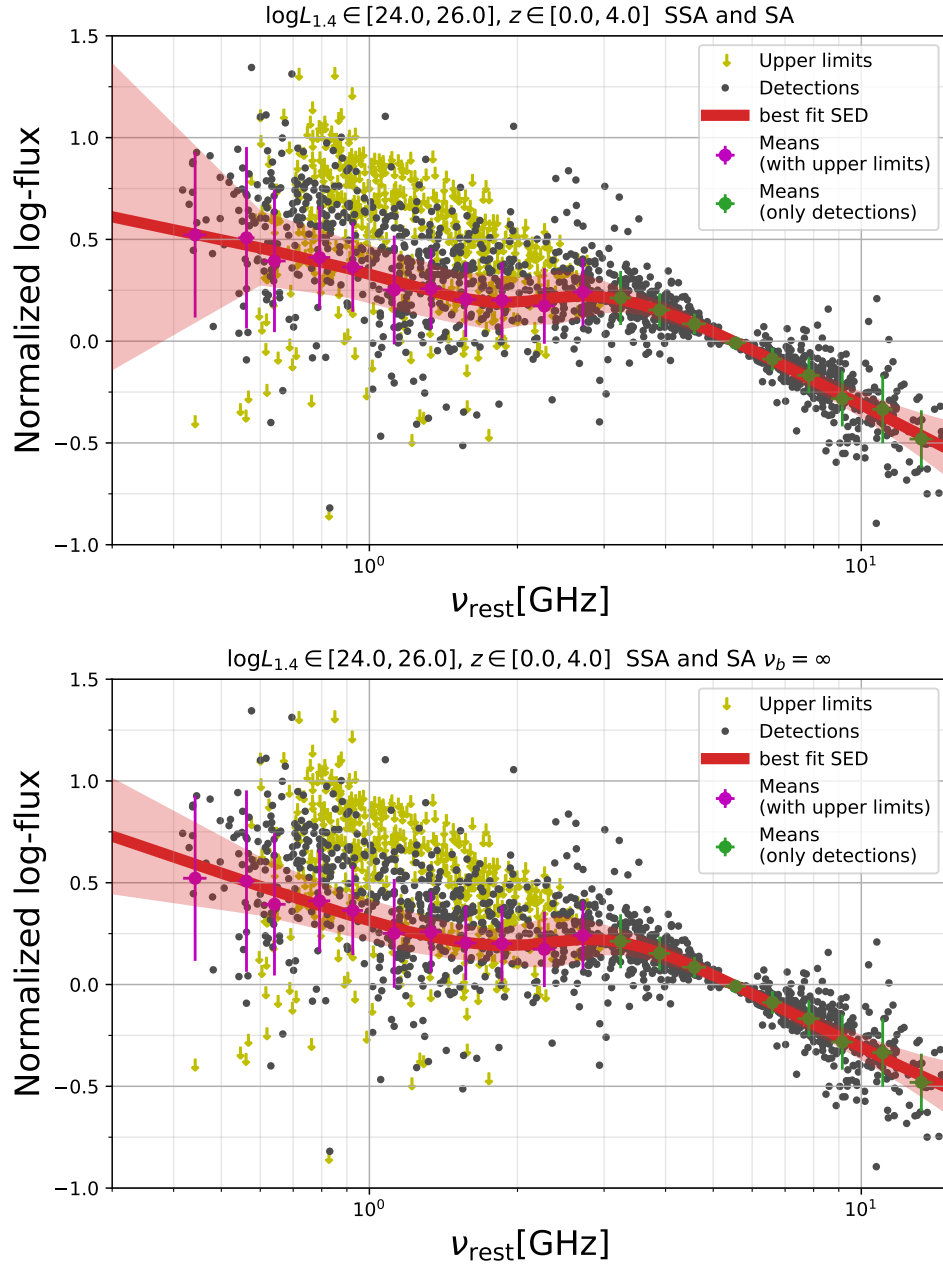


Figure 5.4: SED of the RxAGN sample with the model from Eq. 5.3 fitted. Upper panel shows the resulting model before applying the MBAM method, while the lower panel shows the best-fitting model after reducing the number of parameters with the MBAM method.

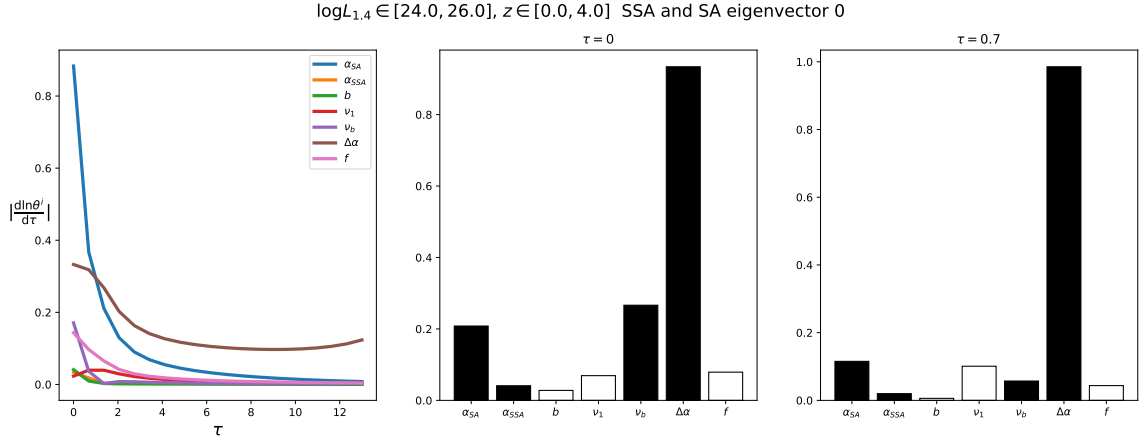


Figure 5.5: Behavior of logarithmic derivative of parameters along the geodesic curve (left panel) and the components of the FIM eigenvector corresponding to the smallest eigenvalue at the beginning (end) of the geodesic curve are shown in the middle (right) panel the model from Eq. 5.3.

In Fig. 5.4, we show that this reduced model describes the same data points with a similar SED shape as the full model. Fig. 5.5 shows the behavior of the components of the eigenvector corresponding to the smallest FIM eigenvalue for the radio SED of RxAGN. In the best fitting point (middle panel of Fig. 5.5), the eigenvector's components are pointing in a direction that doesn't purely indicate the most uncertain parameter. However, along a geodesic, for sufficiently large τ , the movement along a geodesic halts in each direction other than $\Delta\alpha$, as indicated by diminishing values of the logarithmic parameter derivatives in the left panel of Fig. 5.5. The eigenvector corresponding to the smallest FIM eigenvalue, now computed at the end of the geodesic curve, clearly shows that the least determined parameter is $\Delta\alpha$. Moreover, as indicated by the blue line in the left panel of Fig. 5.5, the geodesic curve significantly varies only in the $\Delta\alpha$ direction, pointing toward $\Delta\alpha \rightarrow \infty$. In the upper panel of Fig. 5.4, we have over-plotted the SED resulting at the end of the computed geodesic with black dashed line. This line does not exit the 1σ confidence interval, further indicating we can safely eliminate $\Delta\alpha$ by setting $\Delta\alpha \rightarrow \infty$. This reduced model also reduces the need for v_b .

The resulting SED shows a 'bump' at ~ 3 GHz and a low frequency steepening around 0.6 – 1 GHz. For sources detected at both GMRT and VLA frequencies, there seems to be a

deficit in flux computed at 610 MHz based on the VLA fluxes. This correction is appropriate for some of the sources, while blindly applying a 20% correction of the total flux induced overcorrection in others. The flux offset is different when computed based on the 1.4 GHz catalog and when computed using the 3 GHz catalog, indicating complications due to complex spectral shapes. Since this frequency range is dominated by the 610 MHz GMRT catalog fluxes, to account for possible biases in the fluxes at this frequency, we have performed again the SED fitting procedure without the 610 MHz catalog. We find a similar steepening in the SED when using only the 325 MHz, 1.4 GHz and 3 GHz data, indicating that the effect may be due to the intrinsic shape of the SED and not due to systematic effects of a particular catalog. Alternatively, this result could explain [Calistro Rivera et al. \(2017\)](#) findings, since the observed feature in our SED effectively produces a steeper spectrum below 1 GHz with a flattening around 1 GHz. Moreover, the fraction of SSA emission ($1 - f = 0.2 \pm 0.03$) described by a steep SSA spectral index is in line with [Kapahi \(1981\)](#) and [Peacock & Wall \(1982\)](#), suggesting the presence of gigahertz-peaked or inverted spectrum sources in our sample.

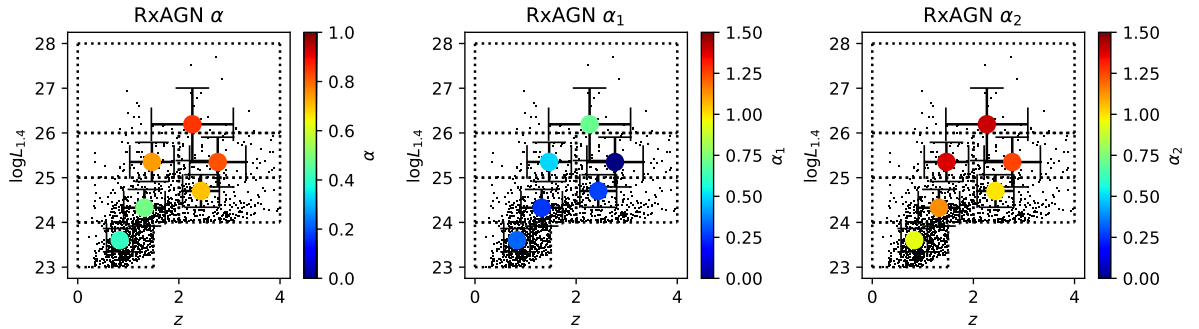


Figure 5.6: Spectral indices derived for subsets of the RxAGN sample divided by redshift, z , and radio luminosity, $\log L_{1.4\text{GHz}}$, described in Sect. 5.4.2. The color-scale in the left panel shows the spectral index of the PL model, while the color-scales in the middle and right panels show the spectral indices α_1 and α_2 of the broken power-law model. Bins are outlined by black dashed lines.

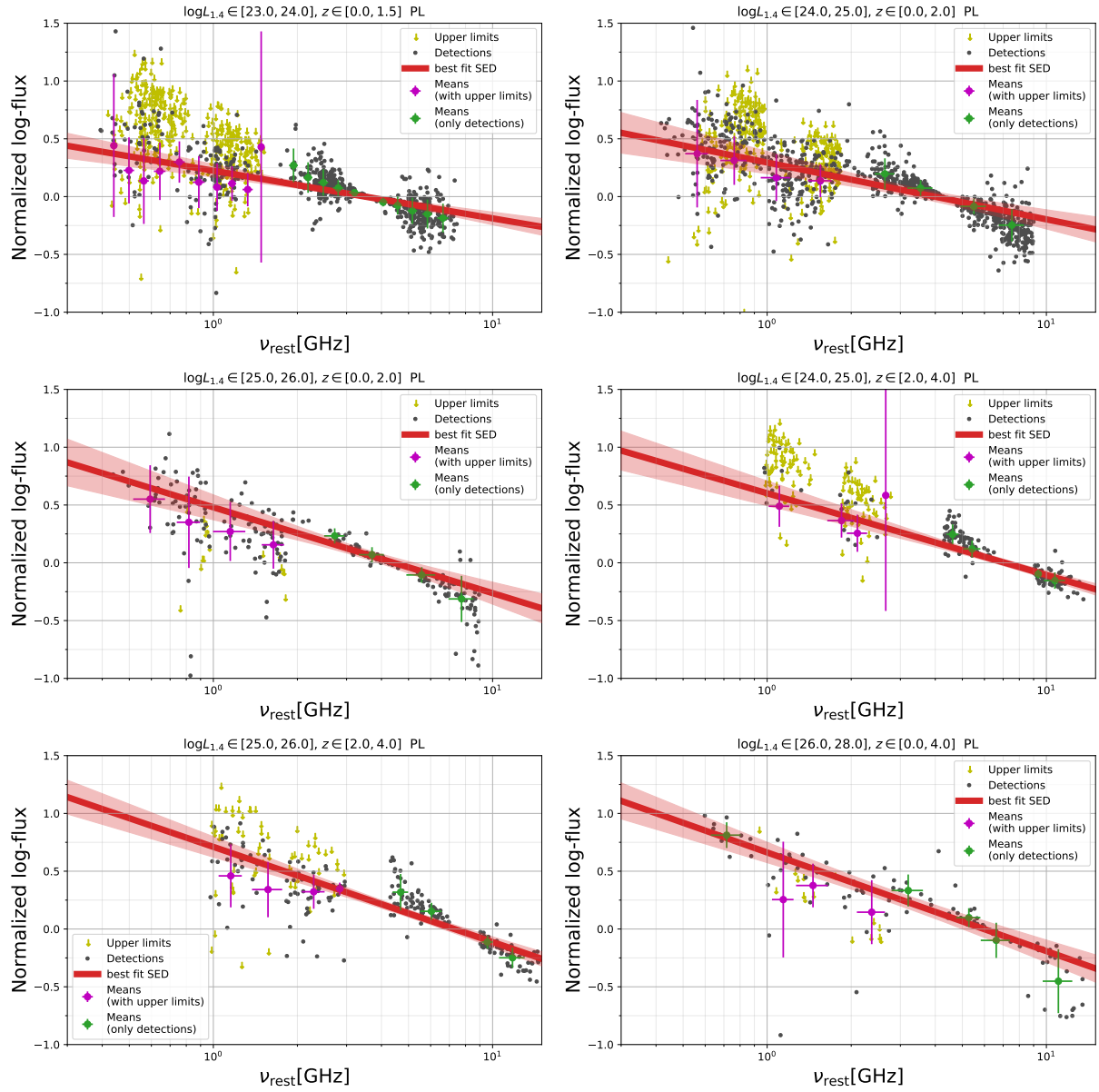


Figure 5.7: SEDs derived for subsets of the RxAGN sample divided by redshift, z , and radio luminosity, $\log L_{1.4\text{GHz}}$. Shown is the best-fitting power-law model for each bin.

5.4.2 SED shape dependence on various observables

In order to test if the shape of the radio SED of RxAGN depends on parameters like redshift and radio luminosity, we split the RxAGN dataset in bins of redshift and 1.4 GHz radio luminosity and fitted both the PL and the BPL models to each bin separately.

The best-fitting PL spectral indices are shown for each selected bin in Fig. 5.6 for the whole RxAGN dataset and the corresponding SEDs are shown in Fig. 5.7. The bins, whose boundaries are outlined by black dashed lines in Fig. 5.6, split the RxAGN sample into four bins and additionally include two bins, for lower and higher 1.4 GHz radio luminosities. All bins have the mean completeness correction higher than 75%.

We have further used source sizes of RxAGN (Bondi et al. 2018) to investigate whether there is a correlation of spectral indices with the source size, D , or the type of the source (RxHLAGN, RxSMLAGN, RxQMLAGN) in different bins.

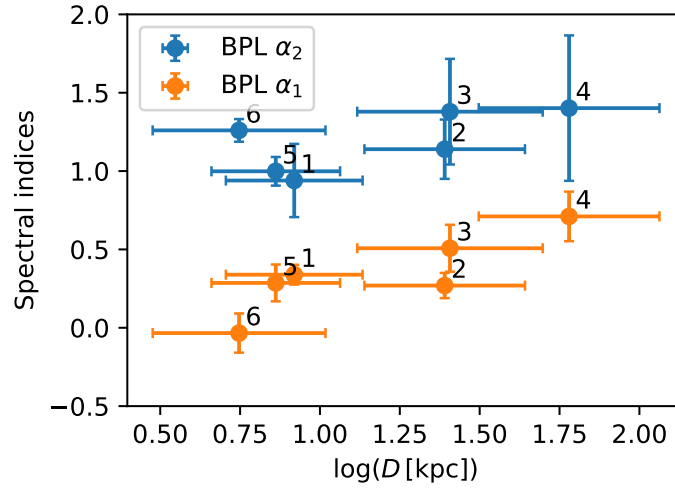


Figure 5.8: Dependence of the broken power-law spectral indices below and above a break frequency of 4 GHz (α_1 and α_2 , respectively) on the source size, $\log D$, for the subsets of the RxAGN dataset for different values of $\log D$, with corresponding errors in spectral indices. The error bars for $\log D$ show the standard deviations of $\log D$ within each bin. The numbers indicate the bin number in table 5.2.

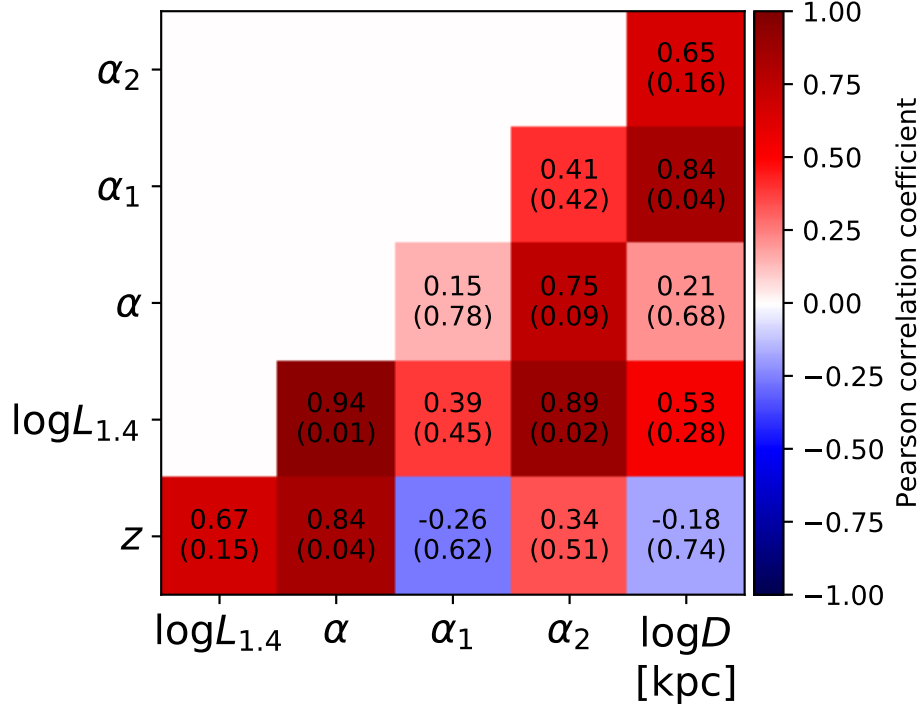


Figure 5.9: Correlation matrix for properties of subsets of the RxAGN sample. Colors indicate positive or negative Pearson correlation coefficient, written on the plot for each parameter pair with its corresponding p-value in parentheses. The considered variables in the correlation matrix are the 1.4 GHz radio luminosity, $\log L_{1.4}$, power-law spectral index α , broken power-law spectral indices α_1 and α_2 , and source size, $\log D$.

To this end, we further split the dataset in mutually independent subsets of RxHLAGN, RxQMLAGN and RxSMLAGN (see Sect. 5.1.1 for details). In Fig. 5.8 we show the dependence of the BPL spectral indices on source size for subsets of the RxAGN dataset binned in redshift and 1.4 GHz radio luminosity. In Fig. 5.9, we show the components of the correlation matrix with given p-values of correlation coefficients. If we adopt a p-value cut, $P < 0.1$, this correlation matrix shows the following:

1. There a positive correlation of the PL spectral index α with both redshift and radio luminosity;
2. There is a positive correlation of the BPL spectral index α_1 with source size;

3. There is a positive correlation of the BPL spectral index α_2 with source size, radio luminosity and the PL spectral index α .

Since some of the parameters (z , $\log L_{1.4}$, $\log D$) are likely to be mutually correlated, we have employed a series of Analysis of variance (ANOVA) and linear model tests using the `STATSMODELS` package (Seabold & Perktold 2010) to further analyze the spectral indices and their correlations with other parameters. We performed ANOVA analysis of the different spectral indices α , α_1 and α_2 to determine if there was a difference between subsets of RxHLAGN, RxQMLAGN, RxSMLAGN and possibly with redshift and source size. We started by considering the following dependent variables: type (RxHLAGN, RxQMLAGN, RxSMLAGN) as a categorical variable, redshift and source size. For PL and BPL spectral indices, we separately performed a linear model fit of the spectral indices as functions of all dependent variables. We then computed the F-statistics and the corresponding p-values for each parameter in the model. The parameter with the highest p-value was removed from the model until all variables in the reduced model had p-values less than 10%.

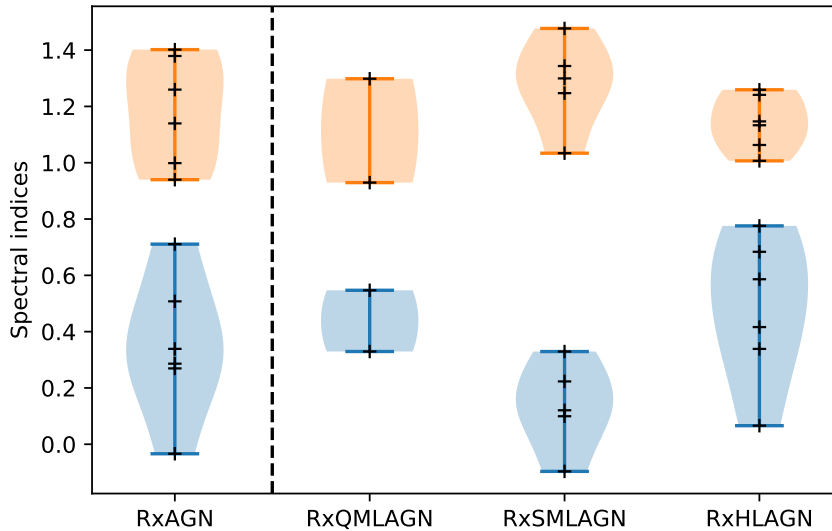


Figure 5.10: Distribution of the broken power-law spectral indices for the subsets of the RxAGN sample. Black crosses are spectral indices derived for individual bins, listed in Tab. 5.2. Blue intervals denote α_1 while orange intervals denote α_2 .

Table 5.1: Summary of ANOVA results for the power-law and broken power-law spectral indices for RxAGN subsamples. For each model the significance of dependence of the spectral index on each of the listed parameters is determined from the p-value and the F-statistic. The considered parameters are: Type- if the sources in the bins were RxHLAGN, RxSMLAGN or RxQMLAGN, z - redshift, and $\log D$ - source size.

Model	Parameter	F-statistic	p-value
$\alpha(\text{Type}, z, \log D)$	Type	1.65	0.23
	$\log D$	17.08	0.001
	z	68.21	0.000002
$\alpha(\text{Type}, \log D)$	Type	0.54	0.66
	$\log D$	0.89	0.36
$\alpha(z, \log D)$	z	64.79	5.1×10^{-7}
	$\log D$	16.71	8.6×10^{-4}
$\alpha(\text{Type})$	Type	0.43	0.73
$\alpha_1(\text{Type}, z, \log D)$	Type	2.45	0.11
	$\log D$	8.9	0.01
	z	0.63	0.44
$\alpha_1(\text{Type}, \log D)$	Type	2.89	0.07
	$\log D$	10.89	0.005
$\alpha_1(z, \log D)$	z	1.37	0.26
	$\log D$	7.18	0.02
$\alpha_1(\text{Type})$	Type	2.22	0.13
$\alpha_2(\text{Type}, z, \log D)$	Type	1.33	0.31
	$\log D$	22.77	0.0004
	z	9.80	0.008
$\alpha_2(\text{Type}, \log D)$	Type	2.21	0.13
	$\log D$	10.62	0.005
$\alpha_2(z, \log D)$	z	0.17	0.001
	$\log D$	20.60	0.0003
$\alpha_2(\text{Type})$	Type	0.81	0.50

Table 5.2: Parameters of the power-law and broken power-law models, and source size, $\log D$, derived for subsets of the RxAGN sample divided by redshift, z , and radio luminosity, $\log L_{1.4 \text{ GHz}}$, described by the mean and standard deviation of redshifts and radio luminosity for each bin. The sample is further split into RxHLAGN, RxQMLAGN, and RxSMLAGN. The numbers 1-6 in parentheses indicate bin labels in Fig. 5.8.

z	$\log L_{1.4}$	Type	α	α_1	α_2	$\log D$
0.83 ± 0.26	23.60 ± 0.28	RxAGN (1)	0.41 ± 0.06	0.34 ± 0.06	0.94 ± 0.23	0.92 ± 0.21
1.3 ± 0.4	24.33 ± 0.24	RxAGN (2)	0.49 ± 0.10	0.27 ± 0.08	1.14 ± 0.19	1.39 ± 0.25
1.5 ± 0.4	25.35 ± 0.26	RxAGN (3)	0.74 ± 0.13	0.51 ± 0.15	1.38 ± 0.34	1.41 ± 0.29
2.3 ± 0.8	26.2 ± 0.4	RxAGN (4)	0.85 ± 0.11	0.71 ± 0.16	1.4 ± 0.5	1.78 ± 0.28
2.4 ± 0.4	24.70 ± 0.21	RxAGN (5)	0.71 ± 0.09	0.29 ± 0.12	1.00 ± 0.09	0.86 ± 0.20
2.8 ± 0.6	25.35 ± 0.28	RxAGN (6)	0.82 ± 0.10	-0.03 ± 0.13	1.26 ± 0.07	0.75 ± 0.27
1.0 ± 0.4	24.29 ± 0.25	RxQMLAGN	0.50 ± 0.09	0.33 ± 0.10	0.93 ± 0.22	1.12 ± 0.27
1.2 ± 0.4	25.28 ± 0.22	RxQMLAGN	0.75 ± 0.11	0.55 ± 0.16	1.3 ± 0.4	1.13 ± 0.31
1.5 ± 0.4	24.34 ± 0.24	RxSMLAGN	0.56 ± 0.11	0.33 ± 0.11	1.25 ± 0.27	1.40 ± 0.24
1.77 ± 0.30	25.27 ± 0.29	RxSMLAGN	0.79 ± 0.10	0.22 ± 0.10	1.34 ± 0.10	1.54 ± 0.30
2.6 ± 0.6	26.1 ± 0.4	RxSMLAGN	0.82 ± 0.17	0.1 ± 0.4	1.48 ± 0.35	1.19 ± 0.30
2.46 ± 0.34	24.71 ± 0.21	RxSMLAGN	0.72 ± 0.12	0.10 ± 0.12	1.03 ± 0.07	0.86 ± 0.20
2.7 ± 0.6	25.32 ± 0.26	RxSMLAGN	0.79 ± 0.12	-0.10 ± 0.15	1.30 ± 0.10	1.06 ± 0.27
0.82 ± 0.25	23.69 ± 0.27	RxHLAGN	0.50 ± 0.07	0.42 ± 0.08	1.01 ± 0.28	1.11 ± 0.23
1.3 ± 0.4	24.35 ± 0.24	RxHLAGN	0.55 ± 0.10	0.34 ± 0.06	1.15 ± 0.14	1.89 ± 0.27
1.4 ± 0.5	25.37 ± 0.25	RxHLAGN	0.78 ± 0.07	0.68 ± 0.08	1.13 ± 0.23	1.30 ± 0.30
2.2 ± 0.8	26.2 ± 0.5	RxHLAGN	0.89 ± 0.08	0.78 ± 0.11	1.24 ± 0.27	1.54 ± 0.29
2.4 ± 0.4	24.68 ± 0.16	RxHLAGN	0.89 ± 0.07	0.59 ± 0.10	1.06 ± 0.07	0.78 ± 0.21
2.9 ± 0.6	25.39 ± 0.30	RxHLAGN	0.85 ± 0.09	0.07 ± 0.13	1.26 ± 0.07	0.60 ± 0.28

The ANOVA results are shown in Table 5.1. In Table 5.2 we show the determined spectral indices for various bins, while in Fig. 5.10 we show the distribution of the BPL spectral indices for the different subsets. We find that the variations in the PL spectral index can be explained by just redshift and source size, the BPL spectral index α_1 can be described using type and source size, while α_2 can be described using source size and redshift. The parameters of the

corresponding linear models are

$$\begin{aligned}\alpha &= 0.17 \pm 0.07 + (0.10 \pm 0.02) \log D + (0.20 \pm 0.02)z \\ \alpha_1 &= 0.0 \pm 0.1 + (0.2 \pm 0.06) \log D + (0.1 \pm 0.1)\text{RxHLAGN} \\ &\quad + (0 \pm 0.1)\text{RxQMLAGN} + (-0.2 \pm 0.1)\text{RxSMLAGN} \\ \alpha_2 &= 0.7 \pm 0.1 + (0.16 \pm 0.04) \log D + (0.15 \pm 0.04)z\end{aligned}$$

where types are taken as categorical variables (1 or 0).

All spectral indices show a rising trend with source size, which would imply that the SEDs of larger sources are more influenced by larger-scale features (jets). [Blundell et al. \(1999\)](#) argue that sources at higher redshift are on average younger than sources at lower redshift and thus have interactions of their jets occurring closer to the host galaxy. This could explain the trend of rising PL spectral index α , and BPL spectral index α_2 with both redshift and source size. [Ker et al. \(2012\)](#) find that the strongest correlation is between spectral index and source size, with redshift correlation becoming more important around ~ 1 GHz. This might explain the ANOVA giving higher importance to redshift dependence for higher frequency BPL spectral index (α_2) than for α_1 and why both PL and BPL spectral indices depend on source size. All spectral indices show strong ($4 - 5\sigma$) positive correlation with redshift. Furthermore, only the spectral index below 4 GHz shows (weak) correlation with the type of source. The ANOVA test suggests that the variation of the spectral index α_1 between the subsets, as shown in Fig. 5.10, can be in part explained by the source type, but the exact contribution of this effect cannot be reliably determined by fitting, as indicated by large parameter errors. The spectral index α_1 shows a (1σ) positive correlation with RxHLAGN, a negative (2σ) correlation with RxSMLAGN and no correlation with RxQMLAGN.

For a source of a 10 kpc size, these correlations would imply a broken power-law SED described by a spectral index of 0.9 ± 0.2 above 4 GHz and a spectral index $(0 - 0.3) \pm 0.1$ below 4 GHz, with the higher value estimated for RxHLAGN and the lower value estimated for RxSMLAGN. As a consistency check, if we approximate our RxAGN sample as having $z \sim 2$, we are in agreement with our parameters of α_1 and α_2 for the average radio SED of RxAGN, reported in Sect. 5.3.

The positive correlation of spectral indices with source size may be explained by the size-turnover frequency relation for gigahertz-peaked sources (Oriente & Dallacasa 2014). Smaller source size (< 1 kpc) implies a high turnover frequency, thereby producing smaller α_1 values in an averaged sample. The higher-frequency spectral index could also be affected by this relation, since the spectral peak could be broadened, producing a flatter SED (O’Dea et al. 1991). The redshift dependence could be related to the difference in luminosity functions of flat and steep spectrum sources (Jarvis & Rawlings 2002). Regarding the classification as RxHLAGN and RxQMLAGN, the RxHLAGN could have a marginally higher (i.e. by 0.1) spectral index α_1 , but the uncertainties in the $\alpha_1 - RxHLAGN - RxQMLAGN$ relation are too high to draw a definitive conclusion.

5.4.3 Flat spectrum sources

In order to investigate the possibilities that there might be sources in our sample that are severely influenced by SSA, we split our sample by selecting all sources having source sizes less than 1 kpc. This size is expected for gigahertz-peaked sources (O’Dea 1998; Collier et al. 2018). From the turnover frequency-linear size relation (Oriente & Dallacasa 2014) we expect that this requirement should select sources having turnover frequencies above 1 GHz. The constraint on source size less than 1 kpc produces a sample of 25 sources, for which we construct a PL and BPL SED.

The PL model yields an SED with a spectral index of $\alpha = 0.41 \pm 0.07$, while the BPL model describes the spectrum with a spectral index of $\alpha_1 = 0.1 \pm 0.1$ below $\nu_b = (2.7 \pm 0.5)$ GHz and $\alpha_2 = 0.55 \pm 0.09$ above ν_b . The resulting SED is shown in Fig. 5.11. Both the PL and the BPL spectral indices classify our sample below 1 kpc as having a flat spectrum by the usually accepted $\alpha < 0.5$ criterion (see, e.g., De Zotti et al. 2010). Since the break frequency is larger than 1 GHz, the < 1 kpc sample does not show a significant contribution of compact steep-spectrum sources (a spectral index of ~ 0.75 above a turnover frequency of 0.5 GHz, Kapahi 1981; Peacock & Wall 1982; O’Dea 1998; De Zotti et al. 2010).

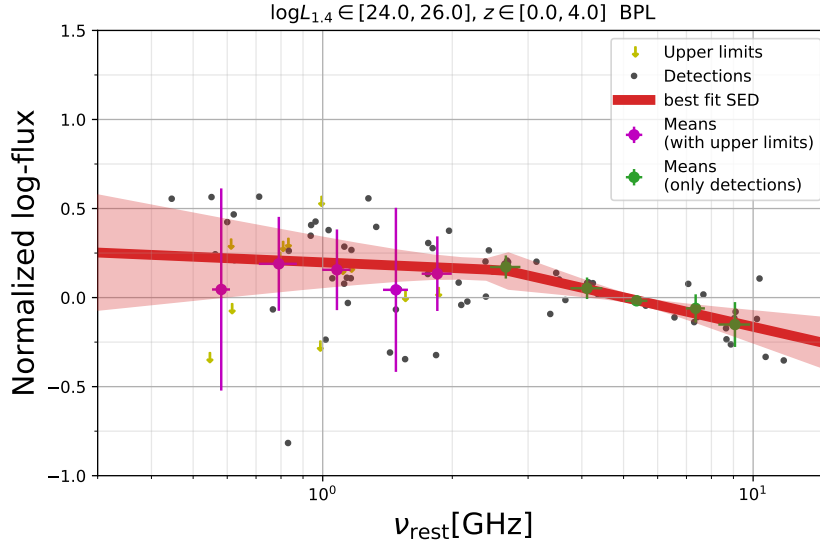


Figure 5.11: SED of a sample of flat-spectrum sources, produced by selecting all sources having sizes less than 1 kpc. Red line shows the broken power-law model.

We find a spectral index difference of $\Delta\alpha = \alpha_2 - \alpha_1 = 0.45 \pm 0.1$, which is less than the theoretical limit imposed by pure synchrotron self-absorption (Mhaskey et al. 2019). This indicates that other absorption processes may also influence the flat spectrum radio SED, like free-free absorption (Kameno et al. 2005; Tingay & de Kool 2003). We have performed a fit of the SSA model on the < 1 kpc sample, yielding a flat spectral index of $\alpha_{SSA} = 0.53 \pm 0.06$ above a break frequency of $\nu_1 = (0.9 \pm 0.1)$ GHz. A broader rest-frame frequency range is needed to determine if this is due to a single SSA component, or a result of multiple break frequencies (Kellermann & Pauliny-Toth 1969; Cotton et al. 1980).

5.5 Chapter summary

We have constrained the radio SED for a sample of AGN in the COSMOS field using available VLA and GMRT data in the rest-frame frequency range from ~ 0.3 GHz to ~ 10 GHz. The radio-excess AGN (RxAGN) sample contained sources which exhibit a 3σ excess of 1.4 GHz radio luminosity, compared to that expected solely from star-forming processes occurring within the AGN host galaxies. The RxAGN sample is relatively complete (75%) in redshift out to $z \sim 4$

and in radio luminosity range from 10^{24} W/Hz to 10^{26} W/Hz.

We find that if we fit the radio SED for this sample with a single power-law model, the resulting spectral index is 0.64 ± 0.07 . However, such a model does not capture all the features of the RxAGN radio SED which can be better described by a broken power-law with a spectral index of $\alpha_1 = 0.28 \pm 0.03$, below 4 GHz, and $\alpha_2 = 1.16 \pm 0.04$, above 4 GHz. The derived SED can be even better described by models involving both synchrotron self-absorption and synchrotron aging processes.

By binning in both the 1.4 GHz radio luminosity and redshift, we have found using ANOVA that the power-law spectral index may rise with increasing source size and redshift. The broken power-law spectral index below 4 GHz depends on source size and the spectral index above 4 GHz depends on both source size and redshift. For a subsample of sources having sizes less than 1 kpc, we find a flat spectrum SED described by a power-law spectral index of $\alpha = 0.41 \pm 0.07$. Using the broken power-law model we find a flat spectrum SED with a spectral index of $\alpha_1 = 0.1 \pm 0.1$ ($\alpha_2 = 0.55 \pm 0.09$) below (above) $\nu_b = (2.7 \pm 0.5)$ GHz.

Chapter 6

Redshift dependence of the infrared-radio correlation

The results of this chapter are a part of a still-ongoing analysis.

Radio and infrared emission of galaxies have been found to be strongly correlated over many orders of magnitude in radio and infrared luminosity ([van der Kruit 1971](#); [Dickey & Salpeter 1984](#); [de Jong et al. 1985](#); [Helou et al. 1985](#); [Sanders & Mirabel 1985](#); [Hummel 1986](#); [Wunderlich et al. 1987](#); [Fabbiano et al. 1988](#)).

The infrared-radio correlation is defined by the q parameter, with various possible frequencies used for infrared and radio luminosities. Throughout this chapter, we use the following convention

$$q = \log L_{TIR}/3.75 \text{ THz} - \log(L_{1.4 \text{ GHz}}), \quad (6.1)$$

where L_{TIR} is the total infrared luminosity ($8 - 1000 \mu\text{m}$) in units of W and $L_{1.4 \text{ GHz}}$ is the luminosity density at 1.4 GHz in units of W/Hz. A frequency of 3.75 THz is used to obtain a dimensionless quantity ([Helou et al. 1985](#)). The thus defined q parameter has been determined for star-forming galaxies in the local universe to be $q = 2.34 \pm 0.01$ out to $z \sim 0.15$, with a dispersion of 0.26 ([Yun et al. 2001](#)).

In the simple calorimeter model ([Voelk 1989](#)), q is expected to be constant over a wide range of magnetic field strengths, which is accomplished by requiring a constant ratio of photon and magnetic-field energy densities. Theoretical considerations ([Murphy 2009](#)) predict q to

increase with redshift, mostly because of the synchrotron electrons' inverse Compton scattering off cosmic microwave background photons.

However, recent studies using stacking and survival analysis find q to be decreasing with increasing redshift (Iverson et al. 2010; Magnelli et al. 2015; Delhaize et al. 2017; Calistro Rivera et al. 2017), a behavior often described as a power law in $(1+z)^n$ with n ranging from -0.1 to -0.3 . Delhaize et al. (2017) pointed out that the computation of rest-frame radio luminosity via a K-correction using only a simple, single power-law assumption of the star-forming galaxies' spectral energy distribution (SED) might cause such a trend, but that does not appear to be the case (Tisanić et al. 2019), nor does simple dependence of the spectral index on redshift explain the redshift trend (Magnelli et al. 2015).

6.1 Methods

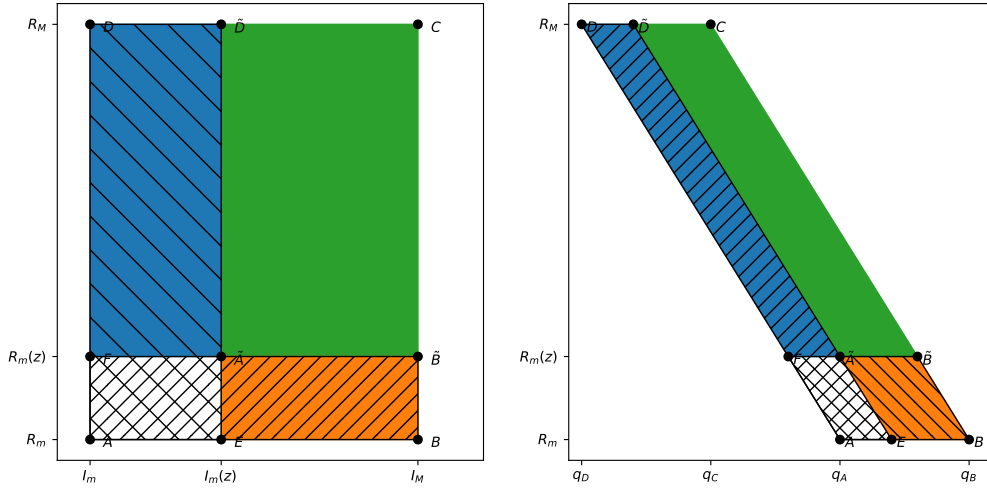


Figure 6.1: Schematic representation of infrared (I) and radio (R) log-luminosity parameter space (left panel) and its mapping to the q - R space (right panel). Green region denotes detections, while blue and orange regions denote regions with non-detections.

We model the distributions of infrared and radio luminosities at each redshift using the

Novak et al. (2018) radio luminosity function for star-forming galaxies, ϕ_R , and the Gruppioni et al. (2013) infrared luminosity functions, ϕ_I .

Radio and infrared luminosity functions are marginals of the joint distribution of sources in radio and infrared luminosity space for each redshift. For a luminosity function $\phi(\log L, z)$, we model its corresponding fixed-redshift probability distribution, p , as

$$p(\log L) = \frac{\phi(\log L, z)}{\int_{L_{min}}^{L_{max}} \phi(\log L, z) d \log L}. \quad (6.2)$$

We do expect these distributions to be dependent due to the existence of a tight infrared-radio correlation. To estimate this joint radio and infrared luminosity distribution, $p(\log L_{1.4 \text{ GHz}}, \log L_{TIR})$, we use statistical copula method

$$p \begin{pmatrix} R \\ I \end{pmatrix} = c_\rho \begin{pmatrix} \Phi^{-1}(P_R(R)) \\ \Phi^{-1}(P_I(I)) \end{pmatrix} p_R(R) p_I(I), \quad (6.3)$$

where P_R , and P_I are corresponding cumulative distribution functions of p_R and p_I , Φ is the cumulative distribution function of the normal distribution, and where we have shortened $\log L_{1.4 \text{ GHz}}$ to R and $\log L_{TIR}$ to I . We chose the Gaussian copula density, defined by

$$c_\rho \begin{pmatrix} x \\ y \end{pmatrix} = \frac{e^{\frac{\rho^2(x^2+y^2)-2\rho xy}{2(1-\rho^2)}}}{\sqrt{1-\rho^2}}. \quad (6.4)$$

Once the joint distribution of Eq. 6.3 is known, we transform our joint probability distribution from luminosities to q using the transformation

$$\phi \begin{pmatrix} q \\ R \end{pmatrix} = \begin{pmatrix} I(q, R) \\ R(q, R) \end{pmatrix} = \begin{pmatrix} q + c + R \\ R \end{pmatrix}, \quad (6.5)$$

where c is the dimensionality factor from Eq. 6.1. The probability distribution in $q - R$ space is then given by

$$p(q, R) dq \wedge dR = \phi^*(p(I, R) dI \wedge dR). \quad (6.6)$$

This transformation is shown schematically in Fig. 6.1. In this figure, infrared (radio) luminosity functions span a range from I_m (R_m) to I_M (R_M), which are mapped to four points in the right

panel of Fig. 6.1: (q_D, R_M) , (q_C, R_M) , (q_A, R_m) and (q_B, R_m) for $z = 0$. The values I_M and R_M are chosen for convergence of numerical integration and are chosen to be sufficiently high so that the probability for having sources with higher luminosities is negligible. At higher redshifts, points I_m and R_m are moved to higher values $I_m(z) > I_m$ and $R_m(z) > R_m$, which correspond to the 5σ upper limits of the surveys, which effectively ‘screen’ a portion of the $q - z$ distribution. While this shifting toward higher values seems trivial in the left panel of Fig. 6.1, we see that the impact is not trivial to describe in the right panel. The information in the white parallelogram is effectively lost if we use a sample of galaxies defined at radio and/or infrared frequencies. We are left only with detections (shown in green in Fig. 6.1) and q -upper limits (blue region) and q -lower limits (orange region).

The resulting distribution of detections is a simple integral

$$p_D(q) \propto \theta(q - q_{\bar{D}})\theta(q_C - q) \int_{R_m(z)}^{R_M} p(q + c + R, R) dR \quad (6.7)$$

$$+ \theta(q - q_C)\theta(q_{\bar{A}} - q) \int_{R_m(z)}^{R_M} p(q + c + R, R) dR \quad (6.8)$$

$$+ \theta(q - q_{\bar{A}})\theta(q_B - q) \int_{R_m(z)}^{R_M} p(q + c + R, R) dR. \quad (6.9)$$

Survival analysis is modeled by integrating the blue and orange regions

$$p_U(q) \propto \theta(q - q_{\bar{D}})\theta(q_{\bar{A}} - q) \int_{I_m}^{I_m(z)} p(I, I_m(z) - c - q) dI \quad (6.10)$$

$$p_L(q) \propto \theta(q - q_{\bar{A}})\theta(q_{\bar{B}} - q) \int_{R_m}^{R_m(z)} p(R + c + R_m(z), R) dR. \quad (6.11)$$

We obtain the probability density function, $p_{SA}(q)$, using the survival analysis method proposed by [Schmitt \(1985\)](#).

Parameters of the distribution can then be determined by either computing the mean

$$\langle q \rangle = \frac{\int_{q_{min}}^{\infty} q p_{SA}(q) dq}{\int_{q_{min}}^{\infty} p_{SA}(q) dq}, \quad (6.12)$$

or by fitting a Gaussian distribution to $p_{SA}(q)$.

6.2 Results

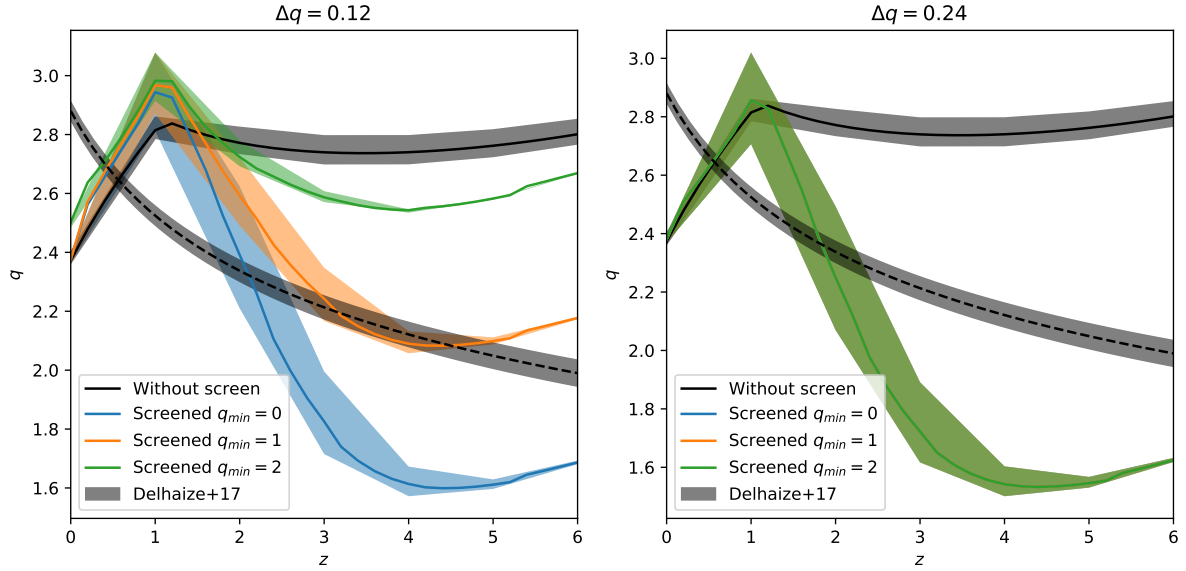


Figure 6.2: The q - z trend determined using luminosity functions and survival analysis to account for non-detections in radio and infrared for different values of q_{min} (blue, orange and green lines). Colored intervals correspond to the 16th and 84th percentile of the q - z trend when derived from MCMC samples of parameters. The solid black line corresponds to the values without screening, while the dashed black line is the [Delhaize et al. \(2017\)](#) $q - z$ trend.

The luminosity functions span a range from minimal to maximal luminosity, but due to the fact that luminosity functions sharply fall for large luminosities, the higher luminosity limits need not be chosen carefully, due to smaller probabilities. We chose sufficiently high ends $R_M = 28$ and $I_M = 14$. However, at lower luminosity, the shapes of the luminosity functions do not fall sharply, but flatten out. Therefore, the choice of the lower luminosity limits impacts the luminosity function-derived probability distributions. To account for these effects, we employ the MCMC method to derive I_m , R_m and ρ for $z = 0$. We chose to emulate the q value corresponding to the local q value of [Yun et al. \(2001\)](#) and its dispersion. By the MCMC method, we have derived $I_m = 7.8 \pm 0.6$, $R_m = 18.9 \pm 0.4$ and $\rho = 0.91 \pm 0.06$, as shown in Fig. 6.3.

In Fig. 6.2 we show the $q - z$ trend determined with and without applying infrared an radio

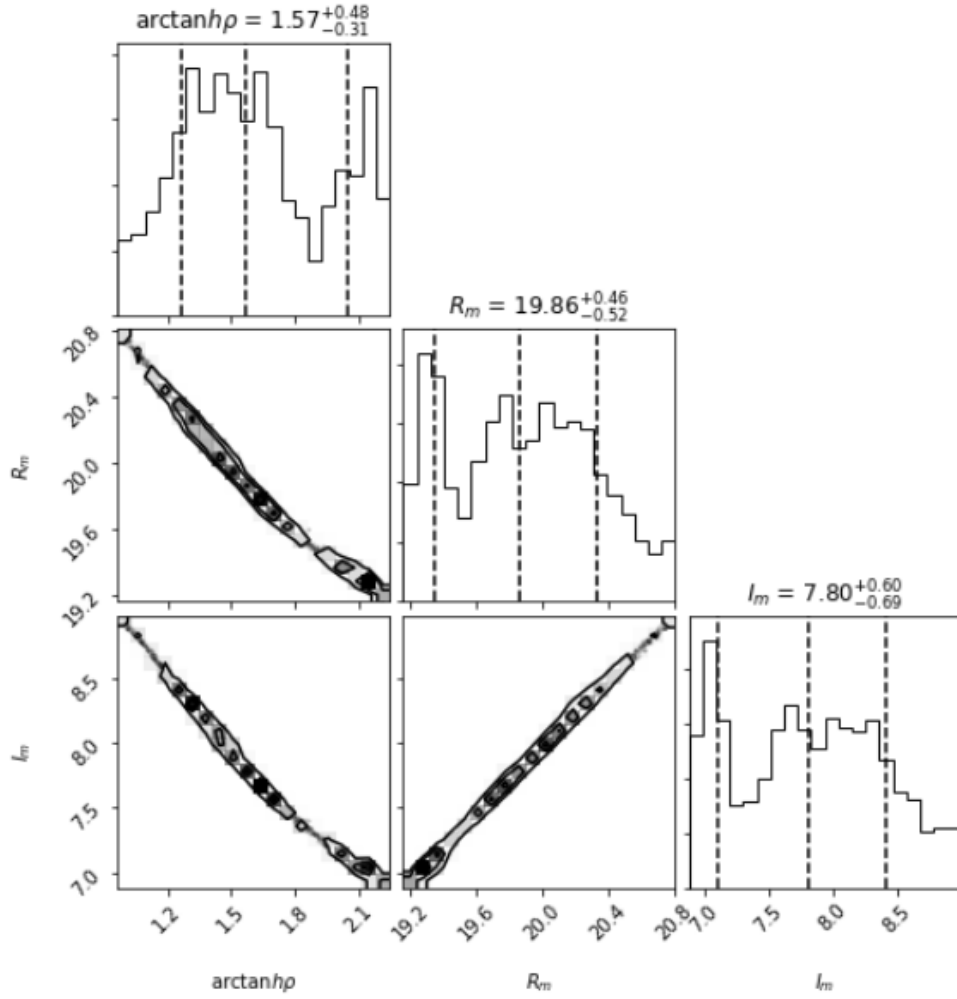


Figure 6.3: The limits of infrared (I_m) and radio (R_m) luminosity functions and the correlation coefficient, ρ , determined using MCMC.

limits. These limits effectively ‘screen’ a portion of the luminosity space and are therefore labeled by ‘screening’ in Fig 6.2. The screen was chosen to correspond to 5σ limits of Herschel for infrared luminosities and 3 GHz VLA-COSMOS limits of radio luminosities, to be as close as possible to [Delhaize et al. \(2017\)](#).

We see that without screening, we get an increase of q with z out to $z \sim 1$ beyond which q flattens with redshift, while survival analysis induces smaller q values at higher redshift. The full probability distribution results correspond to $q_{min} = 0$. Other values will be discussed in the next section.

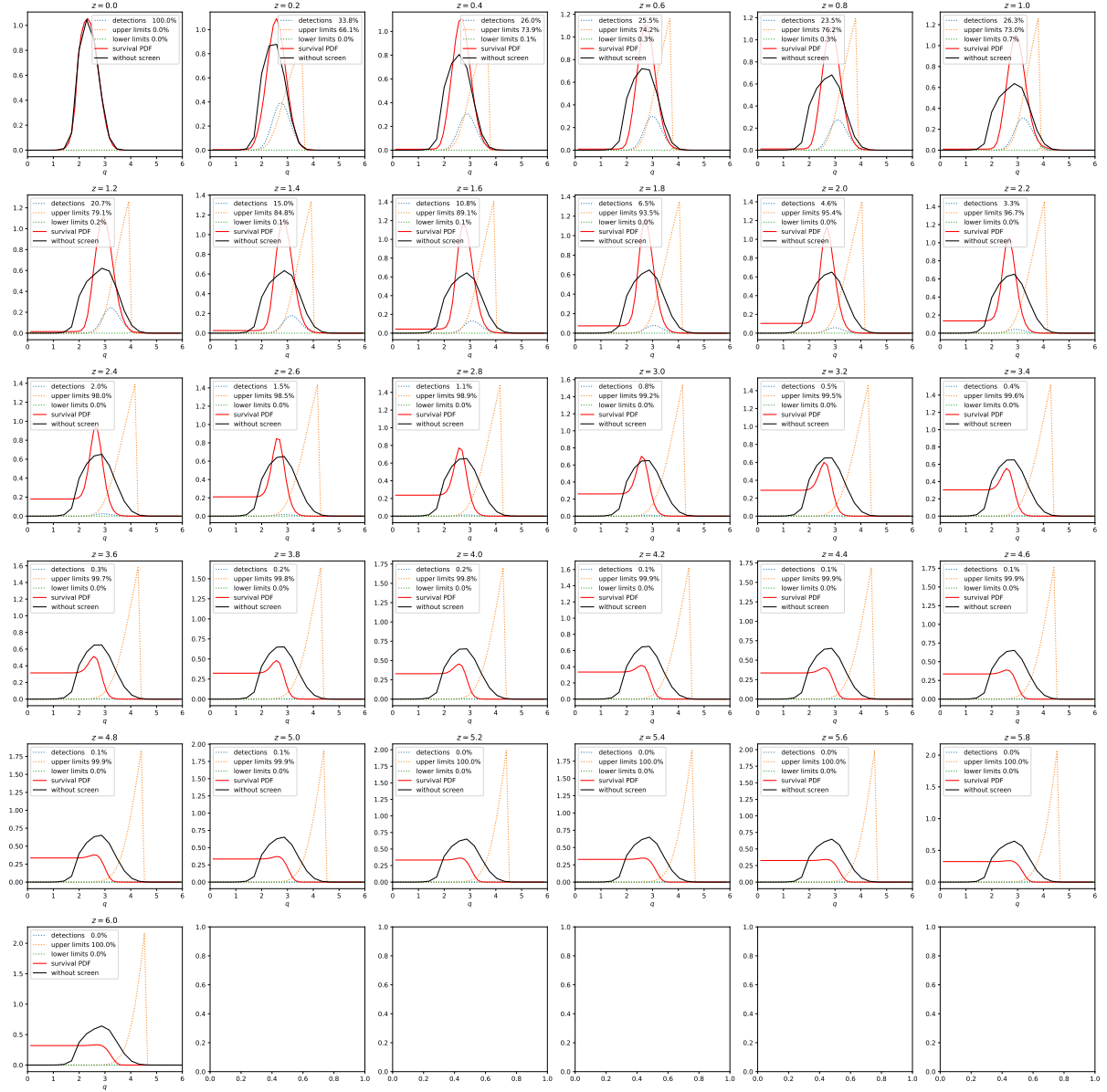


Figure 6.4: The q probability distribution computed with (red line) and without screening (solid black line). Blue and orange lines correspond to upper and lower limits, respectively.

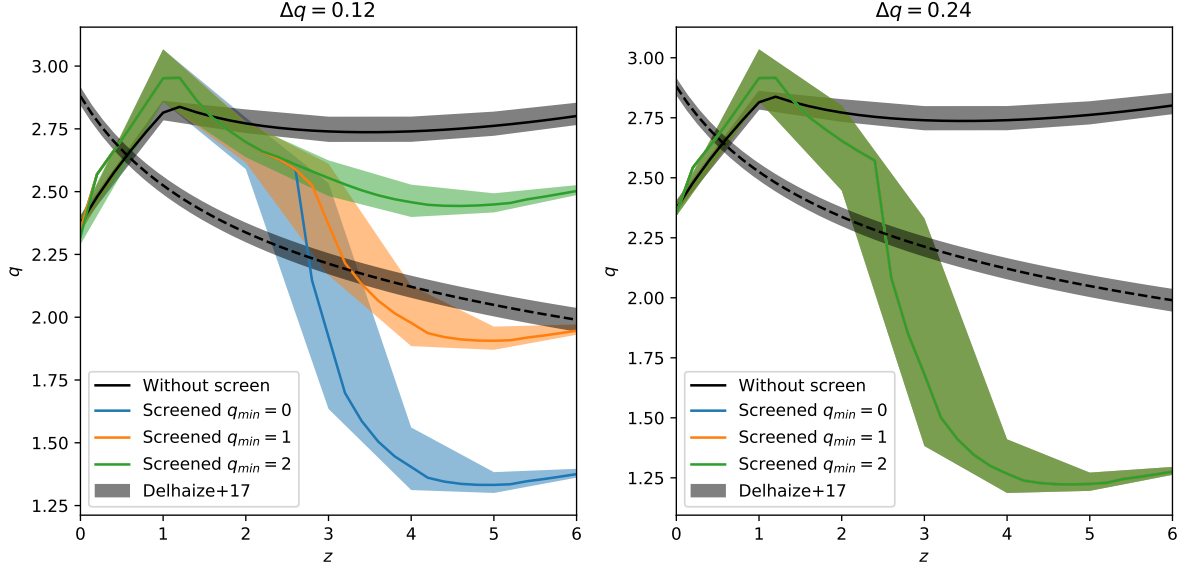


Figure 6.5: The q - z trend determined using luminosity functions and survival analysis, determined by fitting a Gaussian to the probability distribution, to account for non-detections in radio and infrared for different values of q_{min} (blue, orange and green lines). Colored intervals correspond to the 16th and 84th percentile of the q - z trend when derived from MCMC samples of parameters. The solid black line corresponds to the values without screening, while the dashed black line is the [Delhaize et al. \(2017\)](#) $q - z$ trend.

6.3 Discussion

The cause for the discrepancy in the redshift trend between the model computed using the full luminosity space (without screening) and that found by estimating q from survival analysis using luminosity limits (with screening) is due to flattening out of the survival distribution function below $q \sim 1 - 2$, as seen in the shapes of the distribution function for various redshifts in Fig. 6.4.

We have tested this property of the probability distribution by using two different q bin widths in Fig. 6.2 and found no significant difference between the two binning methods.

Furthermore, if we choose to limit ourselves to $q > q_{lim} \in \{1, 2\}$, we progressively diminish our $q - z$ trend, since the survival analysis-derived probability distribution is well constrained

above $q > 2$.

In Fig. 6.5, we have tried an alternative strategy by fitting a Gaussian to the probability distribution, and our findings remain the same.

6.4 Summary

We have devised a simple model for analytical estimation of the infrared-radio correlation using luminosity functions. We do this by combining the infrared luminosity function with the radio luminosity function for SFGs, combined using a Gaussian copula. The copula was chosen to reproduce the local q value of 2.34 and its dispersion (0.33). The resulting joint luminosity function is used to compute average q values at higher redshift values. By including redshift-dependent limits to infrared and radio luminosity, we find that the q values begin to decrease above $z \sim 1$, in contrast to a flat $q - z$ trend computed without accounting for limits above $z \sim 1$. In our model, this was due to the survival analysis not constraining well the q distribution below $q < 2$, which influenced the derived mean q values.

Further work needs to be done to test and verify the model using various data at low and high redshifts, and before these results can be compared to observations at high redshift, which also show a falling $q - z$ trend. For example, the computed joint luminosity function could be used to model observations using Monte Carlo simulations, which could then be used to compare the q values at different redshifts computed analytically to the survival analysis codes which have already been used in analyzing observations. Another complication to the basic model would be analyzing how our results change when modifying the low-luminosity ends of the luminosity functions by using different functional forms for the luminosity functions.

Chapter 7

Summary and outlook

In chapter 4 we have constructed the average radio spectral energy distribution for a 1.4 GHz-selected sample of highly star-forming galaxies with $\text{SFR} > 100 \text{ M}_\odot/\text{yr}$ in the COSMOS field. To achieve a broad rest-frame frequency range, we combined previously published VLA observations at 1.4 GHz and 3 GHz with unpublished GMRT observations at 325 MHz and 610 MHz by employing survival analysis to account for non-detections in the GMRT maps caused by their higher RMS values. By fitting a broken power-law to the SED, we find the spectral index to change from $\alpha_1 = 0.42 \pm 0.06$ below 4.3 GHz to $\alpha_2 = 0.94 \pm 0.06$ above 4.3 GHz. Our results are in line with previous low-redshift studies of star-forming galaxies with an $\text{SFR} > 10 \text{ M}_\odot/\text{yr}$ that show that their SED differs from the one found in normal star-forming galaxies by having a steeper spectral index around 10 GHz, which could imply a smaller thermal fraction than in normal star-forming galaxies. Furthermore, we have constructed the IR-radio correlation by using our broken power-law SED for galaxies with an $\text{SFR} > 10 \text{ M}_\odot/\text{yr}$ and an SED based on a steep nonthermal synchrotron spectral index ($\alpha = 0.97$) and a 10% thermal fraction at 1.4 GHz (Tabatabaei et al. 2017) for galaxies with $\text{SFR} < 10 \text{ M}_\odot/\text{yr}$. We find that the shape of the radio-SED is probably not the root cause of the redshift trend found by previous studies.

In chapter 5 we have constrained the radio SED for a sample of AGN in the COSMOS field. The radio-excess AGN (RxAGN) sample contained sources which exhibit a 3σ excess of 1.4 GHz radio luminosity, compared to that expected solely from star-forming processes occurring within

the AGN host galaxies. We found that if we fit the radio SED for this sample with a single power-law model, the resulting spectral index is 0.64 ± 0.07 . However, such a model does not capture all the features of the RxAGN radio SED which can be better described by a broken power-law with a spectral index of $\alpha_1 = 0.28 \pm 0.03$, below 4 GHz, and $\alpha_2 = 1.16 \pm 0.04$, above 4 GHz. The derived SED can be even better described by models involving both synchrotron self-absorption and synchrotron aging processes.

In short, we have established the different SED shapes for highly star-forming galaxies and RxAGN at radio frequencies around 1-10 GHz in the COSMOS field. Further work needs to be done to assess the possible differences in SEDs above 10 GHz, which would give better estimates of the free-free contribution in star-formation processes at high redshift. Furthermore, new observations below 1 GHz are needed to better constrain the SED shapes in this regime, and therefore to better understand radio K-corrections.

Motivated by our finding that the shape of the radio-SED is probably not the root cause of the redshift trend found by previous studies, in chapter 6, we have constructed a simple model for analytical estimation of the infrared-radio correlation using luminosity functions. We do this by combining the infrared luminosity function with the radio luminosity function for star-forming galaxies, combined using a Gaussian copula, chosen to reproduce the local q value and its dispersion. By modeling redshift-dependent limits to infrared and radio luminosity, we find that the q values in our model begin to decrease above $z \sim 1$, in contrast to a flat $q - z$ above $q \sim 1$ trend computed without accounting for limits. Further testing, such as applying Monte Carlo simulations and choosing different luminosity functions at low redshift, needs to be done before these results can be robustly compared to observations.

Bibliography

- Adams, W. S. 1941, The Astrophysical Journal, 93, 11
- Aghanim, N., Akrami, Y., Arroja, F., et al. 2019, Astronomy & Astrophysics
- Akiyama, K., Alberdi, A., Alef, W., et al. 2019, The Astrophysical Journal, 875, L1
- Alexander, D. M. & Hickox, R. C. 2012, New Astronomy Reviews, 56, 93
- Antonucci, R. 1993, Annual Review of Astronomy and Astrophysics, 31, 473
- Balbi, A., Ade, P., Bock, J., et al. 2000, \apjl, 545, L1
- Bardeen, J. M., Steinhardt, P. J., & Turner, M. S. 1983, Physical Review D, 28, 679
- Bennett, C. L. 1995, Nuclear Physics B - Proceedings Supplements, 38, 415
- Bennett, C. L., Halpern, M., Hinshaw, G., et al. 2003, The Astrophysical Journal Supplement Series, 148, 1
- Berta, S., Lutz, D., Santini, P., et al. 2013, Astronomy & Astrophysics, 551, A100
- Bertin, E. & Arnouts, S. 1996, Astronomy and Astrophysics Supplement Series, 117, 393
- Blundell, K. M., Rawlings, S., & Willott, C. J. 1999, The Astronomical Journal, 117, 677
- Bondi, M., Ciliegi, P., Zamorani, G., et al. 2003, Astronomy and Astrophysics, 403, 857
- Bondi, M., Zamorani, G., Ciliegi, P., et al. 2018, Astronomy & Astrophysics, 618, L8

- Boyle, B. J. & Terlevich, R. J. 1998, *Monthly Notices of the Royal Astronomical Society*, 293, L49
- Braun, R. 1996, in *The Westerbork Observatory, Continuing Adventure in Radio Astronomy* (Springer, Dordrecht), 167–183
- Bressan, A., Silva, L., & Granato, G. L. 2002, *Astronomy and Astrophysics*, 392, 377
- Bridle, A. H. & Schwab, F. R. 1999, in *Astronomical Society of the Pacific Conference Series*, Vol. 180, *Synthesis Imaging in Radio Astronomy II*, ed. G. B. Taylor, C. L. Carilli, & R. A. Perley, 371
- Bruzual, G. & Charlot, S. 2003, *Monthly Notices of the Royal Astronomical Society*, 344, 1000
- Buat, V. 1992, *Astronomy and Astrophysics -Berlin-*, 264, 444
- Buat, V., Deharveng, J., & Donas, J. 1989, *Astronomy and astrophysics* (Berlin. Print), 223, 42
- Burbidge, E. M., Burbidge, G. R., & Prendergast., K. H. 1959, *The Astrophysical Journal*, 130, 26
- Calistro Rivera, G., Williams, W. L., Hardcastle, M. J., et al. 2017, *Monthly Notices of the Royal Astronomical Society*, 469, 3468
- Calzetti, D., Kinney, A. L., & Storchi-Bergmann, T. 1994, *The Astrophysical Journal*, 429, 582
- Capak, P., Aussel, H., Ajiki, M., et al. 2007, *The Astrophysical Journal Supplement Series*, 172, 99
- Chabrier, G. 2003, *Publications of the Astronomical Society of the Pacific*, 115, 763
- Clemens, M. S., Alexander, P., & Green, D. A. 1999, *Monthly Notices of the Royal Astronomical Society*, 307, 481
- Clemens, M. S., Vega, O., Bressan, A., et al. 2008, *Astronomy & Astrophysics*, 477, 95

- Collier, J. D., Tingay, S. J., Callingham, J. R., et al. 2018, High-resolution Observations of Low-luminosity Gigahertz-Peaked Spectrum and Compact Steep Spectrum Sources, Tech. rep.
- Condon, J. J. 1992, *Annual Review of Astronomy and Astrophysics*, 30, 575
- Condon, J. J., Huang, Z.-P., Yin, Q. F., & Thuan, T. X. 1991, *The Astrophysical Journal*, 378, 65
- Condon, J. J. & Ransom, S. M. 2016, *Essential Radio Astronomy*, 1–22
- Condon, J. J. & Yin, Q. F. 1990, *The Astrophysical Journal*, 357, 97
- Cotton, W. D., Wittels, J. J., Shapiro, I. I., et al. 1980, *The Astrophysical Journal*, 238, L123
- Croton, D. J., Springel, V., White, S. D., et al. 2006, *Monthly Notices of the Royal Astronomical Society*, 365, 11
- Croton, D. J., Stevens, A. R. H., Tonini, C., et al. 2016, *The Astrophysical Journal Supplement Series*, 222, 22
- Da Cunha, E., Charlot, S., & Elbaz, D. 2008, *Monthly Notices of the Royal Astronomical Society*, 388, 1595
- de Bernardis, P., Ade, P. A. R., Bock, J. J., et al. 2000, *\nat*, 404, 955
- de Jong, T., Klein, U., Wielebinski, R., et al. 1985, *Astronomy and Astrophysics*, 147, L6
- de Sitter, W. 1916, *Monthly Notices of the Royal Astronomical Society*, 76, 699
- de Vaucouleurs, G. 1959, *Handbuch der Physik*, 53, 275
- De Zotti, G., Massardi, M., Negrello, M., & Wall, J. 2010, *Astronomy and Astrophysics Review*, 18, 1
- Deeg, H.-J., Brinks, E., Duric, N., Klein, U., & Skillman, E. 1993, *The Astrophysical Journal*, 410, 626

- Delhaize, J., Smolčić, V., Delvecchio, I., et al. 2017, *Astronomy & Astrophysics*, 602, A4
- Delvecchio, I., Smolčić, V., Zamorani, G., et al. 2017, *Astronomy & Astrophysics*, 602, A3
- Dewdney, P. E., Hall, P. J., Schilizzi, R. T., & Lazio, T. J. L. W. 2009, *IEEE Proceedings*, 97, 1482
- Di Matteo, T., Springel, V., & Ilernquist, L. 2005, *Nature*, 433, 604
- Dicke, R. H., Peebles, P. J. E., Roll, P. G., & Wilkinson, D. T. 1965, *\apj*, 142, 414
- Dickey, J. M. & Salpeter, E. E. 1984, *\apj*, 284, 461
- Donley, J. L., Koekemoer, A. M., Brusa, M., et al. 2012, *Astrophysical Journal*, 748
- Dreyer, J. L. E. 1888, *MmRAS*, 49, 1
- Dunlop, J. S. & Peacock, J. A. 1990, *Monthly Notices of the Royal Astronomical Society*, 247, 19
- Edge, A. C., Pooley, G., Jones, M., Grainge, K., & Saunders, R. 1998, *IAU Colloq. 164: Radio Emission from Galactic and Extragalactic Compact Sources*, 144, 187
- Efstathiou, G., Bond, J. R., & White, S. D. M. 1992, *\mnras*, 258, 1P
- Eggen, O. J., Lynden-Bell, D., & Sandage, A. R. 1962, *The Astrophysical Journal*, 136, 748
- Einstein, V. A. 1919, *Die Naturwissenschaften*, 7, 232
- Elbaz, D., Daddi, E., Le Borgne, D., et al. 2007, *Astronomy and Astrophysics*, 468, 33
- Elbaz, D., Dickinson, M., Hwang, H. S., et al. 2011, *Astronomy & Astrophysics*, 533, A119
- Fabbiano, G., Gioia, I. M., & Trinchieri, G. 1988, *The Astrophysical Journal*, 324, 749
- Fall, S. M. & Efstathiou, G. 1980, *Monthly Notices of the Royal Astronomical Society*, 193, 189
- Fanaroff, B. L.; Riley, J. M. 1974, *Monthly Notices of the Royal Astronomical Society*, 167, 31

- Fanti, R., Fanti, C., Schilizzi, R. T., et al. 1990, *Astronomy and Astrophysics* (ISSN 0004-6361), 231, 333
- Farouki, R. T. & Shapiro, S. L. 1982, *The Astrophysical Journal*, 259, 103
- Feigelson, E. D. & Nelson, P. I. 1985, *The Astrophysical Journal*, 293, 192
- Ferrarese, L. & Merritt, D. 2000, *The Astrophysical Journal*, 539, L9
- Fixsen, D. J. 2009, *\apj*, 707, 916
- Fixsen, D. J., Cheng, E. S., Gales, J. M., et al. 1996, *\apj*, 473, 576
- Forbes, D. A. & Kroupa, P. 2011, *Publications of the Astronomical Society of Australia*, 28, 77
- Foreman-Mackey, D., Hogg, D. W., Lang, D., & Goodman, J. 2013, *Publications of the Astronomical Society of the Pacific*, 125, 306
- Friedman, A. 1922, *Zeitschrift für Physik*, 10, 377
- Gallagher, John S., I. 1972, *The Astronomical Journal*, 77, 568
- Galvin, T. J., Seymour, N., Marvil, J., et al. 2018, *Monthly Notices of the Royal Astronomical Society*, 474, 779
- Garn, T., Green, D. A., Riley, J. M., & Alexander, P. 2008, *Monthly Notices of the Royal Astronomical Society*, 387, 1037
- Gerhard, O. E. 1981, *Monthly Notices of the Royal Astronomical Society*, 197, 179
- Green, D. A. 2014, *Bulletin of the Astronomical Society of India*, 42, 47
- Gruppioni, C., Pozzi, F., Rodighiero, G., et al. 2013, *Monthly Notices of the Royal Astronomical Society*, 432, 23
- Hales, C. A., Murphy, T., Curran, J. R., et al. 2012, *Monthly Notices of the Royal Astronomical Society*, 425, 979

- Hao, C. N., Kennicutt, R. C., Johnson, B. D., et al. 2011, *Astrophysical Journal*, 741
- Heckman, T. M. & Best, P. N. 2014, *Annual Review of Astronomy and Astrophysics*, 52, 589
- Helou, G., Soifer, B. T., & Rowan-Robinson, M. 1985, *The Astrophysical Journal*, 298, L7
- Heywood, I., Jarvis, M. J., & Condon, J. J. 2013, *Monthly Notices of the Royal Astronomical Society*, 432, 2625
- Hubble, E. 1929, *Proceedings of the National Academy of Sciences*, 15, 168
- Hubble, E. P. 1925, *The Astrophysical Journal*, 62, 409
- Hubble, E. P. 1926, *The Astrophysical Journal*, 64, 321
- Hummel, E. 1986, *\aap*, 160, L4
- Hurley-Walker, N., Morgan, J., Wayth, R. B., et al. 2014, *Publications of the Astronomical Society of Australia*, 31, e045
- Ibar, E., Cirasuolo, M., Ivison, R., et al. 2008, *Mon. Not. R. Astron. Soc*, 386, 953
- Intema, H. T., Jagannathan, P., Mooley, K. P., & Frail, D. A. 2017, *Astronomy & Astrophysics*, 598, A78
- Ivison, R. J., Alexander, D. M., Biggs, A. D., et al. 2010, *Monthly Notices of the Royal Astronomical Society*, 402, 245
- Jaffe, Walter; Ford, H. C. T. Z. F. L. D. L. 1999, *ASP Conference Series*, 182
- Jaffe, W. J. J. & Perola, G. C. C. 1973, *a&a*, 26, 423
- Jarvis, M. J. & Rawlings, S. 2002, *Monthly Notices of the Royal Astronomical Society*, 319, 121
- Kameno, S., Inoue, M., Wajima, K., Shen, Z. Q., & Sawada-Satoh, S. 2005, in *Astronomical Society of the Pacific Conference Series*, Vol. 340, *Future Directions in High Resolution Astronomy*, ed. J. Romney & M. Reid, 145

- Kapahi, V. K. 1981, *Astronomy and Astrophysics Supplement Series*, 43, 381
- Kaplan, E. L. & Meier, P. 1958, *Journal of the American Statistical Association*, 53, 457
- Kardashev, N. S.; Kuz'min, A. D. S. S. I. 1962a, *Soviet Astronomy*, 6, 167
- Kardashev, N. S. 1962b, *Soviet Astronomy*, 5, 317
- Katz, N. 1992, *The Astrophysical Journal*, 391, 502
- Katz, N. & Gunn, J. E. 1991, *The Astrophysical Journal*, 377, 365
- Kauffmann, G. & Haehnelt, M. 2000, *Monthly Notices of the Royal Astronomical Society*, 311, 576
- Kellermann, K. I. & Pauliny-Toth, I. I. K. 1969, *The Astrophysical Journal*, 155, L71
- Kennicutt, R. C., J. 1983, *The Astrophysical Journal*, 272, 54
- Kennicutt, R. C., J. & Kent, S. M. 1983, *The Astronomical Journal*, 88, 1094
- Kennicutt, R. C. 1997, *The Astrophysical Journal*
- Kennicutt, R. C. 1998a, *Annual Review of Astronomy and Astrophysics*, 36, 189
- Kennicutt, Jr., R. C. 1998b, *The Astrophysical Journal*, 498, 541
- Ker, L. M., Best, P. N., Rigby, E. E., Röttgering, H. J., & Gendre, M. A. 2012, *Monthly Notices of the Royal Astronomical Society*, 420, 2644
- Kimball, A. E. & Ivezić, v. 2008, *Astronomical Journal*
- Klein, U., Lisenfeld, U., & Verley, S. 2018, *Astronomy & Astrophysics*, 611, A55
- Klein, U., Wielebinski, R., & Morsi, H. W. 1988, *Astronomy and Astrophysics* (ISSN 0004-6361), 190, 41
- Kogut, A., Spergel, D. N., Barnes, C., et al. 2003, *ApJS*, 148, 161

- Kolokythas, K., O’Sullivan, E., Giacintucci, S., et al. 2015, *Monthly Notices of the Royal Astronomical Society*, 450, 1732
- Kormendy, J. & Richstone, D. 1995, *Annual Review of Astronomy and Astrophysics*, 33, 581
- Kroupa, P. & Pavel. 2001, *MNRAS*, 322, 231
- Kukula, M. J., Dunlop, J. S., Hughes, D. H., & Rawlings, S. 1998, *Monthly Notices of the Royal Astronomical Society*, 297, 366
- Lai, C.-D., Murthy, D., & Xie, M. 2006, in *Springer Handbook of Engineering Statistics*, ed. H. Pham (London: Springer London), 63–78
- Laigle, C., McCracken, H. J., Ilbert, O., et al. 2016, *The Astrophysical Journal Supplement Series*, 224, 24
- Larson, R. B. 1969, *Monthly Notices of the Royal Astronomical Society*, 145, 405
- Larson, R. B. 1974a, *Monthly Notices of the Royal Astronomical Society*, 166, 585
- Larson, R. B. 1974b, *Monthly Notices of the Royal Astronomical Society*, 169, 229
- Larson, R. B. 1975, *Monthly Notices of the Royal Astronomical Society*, 173, 671
- Larson, R. B. 1976, *Monthly Notices of the Royal Astronomical Society*, 176, 31
- Lemaitre, A. G. 1931, *Monthly Notices of the Royal Astronomical Society*, 91, 483
- Leroy, A. K., Evans, A. S., Momjian, E., et al. 2011, *Astrophysical Journal Letters*, 739, L25
- Lilly, S. J., Carollo, C. M., Pipino, A., Renzini, A., & Peng, Y. 2013, *Astrophysical Journal*, 772, 119
- Lin, C. C. & Shu, F. H. 1964, *The Astrophysical Journal*, 140, 646
- Lisenfeld, U., Wilding, T. W., Pooley, G. G., & Alexander, P. 2004, *Monthly Notices of the Royal Astronomical Society*, 349, 1335

- Lonsdale, C. J., Diamond, P. J., Thrall, H., Smith, H. E., & Lonsdale, C. J. 2006, *The Astrophysical Journal*, 647, 185
- Macias-Pérez, J. F., Lagache, G., Maffei, B., et al. 2007, *\aap*, 467, 1313
- Madau, P. & Dickinson, M. 2014, *Annual Review of Astronomy and Astrophysics*, 52, 415
- Madau, P., Ferguson, H. C., Dickinson, M. E., et al. 1996, *Monthly Notices of the Royal Astronomical Society*, 283, 1388
- Madau, P., Pozzetti, L., & Dickinson, M. 1998, *The Astrophysical Journal*, 498, 106
- Magnelli, B., Ivison, R. J., Lutz, D., et al. 2015, *Astronomy & Astrophysics*, 573, A45
- Magorrian, J., Tremaine, S., Richstone, D., et al. 1998, *The Astronomical Journal*, 115, 2285
- Mahajan, S., Ashby, M. L., Willner, S. P., et al. 2019, *Monthly Notices of the Royal Astronomical Society*, 482, 560
- Mathews, W. G. & Baker, J. C. 1971, *The Astrophysical Journal*, 170, 241
- McKellar, A. 1941, *Publications of the Dominion Astrophysical Observatory*, 7, 251
- Menon, T. K. 1983, *The Astronomical Journal*, 88, 598
- Messier, C. 1781, *Connaissance des Temps ou des Mouvements Célestes*, 227
- Mhaskey, M., Gopal-Krishna, Dabhade, P., et al. 2019, *Monthly Notices of the Royal Astronomical Society*
- Mihos, J. C. & Hernquist, L. 1996, *The Astrophysical Journal*, 464, 641
- Miller, A., Beach, J., Bradley, S., et al. 2002, *\apjs*, 140, 115
- Mo, H., van den Bosch, F. C., & White, S. 2010, *gfe*
- Molnár, D. C., Sargent, M. T., Delhaize, J., et al. 2018, *Monthly Notices of the Royal Astronomical Society*, 475, 827

- Murphy, E. J. 2009, *Astrophysical Journal*, 706, 482
- Narayan, R. & Yi, I. 1994, *The Astrophysical Journal*, 428, L13
- Navarro, J. F. & Benz, W. 1991, *The Astrophysical Journal*, 380, 320
- Navarro, J. F. & White, S. D. 1994, *Monthly Notices of the Royal Astronomical Society*, 267, 401
- Netzer, H. 2015, *Annual Review of Astronomy and Astrophysics*, 53, 365
- Niklas, S. 1997, *Astronomy and Astrophysics*, 322, 29
- Noeske, K. G., Weiner, B. J., Faber, S. M., et al. 2007, *The Astrophysical Journal*, 660, L43
- Norris, R. P., Afonso, J., Bacon, D., et al. 2013, *Publications of the Astronomical Society of Australia*, 30, e020
- Novak, M., Smolčić, V., Civano, F., et al. 2015, *Monthly Notices of the Royal Astronomical Society*, 447, 1282
- Novak, M., Smolčić, V., Schinnerer, E., et al. 2018, *Astronomy and Astrophysics*, 614, 1
- O'Dea, C. P. 1998, *Publications of the Astronomical Society of the Pacific*, 110, 493
- O'Dea, C. P. & Baum, S. A. 1997, *The Astronomical Journal*, 113, 148
- O'Dea, C. P., Baum, S. A., & Stanghellini, C. 1991, *The Astrophysical Journal*, 380, 66
- Orienti, M. & Dallacasa, D. 2014, *Monthly Notices of the Royal Astronomical Society*, 438, 463
- Ostriker, J. P. 1980, *Comments on As*, 8, 177
- Ostriker, J. P. & Peebles, P. J. E. 1973, *The Astrophysical Journal*, 186, 467
- Pacholczyk, A. G. 1977, *Radio galaxies: Radiation transfer, dynamics, stability and evolution of a synchrotron plasmon*, Vol. 89

- Padovani, P. 2016, *The Astronomy and Astrophysics Review*, 24, 13
- Peacock, J. A. & Wall, J. V. 1982, *Monthly Notices of the Royal Astronomical Society*, 198, 843
- Penzias, A. A. & Wilson, R. W. 1965, *\apj*, 142, 419
- Perlmutter, S., Aldering, G., Goldhaber, G., et al. 1999, *The Astrophysical Journal*, 517, 565
- Pohl, M.; Schlickeiser, R. H. E. 1991, *Astronomy and astrophysics* (Berlin. Print), 250, 302
- Prandoni, I. & Seymour, N. 2015, *Advancing Astrophysics with the Square Kilometre Array (AASKA14)*, 67
- Prouton, O. R., Bressan, A., Clemens, M., et al. 2004, *Astronomy and Astrophysics*, 421, 115
- Rau, U. & Cornwell, T. J. 2011, *Astronomy & Astrophysics*, 532, A71
- Razin, V. A. 1960, *Iz. VUZ*, 3, 584
- Razin, V. N. 1951, *Vestn. Mosk. Univ.*, 11, 27
- Roberts, M. S. 1963, *Annual Review of Astronomy and Astrophysics*, 1, 149
- Robertson, H. P. 1935, *The Astrophysical Journal*, 82, 284
- Rubin, V. C. & Ford, W. Kent, J. 1970, *The Astrophysical Journal*, 159, 379
- Rubin, V. C., Thonnard, N., & Ford, W. K., J. 1978, *The Astrophysical Journal*, 225, L107
- Salpeter, E. E. 1955, *The Astrophysical Journal*, 121, 161
- Sancisi, R.; van Albada, T. S. 1987, *Dark Matter in the Universe. Proceedings of the 117th. Symposium of the International Astronomical Union*, 117, 67
- Sanders, D. B. & Mirabel, I. F. 1985, *\apjl*, 298, L31
- Sanders, D. B. & Mirabel, I. F. 1996, *\araa*, 34, 749
- Sanders, D. B., Salvato, M., Aussel, H., et al. 2007, *The Astrophysical Journal Supplement Series*, 172, 86

- Schinnerer, E., Sargent, M. T., Bondi, M., et al. 2010, *Astrophysical Journal, Supplement Series*, 188, 384
- Schinnerer, E., Smolčić, V., Carilli, C. L., et al. 2007, *The Astrophysical Journal Supplement Series*, 172, 46
- Schmidt, M. 1959, *The Astrophysical Journal*, 129, 243
- Schmidt, M. 1963, *Nature*, 197, 1040
- Schmitt, J. H. M. M. 1985, *The Astrophysical Journal*, 293, 178
- Scoville, N., Aussel, H., Brusa, M., et al. 2007, *The Astrophysical Journal Supplement Series*, 172, 1
- Seabold, S. & Perktold, J. 2010, in *Proceedings of the 9th Python in Science Conference*, ed. S. van der Walt & J. Millman No. *Scipy*, 57–61
- Seyfert, C. K. 1943, *The Astrophysical Journal*, 97, 28
- Shakura, N. I. & Sunyaev, R. A. 1973, *Symposium - International Astronomical Union*, 55, 155
- Shankar, F., Weinberg, D. H., & Miralda-Escudé, J. 2009, *Astrophysical Journal*, 690, 20
- Silverman, J. D., Green, P. J., Barkhouse, W. A., et al. 2008, *The Astrophysical Journal*, 679, 118
- Smolčić, V., Ciliegi, P., Jelić, V., et al. 2014, *Monthly Notices of the Royal Astronomical Society*, 443, 2590
- Smolčić, V., Delvecchio, I., Zamorani, G., et al. 2017a, *Astronomy & Astrophysics*, 602, A2
- Smolčić, V., Intema, H., Šlaus, B., et al. 2018, *Astronomy & Astrophysics*, 620, A14
- Smolčić, V., Novak, M., Bondi, M., et al. 2017b, *Astronomy & Astrophysics*, 602, A1
- Smoot, G. F., Bennett, C. L., Kogut, A., et al. 1992, *apjl*, 396, L1

- Sotan, A. 1982, *Monthly Notices of the Royal Astronomical Society*, 200, 115
- Sparke, L. S. & Gallagher, J. S. I. 2007, *Galaxies in the Universe: An Introduction* (Cambridge: Cambridge University Press)
- Szokoly, G. P., Bergeron, J., Hasinger, G., et al. 2004, *The Astrophysical Journal Supplement Series*, 155, 271
- Tabatabaei, F. S., Schinnerer, E., Krause, M., et al. 2017, *The Astrophysical Journal*, 836, 185
- Tingay, S. J. & de Kool, M. 2003, *\aj*, 126, 723
- Tisanić, K., Smolčić, V., Delhaize, J., et al. 2019, *Astronomy & Astrophysics*, 621, A139
- Toba, Y., Yamashita, T., Nagao, T., et al. 2019, *\apjs*, 243, 15
- Toomre, A. & Toomre, J. 1972, *The Astrophysical Journal*, 178, 623
- Transtrum, M. K., MacHta, B. B., & Sethna, J. P. 2010, *Physical Review Letters*, 104
- Transtrum, M. K. & Qiu, P. 2014, *Physical Review Letters*, 113, 098701
- Tribble, P. C. 2014, *Monthly Notices of the Royal Astronomical Society*, 261, 57
- van den Bergh, S. 1957, *The Astrophysical Journal*, 125, 445
- van der Kruit, P. C. 1971, *Astronomy and Astrophysics*, 15, 110
- van Haarlem, M. P., Wise, M. W., Gunst, A. W., et al. 2013, *Astronomy & Astrophysics*, 556, A2
- Vardoulaki, E., Jiménez Andrade, E. F., Karim, A., et al. 2019, *Astronomy and Astrophysics*, 627, 1
- Voelk, H. J. 1989, *Astronomy and Astrophysics* (ISSN 0004-6361), 218, 67
- Walker, A. G. 1937, *Proceedings of the London Mathematical Society*, s2-42, 90
- White, S. D. M. 1978, *Monthly Notices of the Royal Astronomical Society*, 184, 185

- White, S. D. M. & Frenk, C. S. 1991, *The Astrophysical Journal*, 379, 52
- White, S. D. M. & Rees, M. J. 1978, *Monthly Notices of the Royal Astronomical Society*, 183, 341
- Whittam, I. H., Green, D. A., Jarvis, M. J., & Riley, J. M. 2017, *Monthly Notices of the Royal Astronomical Society*, 464, 3357
- Wilman, R. J., Miller, L., Jarvis, M. J., et al. 2008a, *Monthly Notices of the Royal Astronomical Society*, 388, 1335
- Wilman, R. J., Miller, L., Jarvis, M. J., et al. 2008b, *Monthly Notices of the Royal Astronomical Society*, 388, 1335
- Wunderlich, E., Wielebinski, R., & Klein, U. 1987, *Astronomy and Astrophysics Supplement Series* (ISSN 0365-0138), 69, 487
- Yun, M. S., Reddy, N. A., & Condon, J. J. 2001, *The Astrophysical Journal*, 554, 803

Curriculum vitae

Krešimir Tisanić was born in 1992 in Zagreb (Croatia). He obtained his master's degree in Physics at the Department of Physics, Faculty of Science at the University of Zagreb in 2016, with the thesis titled 'Comparison of hot cores using millimetre spectroscopy', under supervision of prof. dr. sc. Vernesa Smolčić and dr. sc. Oskari Miettinen. In July 2016, he started working in the group led by prof. dr. sc. Vernesa Smolčić, under the ERC project 337595: 'Constraining Stellar Mass and Supermassive Black Hole Growth through Cosmic Times: Paving the way for the next generation sky surveys'. He has presented his work at 5 international and 3 domestic conferences, and took part in one workshop.

Submitted publications

- **Tisanić, K.**, Smolčić, V., Imbrišak, M., Bondi, M., Zamorani, G., Ceraj, L., et al., submitted to A&A, The VLA-COSMOS 3 GHz Large Project: Average radio spectral energy distribution of active galactic nuclei
- Šlaus, B., Smolčić, V., Novak, M., Fotopoulou, S., Ciliegi, P., Jurlin, N., Ceraj, L., **Tisanić, K.**, Birkinshaw, M., Bremer, M., Chiappetti, L., Horellou, C., Huynh, M., Intema, H., Kolokythas, K., Pierre, M., Raychaudhury, S., Rottgering, H., submitted to A&A, The XXL Survey. XLI. Radio AGN luminosity functions based on the GMRT 610 MHz continuum observations
- Molnar, D. Cs., Sargent, M. T., Leslie, S., Magnelli, B., Schinnerer, E., Zamorani, G., Delhaize, J., Smolčić, V., **Tisanić, K.**, Vardoulaki, E., submitted to MNRAS, The non-linear infrared-radio correlation of low-z galaxies: implications for redshift evolution, a new radio SFR recipe, and how to minimize selection bias

Refereed publications

- Gómez-Guijarro, C., Magdis, G. E., Valentino, F., Toft, S., Man, A. W. S., Ivison, R. J., **Tisanić, K.**, van der Vlugt, D., Stockmann, M., Martin-Alvarez, S., Brammer, G. (2019),

ApJ, 886, Compact Star-forming Galaxies as Old Starbursts Becoming Quiescent,88.

- Vardoulaki, E., Jiménez Andrade, E. F., Karim, A., Novak, M., Leslie, S. K., **Tisanić, K.**, Smolčić, V., Schinnerer, E., Sargent, M. T., Bondi, M., Zamorani, G., Magnelli, B., Bertoldi, F., Herrera Ruiz, N., Mooley, K. P., Delhaize, J., Myers, S. T., Marchesi, S., Koekemoer, A. M., Gozaliasl, G., Finoguenov, A., Middleberg, E., Ciliegi, P. (2019), A&A, 627, A closer look at the deep radio sky: Multi-component radio sources at 3 GHz VLA-COSMOS,A142.
- **Tisanić, K.**, Smolčić, V., Delhaize, J., Novak, M., Intema, H., Delvecchio, I., Schinnerer, E., Zamorani, G., Bondi, M., Vardoulaki, E. (2019), A&A, 621, The VLA-COSMOS 3 GHz Large Project: Average radio spectral energy distribution of highly star-forming galaxies,A139.

Non-refereed publications

- **Tisanić, K.**, Smolčić, V., Delhaize, J., Novak, M., Intema, H., Delvecchio, I., Schinnerer, E., Zamorani, G. (2018), Peering towards Cosmic Dawn, 333, Average radio spectral energy distribution of highly star-forming galaxies,191.